Unit cell thick ferrimagnetic Heusler domain wall motion using Chemical Templating Layers

Dissertation

zur Erlangung des Doktorgrades der Naturwissenschaften (Dr. rer. nat.)

der

Naturwissenschaftlichen Fakultät II
Chemie, Physik und Mathematik

der Martin-Luther-Universität Halle-Wittenberg

vorgelegt von

Herrn **Panagiotis Charilaos Filippou**
geb. am 25.02.1986 in Amarousio, Griechenland

Gutachter: Prof. Dr. Stuart S. P. Parkin
Prof. Dr. Jamal Berakdar
Prof. Dr. Wolfgang Kuch

Tag der öffentlichen Verteidigung: 20.03.2019

Contents

List of Figures vi

List of Tables viii

Abbreviations ix

Abstract 1

Introduction 2

1. Deposition Growth and Measurement Setup 5

1.1. Material growth techniques 5

1.1.1. Magnetron Sputtering 6

1.1.2. Ion Beam Deposition 9

1.2. Characterizing Techniques 10

1.2.1. Profilometer and Resistivity measurements 10

1.2.2. RBS-PIXE 10

1.2.3. Magneto-optic Kerr effect for P-MOKE and Kerr microscopy 12

1.2.4. Atomic Force Microscopy 13

1.2.5. X-ray Diffraction 15

1.3. Domain Wall Motion Measurement Setup 17

1.3.1. Kerr Microscopy 17

1.3.2. Pulse Generator and Circuitry 19

1.4. Fabrication and patterning 20

2. Magnetization Dynamics for the Heusler DW motion 23

2.1. Landau-Lifshitz-Gilbert equation 25

2.2. Volume Spin Transfer Torque 26

2.3. Spin Hall Effect 27

2.4. Dzyaloshinskii Moriya Interaction 28

3. Underlayer Chemical Templating Technique to promote the Heusler Growth.... 29
3.1. Properties.... 29
3.2. CoAl – CoGa – CoGe – CoSn.... 34
3.3. CTL Results – X-ray diffraction 35
3.4. CTL Results – AFM and surface roughness with T_{AN} 39
3.5. Transmission Electron Microscopy.... 40
3.6. Results – P-MOKE of Heuslers grown on CTL and ordering with T_{AN} 43
3.6.1. Ambient Temperature and Room Temperature growth.... 45
3.7. CTL – Heusler growth on Silicon substrate and P-MOKE, S-VSM.... 47
3.8. Conclusions 48
4. Ultrathin Heusler DW motion under Kerr microscopy 49
4.1. Main results and Mn_3Z DW motion.... 49
4.1.1. Single DW creation to allow for DW motion experiments.... 50
4.1.2. Mn_3Z DW velocity dependence on the applied current density 52
4.2. DW motion for CoSn, CoAl, CoGa CTL layers in Mn_xSb (x=2.0, 2.7, 3.1) 55
4.3. DW motion dependence on nanowire width.... 56
4.4. Current pulse length dependence for different Heusler film thicknesses.... 57
4.5. Under external Fields – unraveling the mechanism of DW motion.... 59
4.5.1. Illustration of the DW within a nanowire 63
4.6. Bulk DMI and Spin-orbit Torques 65
4.7. Conclusions 67
5. Tailoring the SOTs and Bulk DMI field.... 69
5.1. Tuning the spin-orbit torques by atomically engineering the overlayers.... 69
5.2. Tailoring the bulk DMI field with composition of Mn_xSb 72
5.3. Conclusions 74
6. Mn_3Ge ex-situ annealing temperature dependence 76

6.1. P-MOKE dependence on ex-situ annealing temperature 76
6.2. Domain Wall velocity dependence on ex-situ annealing temperature 77
6.3. Conclusions 79
7. 1-D analytical model for the ultrathin Heusler DW motion 80
7.1. 1-D analytical model for the DW motion in Heusler films 80
7.2. 1-D model simulated curves for H_x, H_y DW velocity dependence 82
8. Conclusions 86
A.1 P-MOKE for Mn_2CoSn on CoGa CTL 88
A.2 DW velocity vs H_x and H_y for CoSn and CoAl CTLs 89
B.1 1-D analytical model for Heusler films 90
B.2 1-D model estimated parameter values 98
Bibliography 101
Publications 113
Acknowledgments 114
Curriculum Vitae 116
Eidesstattliche Erklärung 118

List of Figures

Figure 1.1 Illustration of the Magneto optic Kerr Effect 13
Figure 1.2 Illustration of an atomic force microscope. 14
Figure 1.3 Illustration of a Bragg-Brentano geometry XRD setup. 16
Figure 1.4 Kerr images in differential mode 18
Figure 1.5 Differential mode Kerr microscopy 19
Figure 1.6 Fabrication process. 22
Figure 3.1 CoGa unit cell for CsCl type structure 30
Figure 3.2 Schematic illustration of the Chemical Templating concept 31
Figure 3.3 $D0_{22}$ tetragonal unit cell of Mn_3Z 32
Figure 3.4 XRD diffractogram vs T_{AN} for CoAl CTL 36
Figure 3.5 XRD diffractogram vs T_{AN} for CoGa CTL 37
Figure 3.6 XRD diffractogram vs T_{AN} for CoGe CTL 38
Figure 3.7 XRD diffractogram vs T_{AN} for CoSn CTL 39
Figure 3.8 Film roughness dependence 40
Figure 3.9 Cross sectional scanning TEM images 42
Figure 3.10 Heusler P-MOKE hysteresis loops for different CTLs 44
Figure 3.11 P-MOKE loops for CTL, Cr and CTL with Sb insertion layer. 45
Figure 3.12 P-MOKE of 20 Å Mn_3Ge grown at 100 °C and at 30 °C. 46
Figure 3.13 P-MOKE and S-VSM for 20 Å Mn_3Sb 47
Figure 4.1 Mn_3Ge DW velocity versus current density J. 53
Figure 4.2 Mn_3Sn DW velocity versus current density J 53
Figure 4.3 Mn_3Sb DW velocity versus current density J 54
Figure 4.4 Mn_xSb DW velocity versus current density J 55
Figure 4.5 DW velocity for different wire widths 57
Figure 4.6 Pulse length dependence of the DW velocity 58
Figure 4.7 Image of the nanowire 59
Figure 4.8 15 Å Mn_3Ge DW velocity dependence for H_x and H_y. 60
Figure 4.9 7.5 Å Mn_3Sn DW velocity dependence for H_x and H_y 61
Figure 4.10 20 Å Mn_3Sb DW velocity dependence for H_x and H_y 62

Figure 4.11. Top view illustration of current driven DW motion. 65
Figure 4.12 DW velocity dependence with a capping layer identical to the CTL. 66
Figure 5.1 Domain Wall motion dependence on W and Pt overlayers 70
Figure 5.2 DW velocity dependence on H_x and H_y for 20 Å W, 5 Å Pt, 10 Å Pt. 71
Figure 5.3 Mn_xSb DW velocity vs current density *J*. 72
Figure 5.4 20 Å Mn_xSb DW velocity dependence on H_x for and H_y. 73
Figure 5.5 DMI field, H_{DM} as a function of Mn_xSb composition. 74
Figure 6.1 Post annealing P-MOKE signal for two films of Mn_3Ge. 76
Figure 6.2 DW velocity for 20 Å Mn_3Ge Heusler film annealed at 425 °C. 78
Figure 6.3 ↑↓ and ↓↑DW velocity vs H_x and H_y applied in plane fields 79
Figure 7.1 Depiction of an ↑↓ (⊙|⊗) Domain Wall. 81
Figure 7.2 1-D model simulation of results from Figure 4.8 andFigure 4.9 82
Figure 7.3 1-D model simulation of results from Figure 4.10 andFigure 4.12 83
Figure 7.4 1-D model simulation of results from Figure 5.2 andFigure 5.4 85
Figure A.1 P-MOKE hysteresis loop for 20 Å Mn_2CoSn. 88
Figure A.2 H_x, Hy DW velocity for CoSn | $Mn_{2.0}Sb$, CoAl | $Mn_{2.7}Sb$. 89
Figure B.1 Cartoon of current driven DW motion for small H_x or H_{DM} and pinning .. 95
Figure B.2 Cartoon of current driven DW motion for H_x or H_{DM} 96
Figure B.3 Cartoon of current driven DW motion for H_k or H_y only 97

List of Tables

Table 3.1 CTL candidates with a B2. 33
Table 3.2 Theoretical calculated values for the Mn_3Z tetragonal structure. 33
Table 3.3 Chemical Templating Layers 34
Table 4.1 Spin polarization direction, DMI, SHA and SOT contribution. 68
Table B.1 List of fitting parameters for the fits of Figures 7.2 - 7.3 98
Table B.2 List of fitting parameters for the fits of Figures 7.3 - 7.4 and Figure A. 99
Table B.3 List of fitting parameters for the fits of Figure 7.4 100

Abbreviations

AFM	Atomic Force Microscopy
CTL	Chemical Templating Layer
DMI	Dzyaloshinskii-Moriya interaction
DW	Domain Wall
LLG	Landau-Lifshitz-Gilbert equation
P-MOKE	Polar-Magneto Optic Kerr Effect
PMA	Perpendicular Magnetic Anisotropy
SHE	Spin Hall Effect
SHA	Spin Hall Angle
SOT	Spin Orbit Torque
UHV	Ultra High Vacuum
v-STT	Volume Spin Transfer Torque
XRD	X-ray Diffraction

Abstract

In this thesis, is shown a novel chemical templating technique where bulk like magnetic properties in tetragonally distorted Heusler films can be achieved. This chemical templating technique is so effective and is demonstrated for the successful growth of single unit cell thick Heuslers. This is achieved by growing the Heusler films on atomically ordered X'Z', with X'=Co, Z'=Al, Ga, Ge, Sn, underlayers that template chemical ordering within the Heusler films, even at room temperature. X' is a transition metal and Z' a main group element. The Mn_3Z family of Heusler alloys is mainly investigated, with Z=Ge, Sn, Sb. These tetragonally distorted ultra-thin Heusler films display excellent perpendicular magnetic anisotropy.

Furthermore, nanowire racetracks are fabricated from these films and the current driven domain wall motion is demonstrated. The highest domain wall velocities achieved are -129 ms^{-1} and the lowest current density to initiate the motion is $2.8 \cdot 10^{6}\mathrm{A\ cm}^{-2}$. The direction of the domain wall motion is determined by the bulk spin polarization of the Heusler. Moreover, the domain wall motion shows contribution by chiral spin orbit torques when studied applying in-plane magnetic fields. A bulk in origin Dzyaloshinskii-Moriya interaction and a spin Hall effect deriving from the chemical templating layers are identified.

These results are the first demonstration of domain wall motion in ultra-thin Heusler alloys with complex and tunable magnetic properties. One example of their extraordinary abilities is shown by systematically tuning within an order of magnitude the Dzyaloshinskii–Moriya field strength, by varying the composition of the Heusler alloy. Since the Heusler properties are intimately connected to the atomic scale ordering of their constituent elements, this work is an important step to enable Heusler spintronics applications.

Introduction

Spintronics refers to the study of the role played by the electron spin in solid state physics and spintronic devices are in the heart of several memory-storage technologies, most profoundly in the read heads and memory-storage cells using the giant magneto-resistance (GMR) in sandwiched multilayered structures[1–4]. Spintronic devices allow device element scaling beyond those achieved by conventional charge-based devices. Two important spintronic applications are identified, the magnetic random-access memory (MRAM)[5] and the racetrack memory[5,6]. Current efforts in designing and manufacturing spintronic devices for novel memory technologies and applications, are either perfecting the existing GMR-based technology or developing new magnetic materials.

Spin-transfer torque magnetic random-access memory, one of the most promising nonvolatile memory technologies, is already in production by several companies and has a reading performance that approaches that of dynamic random-access memory (DRAM). A magnetic tunnel junction (MTJ) is at the core of these MRAM memory elements. The magnetic materials used, should have large enough stability to sustain low dimensions device scaling without allowing thermal fluctuations to perturb the memory element. Additionally, large perpendicular magnetic anisotropy (PMA) is a prerequisite, allowing for reduced currents, to switch the magnetization of the electrode using spin torques[7,8].The best MTJ candidate electrodes to date, are alloys of Co, Fe, B and are used on either sides of an MgO tunnel barrier[7,9], and may also utilize interfacial layers. The PMA of CoFeB or similar Co, Fe, B alloys arises from the interfaces between CoFeB and the MgO tunnel barrier and/or interfaces with them. Device scaling below $\lesssim 20\,\mathrm{nm}$ will set the PMA to become too weak to overcome the superparamagnetic limit. Magnetic materials, in which PMA is derived from volume magnetocrystalline anisotropy are exemplary candidates that can overcome this challenge.

This is the case for the tetragonal Heuslers studied here. While many Heuslers are cubic, making their PMA zero, some compounds are found to be tetragonally distorted in their minimal-energy configurations and thus could have large PMA with their corresponding tetragonal lattice parameters a_t and c_t' while the $a_c$cubic lattice constant should match the MgO, which is commonly used for MTJs. This study is based on the findings of tetragonal distortion in Heusler compounds X_2YZ predicted by density-functional theorem calculations[10,11] and specifically the Mn_3Z Heusler family, where Z=Ge, Sn, Sb. The tetragonal distortion in Mn-based compounds can be linked to a band Jahn-Teller distortion[12,13] and to peak-and-valley character of the density of states in these compounds, in the cubic phase[10,11]. For this theory to be applied, the chemical order of the cubic phase that corresponds to the tetragonal lowest energy configuration must be the same for the latter. Also, the same applies for the configuration of magnetic moments, and satisfies the lightest-atom rule[14]. Anti-ferromagnetic coupling of the two Mn atoms, which leads to ferrimagnetism is found for the Mn_3Z used in the current study. Hence, it is essential that the Heusler is chemically ordered. Lastly, the extraordinary abilities of the Heusler class of alloys, of high tunability and high spin polarization makes them suitable for spintronic applications[15–18].

The scope of this study is two-fold. First to enable ultra-thin growth of Heusler films with near-bulk like properties even when grown at single unit cell thicknesses. And secondly, to demonstrate their spintronic application by means of domain wall motion in a racetrack, mainly focusing on Mn_3Z (Z= Ge, Sn, Sb).

It is shown that chemically ordered Heusler films can be grown on atomically ordered X'Z' underlayers, where X' is a transition metal and Z' a main group element. Indeed, using X'=Co, Z'=Al, Ga, Ge, Sn, underlayers that template chemical ordering within the Heusler films, even at room temperature, great PMA is found even for unit cell thick Heuslers. Up until now, PMA has been observed in films too thick to be technologically useful[19–27]. It has been shown that $L1_0$ ordered MnGa was grown showing PMA on CoGa buffer layers by Suzuki *et al.*[28–30] with the postulation that Ga terminated layers account for the successful growth.

Using a chemical templating technique, single or few unit cells thick Mn_3Ge, Mn_3Sn, Mn_3Sb Heuslers are grown with excellent PMA. The current induced Domain Wall

(DW) motion is studied in racetracks from these films. Due to their ferrimagnetic nature, they can exhibit very narrow DWs, low moment and allow for high density applications. For the first time, the DW motion for ultra-thin PMA Heuslers is observed and remarkably, DW velocities of -129ms^{-1} are found. Furthermore, the lowest current density finding for the Heusler DW motion, when compared at 100 ms^{-1} with the best conventional ferromagnetic Co/Ni/Co racetrack[31], is ~ 6 times more efficient. Even when one accounts for their lower magnetic moment of about 3 times, the ultra-thin Heuslers studied move 2 times more efficiently.

The racetrack memory studied here, is a nonvolatile magnetic memory. It consists of magnetic nanostrips, considered of material with PMA, containing magnetic domains ↑ or ↓, and the magnetization transitions from one domain to another, the DWs. The DWs move by injecting current pulses and thus, shifting the magnetic domains. The magnetic domains themselves, represent the magnetic stored bits of information, "0" and "1" for the two magnetization states and can be moved in a lock-step motion, to the reading and writing locations[6,32].

1. Deposition Growth and Measurement Setup

In this chapter, the main techniques used for growing and characterizing these Heusler films are explained. The sub sections following are introduced, starting from a single substrate, then deposition, following with characterization of the deposited film and characterization measurements to optimization, and finally fabrication and Domain Wall velocity measurements. In such way the entire study can be followed and can give insight for future reference and further development.

Physical methods of film deposition can be generally described as a target being connected to a negative voltage supply (dc or rf), and a substrate facing the target. Ar gas is introduced to provide a medium where a glow discharge can be initiated and maintained. Typical gas pressures of a few millitorr to 100 mTorr are used (3 mTorr in our case). When the plasma is ignited, or the glow discharge has started, positive Ar^+ ions strike the target and remove mainly neutral target atoms by momentum transfer (physical method of film deposition). These atoms then travel, diffuse towards the substrate where they start forming thin films. Secondary electrons are accelerated away from the target since it is held at high negative potential. These electrons help to sustain the plasma-glow discharge by ionizing neutral sputtering gas atoms which in turn bombard the target and release more secondary electrons in an avalanche process.

1.1. Material growth techniques

Most of the study was performed on MgO (001) substrates from Crystec. They are 10x10 mm in size, made by arc fusion. The cleavage process leaves them with (100) orientation. They are cubic, with a density of 3.58g cm^{-3} and a lattice constant of a=0.4212 nm and are one sided epipolished. The substrates are prepared by sonication in Methanol for 30 minutes. Then transferred to hot Isopropyl Alcohol vapor degreaser for 2 minutes and lastly dried by hot N_2 gas at ~60-70 °C. Afterwards, the substrates

are transferred in the LoadLock under Ultra High Vacuum (UHV). The last step before the deposition is a substrate annealing step at 650 °C for 30 minutes and the final cooldown to ambient temperature (below ~100 °C) before starting the deposition.

Silicon substrates Si (100) wafers are also used mainly for calibration but also shown in this study. They are covered with ~250 Å SiO_2 and for preparation, are first subjected to UV light, then dipped in de-ionized water to wash away the organic residues. Finally transferred to hot Isopropyl Alcohol vapor for 2 minutes and lastly dried by hot N_2 gas at ~60-70 °C.

UHV is defined as base pressure below 10^{-9} Torr. There are about $3\ 10^{19}$ molecules cm^{-3} at atmospheric pressure ~770 Torr. In UHV, this is reduced to $3\ 10^{7}$ molecules cm^{-3} which is approximately 12 orders of magnitude reduction. Each order of magnitude decrease in pressure, is a decrease in molecules in volume. Incident flux describes the number of incident gas molecules on a unit cross-sectional area at 20 °C. This is directly proportional to the chamber pressure. This flux is approximately 1 monolayer sec^{-1} at 10^{-6} Torr. The lower the chamber pressure, the lower the incident flux, *I*. In the case of UHV, at 10^{-9} Torr, *I*~1/1000 monolayers sec^{-1}. That means it will take hours to form a layer of gas on the substrate surface[33,34].

1.1.1. Magnetron Sputtering

Sputtering refers to the method of deposition that uses ions impacting a surface to create a chain of collisions in a target material, thus emitting atoms from the target material into the chamber. There are two main types of sputtering, categorized by the source of the power supply in use: DC, and RF. The sputtering system includes a sputtering gun where the target lies and unbalanced magnetrons[35] (referring to the magnetic field used to enhance sputtering) are used. Plasma discharge or simply, plasma is the collection of ionized gas, ions, electrons and neutral atoms that is overall electrically neutral. A plasma must be created for sputtering to begin, a process called striking the target.

Magnetron sputtering uses magnetic fields in conjunction with electric fields to enhance the sputtering process. It is the most widely used commercial method of sputtering as it can allow lower deposition pressures (1-3 mTorr) and has high deposition rates. Sputtering at low pressures produce dense and tightly bound thin films. The atoms mean free path is proportional to the pressure and the atoms can travel 1-10 meters without colliding with other atoms or gas molecules at 1-3 mTorr pressures[36,37]. The magnetic field is created by permanent magnets behind the target and causes the electrons to follow a helical path due to Lorentz force. The track of electrons is where most of the sputtering occurs, since most of the ionization of gas happens there, thus forming the characteristic circular ring on the target from sputtering. The deposition control is performed by shutters and all magnetron depositions are operated at 3 mTorr, using constant power mode in the sputtering power supplies.

The deposition chamber capabilities include in situ annealing of the substrate, DC or RF magnetron sputtering, Ion Beam Deposition (IBD) from single targets (elemental or alloys) but also DC magnetron co-sputtering of up to 3 different targets.

DC

In DC sputtering, the target gun is powered by a DC power and produces plasma through a large voltage difference. The target is brought to a high, negative potential while the outer parts of the sputter gun are grounded. The argon gets ionized and the plasma is created above the target. The collision of Argon ions from the plasma begins the deposition process· the Ar ions collide with the target material on the gun. The collision transfers kinetic energy from the Ar ions to the target material and target atoms are emitted into the vacuum chamber[38]. These atoms which are mostly neutral, scatter in all directions away from the target and will deposit onto the substrate facing them, creating a thin film made from the target material[37].

DC magnetron sputtering is used for the following material growth as discussed in this study: $Co_{51}Al_{49}$, from a CoAl alloy target with composition 45:55.

$Co_{53}Ga_{47}$ from a CoGa alloy target with composition 55:45.

Mn_3Sn from MnSn alloy target with composition 3:1.

$Co_{51}Sn_{49}$ from co-sputtering of Co and Sn single elements.

$Co_{50}Ge_{50}$ from co-sputtering Co and Ge single elements.

Mn_3Sb from co-sputtering of three single element targets, Mn, Mn and Sb.

Pt and W were grown from single element targets.

RF

RF sputtering is used for sputtering insulating materials. When an insulating target is kept at a negative applied potential, it accumulates positive ions at the surface and saturates, blocking any sputter deposition. RF sputtering uses an oscillating radio frequency signal, similar to an AC signal. The oscillating signal allows the target to remain at negative potential for most of the time, while briefly switching to positive potential "sweeps away" forming ions from the target surface. RF also gets the electrons to oscillate, ionizing collisions, helping to sustain the plasma. RF can couple any type of impedance, so the sputtering process can be performed from any type of insulating material, regardless its resistivity.

RF magnetron sputtering is used for MgO overlayer and some of the underlayers from an MgO RF-target alloy of composition, 50:50.

The target composition is not replicated onto the film sample. An alloy target is not removing equivalently to its composition, atoms from its constituting elements, when the kinetic energy to be transferred is constant. Heavier atoms travel slower but are less prone to scattering with gas molecules. One has to anticipate the sample composition and then adjust by varying the sample to target distance as well as the angle of the deposition which is possible in the sputtering system used.

1.1.2. Ion Beam Deposition

For ion beam deposition (IBD) in the deposition system used, the ion beam is an inert gas (Kr), at high energy (several hundreds of eV). The beam is directed at the target of the desired material, which is sputtered. The first step is the production of the ions, by electron impact ionization. An inert gas, (Kr) is used to create a discharge so plasma fills the ion source chamber by RF discharge. The electrons, highly mobile, pick up sufficient energy during their oscillations in the RF field to cause ionization. Electrons are constrained by a magnetic field to enhance the ionization efficiency. Kr ions formed by collisions with the electrons are attracted to a grid system with parallel plates, the first of which is the screen grid. Aligned to the screen grid, at a small distance (~0.1 cm) is the acceleration grid. Lastly, a deceleration grid is also aligned, and the resulting beam has the desired shape and energy. The resulting beam is a Kr ionized beam. A neutralizer is used to add electrons from a thermionic filament (usually tungsten) to neutralize the beam and to avoid beam spreading. Low (background) gas pressure can be maintained to avoid excessive scattering, divergence and contamination. The latter results in less gas incorporation in the grown film[36,39]. Sputtering insulating targets requires the beam to be neutralized to avoid charge build up on the target surface which would cause beam deflection[36,37,39].

Generally, ion beam deposition allows for greater isolation of the substrate from the sputtering process, in this case more control over the gas pressure, substrate temperature, type of particle bombardment and control over the ion beam itself. Thus, IBD allows for more flexibility in the sputtering processes and the higher energy of arrival of the sputtered particles allows for better adhesion to the film growth. The non-unlimited capabilities of the system used, fast-paced research and different projects sharing the same deposition tool, could not allow for preferential IBD use for most of the growth in this study.

IBD was used for some of the MgO underlayers with equal results to the RF MgO underlayers from an IBD MgO target with composition of 50:50.

Mn_3Ge was grown with IBD from an IBD target of composition: 67:33.

Ta capping layer was grown by IBD from a Ta target.

Cr buffer layer also was grown by IBD from a Cr target.

1.2. Characterization Techniques

Characterizing the deposited films is the most essential step to achieve the required properties, namely the Heusler growth with great perpendicular magnetic anisotropy. Before the magnetic film stack growth, calibration films of each layer are grown to determine thickness and composition. After the magnetic film stack growth, the magnetic and structural properties of the film can be determined. In a way, exploring the film properties can give insight to the next deposition parameters to obtain the proper sample growth.

1.2.1. Profilometer and Resistivity measurements

Shadow masked deposition onto Silicon substrates of the layer to be calibrated, provides an area where vertical profiles can be measured for thickness calibration and an open area where the film is deposited and can be used for sheet resistance measurements using a 4-probe setup.

A DEKTAK profilometer was used to measure the film thicknesses on typically 500 Å film of the material to be calibrated. The masked deposition results in a pattern which can be measured in the profilometer.

Based on the sheet resistance and thickness of the calibration film, the resistivity of the layer grown is determined.

1.2.2. RBS-PIXE

Rutherford backscattering spectrometry (RBS) is used to determine the composition of the deposited layers, usually from the calibration substrate films[40,41]. RBS was performed for thin films of the materials to be used either in calibration films of the layers or directly onto the grown Heusler film stack, like in the case of Mn_xSb shown in section 5.2 and can provide elemental composition of the constituting materials in these thin films when combined with Particle Induced X-Ray Emission (PIXE)[42,43].

RBS detects the energies and amount of the backscattered ions from the substrate of all its deposited layers. An incident mono-energetic light ion beam, typically in the MeV energy range for He ions is directed onto the substrate. The energy of the scattered He particles from the substrate is analyzed by a solid-state particle detector positioned at a backscattered angle with respect to the incident ion beam (typically ranging from 100-170° depending on the specific analysis). The working principle and analysis, depends on the conservation of energy and momentum for the backscattered He ions. The energy transfer is between the incident ion (He) and the scattering atom (from the substrate) and can be related to the depth and mass of the substrate/target. The number of backscattered ions is proportional to the concentration of its constituting elements.

In parallel to the RBS energy spectra, particle induced X-ray emission is used. It is a technique which relies on the spectrometry of characteristic x-rays emitted by the target/film-substrate elements due to the irradiation of a high energy ion beam (1-2 MeV of He). PIXE can identify the different element intensity peaks in a compound target. Since there is little overlapping of the characteristic x-rays for different elements, simultaneous detection of all elements in multilayer samples is possible. PIXE was used with the appropriate corrections to absorption and x-ray yields to also give a quantitative analysis.

In this thesis, PIXE is used in conjunction to RBS for most of the compositional analysis, since most of the layers used to promote growth and the Heuslers, have overlapping RBS energy spectra and only PIXE allows identifying the constituting elemental composition.

1.2.3. Magneto-optic Kerr effect for P-MOKE and Kerr microscopy

The Magneto-Optic Kerr Effect (MOKE)[44–46] describes the rotation of the plane of polarization of the incident light as it is reflected by a magnetic substrate. In Polar or Perpendicular MOKE (P-MOKE), the magnetic field is applied out-of-plane (along the easy axis for PMA materials). The rotation angle, degree and direction, depends on the magnetization magnitude and direction of the local magnetic domain.

The polarization of the incident light is rotated by a small degree when it reflects off the surface of the magnetic sample. In Figure 1.1a, is shown a vector representation using the concept of a Lorentz force, acting on light agitated electrons. A polarized light beam will induce electrons to oscillate. The Electric Field, $\boldsymbol{E}$, of the plane polarized light which is incident, can be thought as exciting the electrons so that they can oscillate parallel to the incident polarization. Typically reflected light is polarized in the same plane as the incident light which gives the normal component in the reflected light. An added small component which is perpendicular to both the normal component and direction of magnetization arises because of the Lorentz force. This is the Kerr component. Generally, the two components are not in phase and their superposition gives rise to magnetization dependent rotation of the polarization. To collect the maximum signal, the incident light or laser excitation is aligned perpendicular to the sample plane $\vartheta_i \sim 0$ (normal incidence) and the polar Kerr effect is independent of the incident polarization.

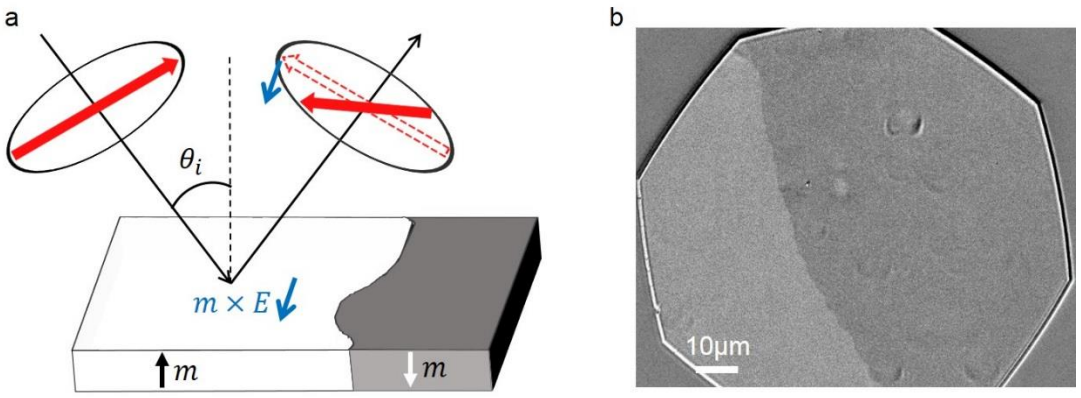

Figure 1.1 (a) Illustration of the Magneto optic Kerr Effect representing the rotation of the plane of polarization. (b) Kerr microscopy image of a blanket PMA Heusler film, showing two opposite magnetized domains as different contrasts. The octahedron shape shown is from the partially closed diaphragm.

In MOKE microscopy[45,47], light passes through a polarizer which transmits only plane polarized light which through the optical setup is guided towards the sample stage where it is reflected from the substrate. The interference of the normally reflected component and the Kerr component results in the magnetization dependent polarized light rotation. Using an analyzer in the collected light leads to contrast between opposite magnetized domains. The Kerr images obtained appear essentially as different shades of grey which represent the differently magnetized domains as shown in Figure 1.1b for a PMA Heusler blanket film (deposited film on the substrate before any patterning takes place). The direction of magnetization within the domains governs the direction in which the plane of polarization of the incident light is rotated. Digital image enhancement helps in distinguishing the two different regions.

1.2.4. Atomic Force Microscopy

The properties of thin films and their potential application in devices is strongly influenced by their surface properties and very importantly by the surface roughness. Atomic Force Microscopy (AFM) was used throughout the study for the morphological

study of the growth of Heusler materials and their underlayers. AFM is a scanning probe microscopy technique where the surface of a sample is probed with a sharp tip[48].

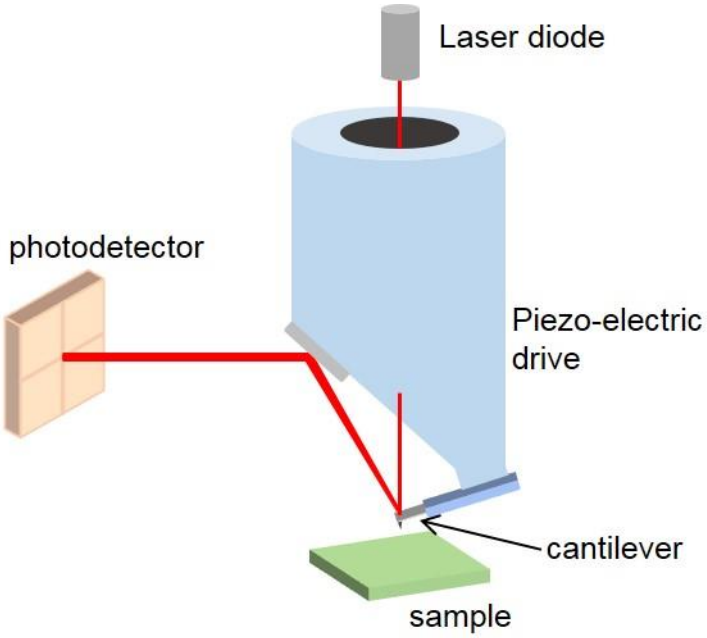

Figure 1.2 Illustration of an atomic force microscope.

The tip is located at the free end of a cantilever. When the atomically sharp tip is brought into proximity of a sample surface, the forces between the tip and sample lead to a deflection of the cantilever according to Hooke's law. The tip and sample are moved relative to each other in a raster pattern so that it scans the chosen area in close contact with the surface. The tip and the sample are brought into proximity with a piezoelectric drive and the force between the tip and the sample surface is usually 10^{-9} to 10^{-6} N (for example due to Van der Walls force at distances of a few nanometers) and is not measured directly by the detection system. Instead, the deflection of the microcantilever is sensed by the reflection of a laser beam, pointed at the mirrored back side of the cantilever and detected by a position sensitive (four-quadrant) photodetector. In this arrangement, a small deflection of the cantilever will change the position of the reflected laser beam on the photodetector. Using Tapping mode imaging in ambient air, the cantilever oscillates at or near its resonant frequency at a high amplitude (tens of nanometers), normal to the sample surface using a piezoelectric crystal. A feedback loop maintains a constant amplitude without changing the frequency by the movement

of the z-piezo-electric drive which gives the sample topography and is displayed as a function of the lateral position of the tip/sample.

All morphological studies were performed ex-situ, on a Bruker Dimension Icon. A 2x2 μm scan window was selected in all cases and the surface roughness, r_{rms} was measured. To get atomically smooth layers and films, the deposition and annealing process were optimized, the results are shown in Figure 3.8.

1.2.5. X-ray Diffraction

To enable ultra-thin growth of PMA Heusler materials, the underlayers (CTLs) are shown to be ordered in the CsCl structure of alternating layers as discussed in chapter 3. The crystalline structure of the highly epitaxial films grown in this study can be determined by X-ray diffraction (XRD). Crystalline materials are characterized by the orderly periodic arrangements of their constituting atoms. The smallest group arrangement of atoms that gives the overall symmetry of a crystalline material is the unit-cell. Parallel planes of atoms intersecting the unit cell define the plane directions. In the X-ray diffractometer, X-rays are generated in a cathode ray tube with the target material (Cu K_α anode with a characteristic wavelength of 0.15406nm for the diffractometer used for this study). Passing by a K_β filter, monochromatic Cu K_α radiation collimated X-rays are directed towards the sample. In the Bragg-Brentano geometry, the source to sample and sample to detector distance are at a fixed radius.

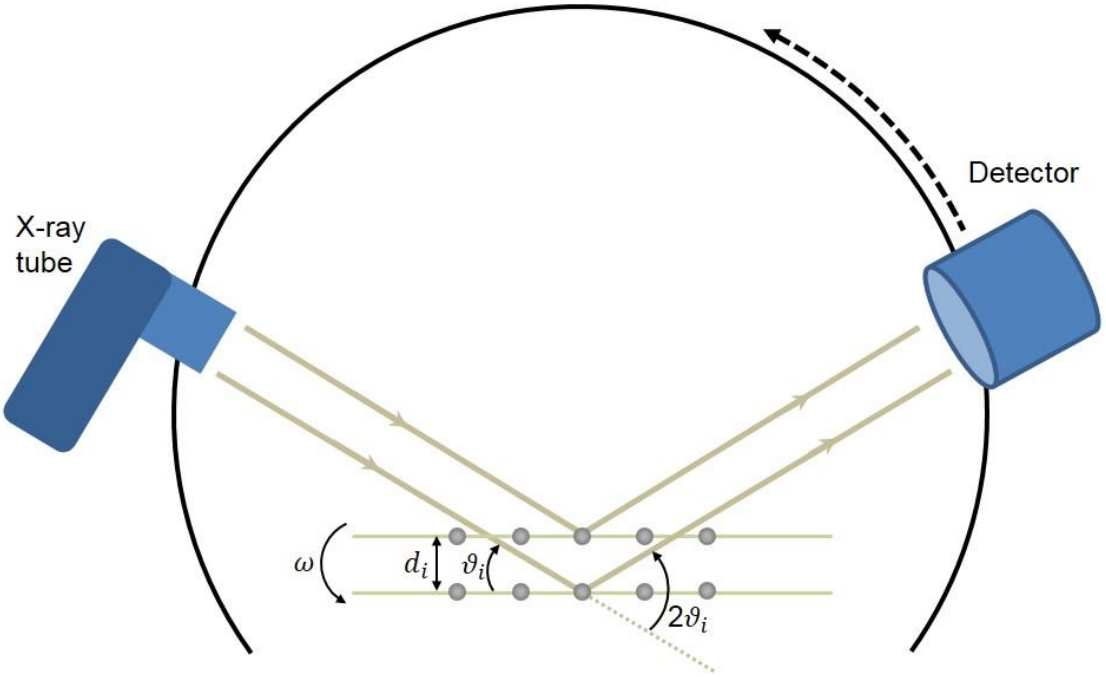

Figure 1.3 Illustration of a Bragg-Brentano geometry XRD setup. A family of planes from the crystal surface that satisfies Bragg's law is illustrated (not in relative scale).

As the sample and detector rotate, the diffracted intensity of the reflected X-rays versus $2\theta_i$ is captured by the detector. A family of planes (planes of atoms), as illustrated in Figure 1.3, produces a diffraction peak only at a specific angle θ_i which satisfies Bragg's law: $n\lambda = 2\, d_i\, sin\theta_i$, where for parallel plane of atoms with spacing of d_i between planes there is constructive interference. λ is the X-ray wavelength, d_i is the distance between the crystal planes, θ_i is the angle between the incident X-rays and the crystal surface, n is an integer, showing the order of diffraction. The spacing between the diffracting planes of atoms determines the XRD peak positions.

Coupled 2θ (θ-2θ) geometry of the X-ray diffractometer is used such that the sample rotates in the path of the X-ray beam at an angle ω while the X-ray detector rotates at an angle 2 θ. The incident angle θ is the angle between the X-ray source and the sample. The diffraction angle 2θ is the angle between the X-ray source and the detector. XRD measurements were performed using a Bruker general area detector diffraction system (GADDS) or a Bruker D8 Discover system, both ex-situ, at room temperature and the collected diffraction patterns are shown in chapter 3.3.

1.3. Domain Wall Motion Measurement Setup

Deposited blanket films, smooth and with great PMA as seen from P-MOKE are brought under the Kerr microscope. Two different magnet arrangements can apply in-plane and out-of-plane fields. The blanket film is viewed using the out-of-plane magnet arrangement to switch the PMA film while imaging with the Kerr microscope. The contrast between the two states, of magnetization Up (↑ or ⊙) and Down (↓ or ⊗) is adjusted and optimized. The single crystal MgO substrates are translucent as the rear side is not polished. Therefore, a lot of light is scattered, and the overall contrast is reduced. Double side polished substrates, with an additional reflective coating on the rear side can enhance the contrast. As an alternative, viewing the domains on the blanket film aides to adjust the polarizer, aperture, and image acquisition settings (like digital contrast, exposure and image averaging).

1.3.1. Kerr Microscopy

The Kerr microscope uses the magneto-optical interaction for the Kerr effect. A camera is adjusted, and digital imaging is used.

Kerr digital images of blanket films in differential mode

Imaging magnetic domains in this study faces two main challenges. One is the translucent MgO substrates and the second is the nature of these Heusler magnetic materials, being very thin films, and having low moment. Thus, in most cases, magnetic domain contrast was faintly visible to the bare eye. Differential imaging is used to enhance the contrast. In differential mode, firstly the sample image with its current magnetic state is acquired. Then this image/magnetic state is digitally subtracted and any change in the magnetization of the sample appears as enhanced contrast over the

subtracted image/state. Averaging a few numbers of frames keeps the noise level very low and the image appears smooth. An example of differential imaging is shown in Figure 1.4. In Figure 1.4a, region I represents a magnetized Up (⊙) domain. Region II and III is the same magnetized Down (⊗) domain, after image the subtraction, an external field to expand the Down domain in region II was applied and appears as bright contrast.

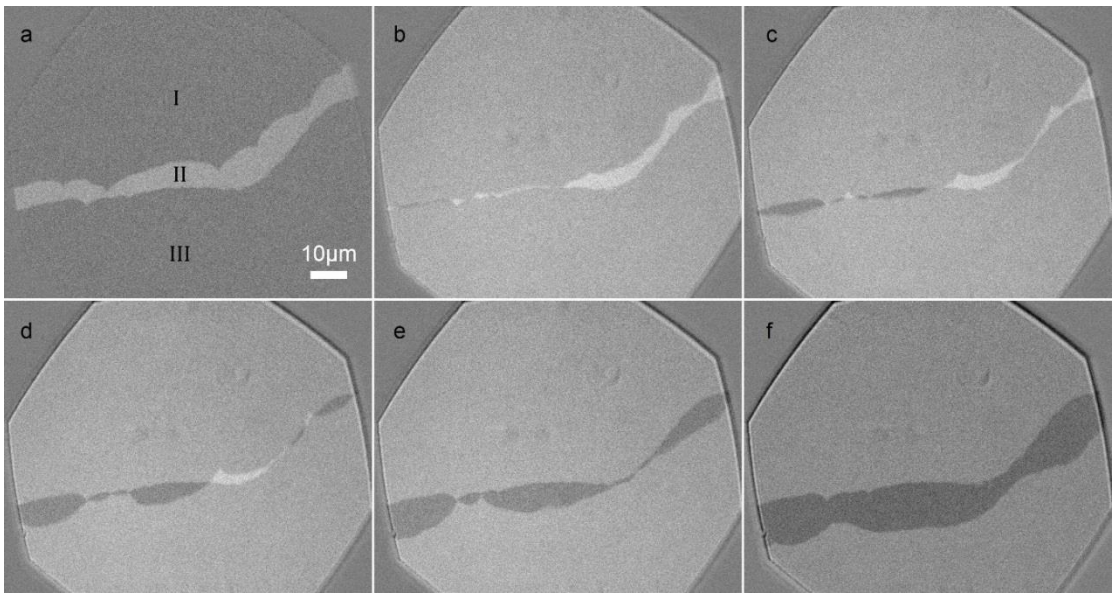

Figure 1.4 (a) – (f) Kerr images in differential mode showing sequentially the propagation of an Up (⊙) domain from region I, shrinking in size the Down (⊗) domain (in bright) region II until it expands over the previous subtracted contrast of down domain, appearing now dark for the Up (⊙) domain over region III.

When the Domain Wall propagates, expanding one magnetic domain, ⊗ domain replacing ⊙ domain appears as bright contrast. ⊙ domain replacing ⊗ domain appears as dark contrast for the given Kerr contrast rotation. For materials with opposite Kerr rotation, it is the inverse, as example, Mn_3Ge and Mn_3Sn have opposite Kerr contrast compared to Mn_3Sb, seen in Figure 4.1 -Figure 4.3.

Kerr imaging of the Domain Wall propagation in nanowires

In Figure 1.5a, is shown the Domain Wall propagation as observed in a Kerr microscope in differential mode for a magnetic Heusler wire. The position of the DW is indicated by a dotted line. In Figure 1.5b, the same images are overlaid to indicate the magnetization direction. The initial magnetic state of the wire is taken at t_0 and subtracted from the subsequent images. Application of current pulses t_1 through t_4 move the DW to the right and this appears as an expansion of the domain in the differential Kerr image. The DW velocity is calculated measuring the distance the DW has travelled, from the expansion of the magnetic domain, for the integrated pulse time duration.

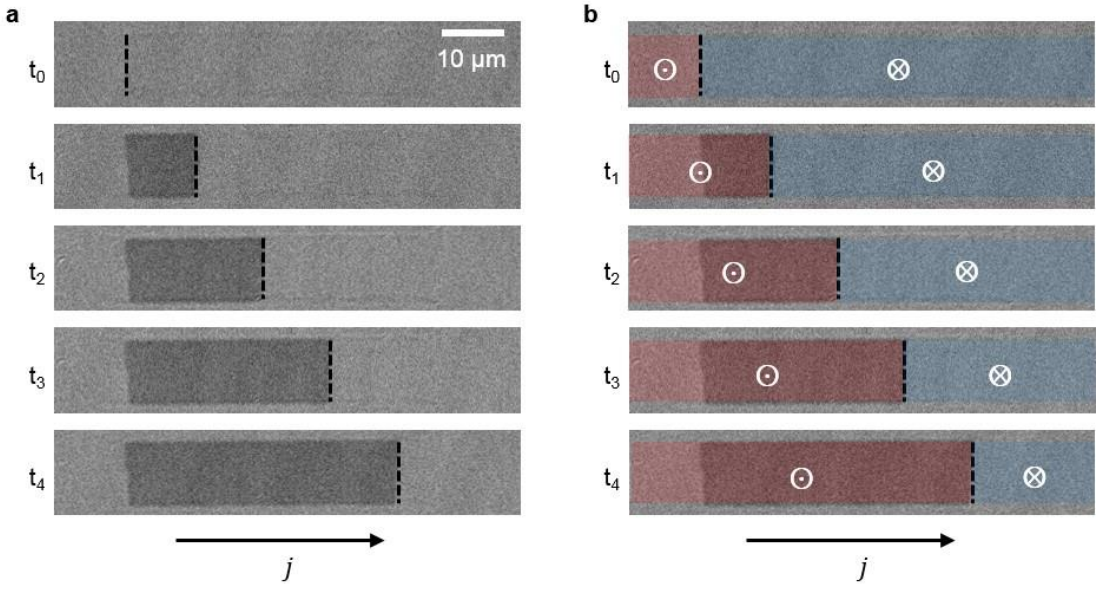

Figure 1.5 (a) Differential mode Kerr microscopy showing the domain expansion using a series of current pulses in a wire, showing with a dashed line the DW position. (b) The same image, overlaid with the representation of the domains.

1.3.2.Pulse Generator and Circuitry

For the DW motion measurements, nanosecond long voltage pulses were generated using a 10,300B Picosecond Pulse Laboratory generator with maximum applied voltage

of $+50, -45$ Volts and risetime of less than 300 picoseconds. Pulses of variable length of 2 to 100 nanoseconds can be applied.

In addition, for the single DW injection, an AVTECH AVOZ-A3-B 100 Volt pulse generator was used for DW nucleation referred to in section 4.1.1.

In conjunction to the pulse generator, a small DC current (0.1 – 10 μA) was applied to the sample via a Picosecond Pulse Labs bias tee to simultaneously measure the device resistance as shown in the schematic in Figure 4.7a. An oscilloscope in series was also used to examine the pulse shape. The current density is calculated as $J = {}^{2V_{\mathrm{p}}}/_{R \cdot t \cdot w}$, V_{p} being the applied pulse, R the measured resistance, t the thickness of the conducting materials and w the width of the wire. The thickness of the conducting material is the overall thickness of the underlayer (CTL), magnetic material (Heusler) and overlayer if any. The 20 Å Ta protective capping layer is always considered to be fully oxidized, thus is not accounted in calculating the current density.

1.4. Fabrication and patterning

Heusler films with great PMA were patterned into wires for Domain Wall motion experiments using multilayer optical lithography. In the DW motion experiments, the substrates used are MgO (001), thus an improved processing technique was developed to better fabricate these samples.

With the lithographic process, the pattern from the photo-mask (mask) is transferred into the resist (polymer film) to finally replicate the pattern on the underlying thin film/substrate. Photolithography (or optical lithography) uses ultraviolet radiation (360-410 nm) to transfer the pattern from the mask to a photosensitive resist. In contact printing, the mask is pressed in hard contact with the resist which is spin-coated onto the wafer.

The fabrication process is illustrated in Figure 1.6, starting from the substrate with the blanket deposited film, Figure 1.6a. At first, HMDS (hexamethyldisilazane) which

promotes adhesion of the subsequent resists, is applied onto the wafer using a YES HMDS vapor priming oven, forming a monolayer. HMDS chemically bonds its Si atom to the oxygen of oxidized surfaces and forms a hydrophobic surface, improving resist wetting and adhesion. Then ~50nm of PMGI resist is spin coated to serve as an undercut and release layer to provide a clean lift off. The last layer is the SPR670 photoresist where a thickness of ~0.62μm is spin coated. This trilayer technique developed for this work, improves resist adhesion and the lift-off process and is illustrated in Figure 1.6b. The mask contains nanowire devices in an area of 10x10 mm^2. Masked exposure in a Karl-Suss MA6 results in degrading the exposed areas of the positive photoresist which are then soluble to the developer (TMAH), leaving the non-exposed nanowires. Pre-exposure and post exposure bake were used accordingly. The result is the transfer of the mask pattern as resist patterns onto the wafer.

The wafer with the nanowire design protecting photoresist is inserted in a IONFAB 300 plus and argon ion milling is used in a similar concept as described for the IBD only in this case the ion beam is directly directed onto the substrate and chemically inert Ar^+ ions are generated. The argon ions are neutralized and accelerated towards the substrate. Upon arriving at the surface, through momentum transfer and when their energy is sufficient, substrate atoms, molecules and ions are ejected, and the material is etched, defining the devices. Because of the collimated beam of ions, the etch profile is essentially vertical. Secondary Ion Mass Spectrometry (SIMS) is used to monitor and stop the etching process when the bottom layer is reached and fully etched. The etched areas are refilled with IBD Al_2O_3 to the etched thickness, providing electrical isolation and protection for the devices. The last step is the resist lift-off, submerging the patterned wafer in NMP at ~45°C with ultrasonic agitation.

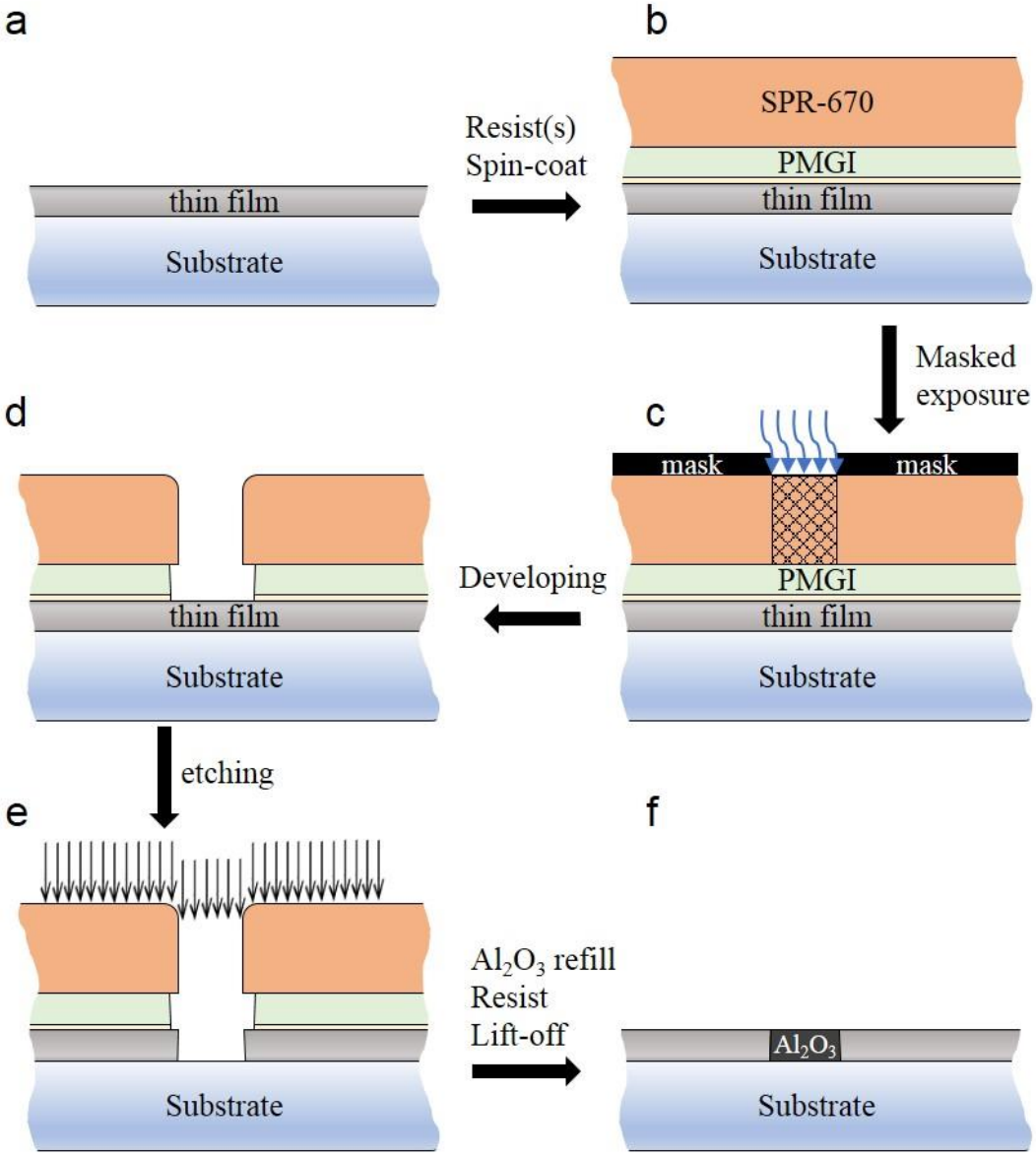

Figure 1.6 Fabrication process. (a) The deposited blanket film on the substrate. (b) Vapor primed HMDS, spin-coated PMGI and SPR670 photoresists. (c) Exposure through a mask. (d) Pattern profile after development of the exposed photoresist. (e) Ar ion etching, to define the devices. (d) Refill of the etched areas with Al_2O_3 and resist lift-off, leaving the desired device pattern on the film.

2. Magnetization Dynamics for the Heusler DW motion

Looking beyond the sole purpose of the Racetrack application, the study of the DW motion under applied current reveals the operating principles of spintronic devices. The current applied along the wire, generates namely two spin torques: a volume spin transfer torque (v-STT), which is the spin transfer from the magnetic domain adjacent to the wall carried by the spin-polarized current through the magnetic material. And a spin-orbit torque (SOT), from the Spin Hall Effect when current flows in usually heavy metals and underlayers. Using these two phenomena, we can describe the DW motion in these wires made from Heusler Alloys. Current induced DW motion studied in the Heusler nanowires is unique in a way that each contribution can be seen having a different effect on the DW motion and therefore, the respective contribution of each torque can be identified when examining the DW motion under externally applied in-plane fields.

Spintronics is a portmanteau of spin transport electronics and allows conventional electronic devices to have an additional degree of freedom, which is the electron spin. Electrons are fermions, described by the Fermi-Dirac statistics and conform to the Pauli exclusion principle. Besides their mass and charge, electrons have an intrinsic property, spin, which is quantized with its associated angular momentum. When observed along one axis, like *z*, it can only take the quantized values of $\boldsymbol{S} = \pm \frac{1}{2}\hbar$, namely spin Up and Down, with $\hbar = \frac{h}{2\pi}$, the reduced Planck constant. Along its spin axis, the electron has an intrinsic magnetic dipole moment which is equal to $\mu_z = \pm\frac{1}{2}\mathrm{g}\mu_B$ ~approximately equal to one Bohr magneton (μ_B). g is the gyromagnetic ratio for the electron spin-factor , with $\mathrm{g} \simeq 2$.

In materials like ferromagnetic elements or alloys, made of atoms with partially filled shells according to Hund's rules, when individual spin orientations show some type of

ordering, considering the Ising model, Up and Down spins are not balanced due to exchange interactions. This causes nearby spins to align parallel or anti-parallel to each other depending on the coupling constant of the Heisenberg exchange interaction and it results in a net magnetic moment. When a current flow is introduced, through such a material, the probabilities of scattering for electrons with spin Up and Down are different, because of the different mobilities of the majority and minority spins. Therefore, the two spin channels encounter different conductivities and the flowing current becomes spin polarized.

In ferromagnetic materials, the spins are aligned parallel within magnetic domains. In ferrimagnetic materials, the spins are aligned antiparallel, but the opposing moments are unequal and do not cancel, such that magnetization remains within magnetic domains. Both cases are considering below T_c, the Curie temperature point. The net moment can be defined by the vector summation of all the magnetic domains and the directional preference of the magnetization is the magnetic anisotropy. Magnetocrystalline anisotropy introduces a preferential direction for the magnetization along a crystal direction. Other anisotropies like the shape anisotropy from the material's geometrical shape, stress or exchange bias also contribute when present. Energetically preferred axes are called the easy axes of magnetization and magnetization tends to align along the easy axes under no external influence. When the moments of the material are aligned perpendicular to the plane of the film, the material is known to exhibit Perpendicular Magnetic Anisotropy (PMA)[49] and it can arise in instance from interfacial or magnetocrystalline anisotropies. For the thin Mn_3Z Heuslers that are studied in the current report, these are ferrimagnetic and have magnetocrystalline anisotropy that induces PMA as will be introduced in chapter 3.

For these strong PMA thin films materials, the transition between oppositely magnetized domains is where the magnetization gradually changes from one direction to the opposite and is known as the Domain Wall (DW)[50–52]. Thus, the DW, separates two magnetic domains and there are two types of walls: Bloch where the magnetization rotates perpendicular to the plane of the wall and about an axis in the plane of the film, and Néel where the magnetization rotates perpendicular to the plane of the film. Thus, in Bloch walls, at the center position of the DW, the magnetization lies perpendicular

to the wire length and in-plane of the film, while for Néel domain walls, the magnetization at the center of the DW lies along the wire length. In thin films, and patterned device wires where $x >> y >> z$, Bloch walls are generally favored[53]. For certain conditions (for example the presence of Dzyaloshinskii-Moriya interaction) or for certain thicknesses, the Néel configuration can be stabilized[54–56] and will be the case in this study as explained in a few paragraphs. The width of the DW is determined by the exchange energy and the anisotropy energy and is equal to $\pi\Delta$, where:

$\Delta = \sqrt{\frac{A}{K_{\text{eff}}}}$ is the DW width parameter[57].

A is the exchange stiffness and K_{eff} is the anisotropy constant. Therefore, large anisotropy leads to narrower DWs.

2.1. Landau-Lifshitz-Gilbert equation

The Landau-Lifshitz-Gilbert equation (LLG)[58] forms the basis for the dynamics of spintronic systems. To briefly introduce the evolution of a spin and its induced moment $\boldsymbol{m} = \gamma \boldsymbol{S}$ (γ is the gyromagnetic ratio, $\gamma = \mathrm{g}\frac{-e}{2m_e}$) in the presence of a magnetic field, $\boldsymbol{H}$, we can follow the classical derived torque on a current carrying loop from a magnetic field: $\boldsymbol{T} = \boldsymbol{M} \times \boldsymbol{H}$. Then classically, an exerted torque induces an angular moment $\boldsymbol{L}$, given by: $\frac{d\boldsymbol{L}}{dt} = \boldsymbol{T}$.

Equivalently, for the magnetization $\boldsymbol{M}$ in a ferromagnet:

$$\frac{d\boldsymbol{M}}{dt} = -\gamma \boldsymbol{M} \times \boldsymbol{H}_{eff}$$

That signifies that a magnetic moment (spin) in the presence of a magnetic field will start a precessional motion perpendicular to the magnetization and the effective field applied. Multiplying the last equation with $\boldsymbol{H_{eff}}$, leaves the angle between magnetization and field invariant. Therefore, in real systems, precession alone is not able to describe the dynamics since there is no dissipation. A second term is added to the equation,

which is damping and tends to align the magnetization with the magnetic field and is parametrized by α, the damping constant. The LLG equation is now formed as:

$$\frac{d\boldsymbol{M}}{dt} = -\gamma \boldsymbol{M} \times \boldsymbol{H}_{eff} + \frac{a}{M_s} \cdot \boldsymbol{M} \times \frac{d\boldsymbol{M}}{dt}$$

M_s is the saturation magnetization. Simply describing the LLG equation, for a magnetic moment under an applied field is shown to cause precession of the moment about the field axis, while the moment rotates/spirals into alignment with the field through damping processes.

2.2. Volume Spin Transfer Torque

When current flows through a ferromagnetic material, electrons will become polarized with the spin of the conduction electrons aligning with the spin of the local electrons. The degree of spin polarization is parametrized by *P* which through classical Bloch-Boltzmann transport theory, allows to separate the currents from spin-Up electrons and spin-Down electrons and thus, the degree of spin polarization via the current densities $\frac{J_\uparrow - J_\downarrow}{J_\downarrow - J_\uparrow}$ [59].When the electrons enter a region of opposite magnetization, they will transfer their spin momentum to the local magnetic moment, while the conservation of momentum holds. The mechanism is based on s-d exchange interaction between conduction electrons and the local magnetic moment.

When electrons traverse a DW, the conduction electrons will transfer spin angular momentum to the localized spins of the domain wall (adiabatic term as introduced by Berger and Slonczewski)[60–63]. The modified LLG equation[64,65], which describes the general effect of a polarized current on magnetic domain walls, accounts also for a non-adiabatic term, parametrized by a phenomenological non-dimensional parameter β, which was introduced to explain experimental results on current driven DW motion[66]. Below the Walker breakdown, the domain wall, should move in the direction of propagation of the electrons:

$$\frac{d\boldsymbol{M}}{dt} = -\gamma \boldsymbol{M} \times \boldsymbol{H}_{eff} + \frac{a}{M_s} \cdot \boldsymbol{M} \times \frac{d\boldsymbol{M}}{dt} + u \cdot \boldsymbol{M} \times \left(\boldsymbol{M} \times \frac{d\boldsymbol{M}}{dt} \right) + \beta \cdot u \cdot \boldsymbol{M} \times \frac{\partial \boldsymbol{M}}{\partial x}$$

Where $u = \frac{JPg\mu_B}{2eM_s}$, J is the current density and the units of u are m s^{-1} while it is positive for $P > 0$.

2.3. Spin Hall Effect

The Spin Hall effect (SHE)[67–70] refers to the phenomenon where a spin accumulation on the lateral surfaces appears when charge current flows through a non-magnetic layer, usually heavy metal with strong spin-orbit coupling with examples like Pt[71–73], Ta[74], W[74,75]. This spin accumulation has opposite spin directions for opposing sides, thus a pure spin current is generated, transverse to the charge current, creating an orthogonal spin accumulation.

When a bilayer of a non-magnetic layer, i.e. underlayer, with a ferromagnet is considered and a current is injected in the system, the charge current flow from the underlayer can give rise to a spin current that can get absorbed by the adjacent ferromagnetic layer, therefore, exerts a torque on the magnetization in the adjacent layer. When considering such bilayer systems, another spin-orbit torque can arise from the Rashba effect[76–78]. However, the Rashba effect is expected to be relatively small compared to the SHE in the device systems studied, and its little contribution[79] is disregarded.

The maximum transverse spin current from the SHE, J_s, due to the charge current density is given by: $J_s = \theta_{SH} \cdot J$,where θ_{SH} represents the efficiency of the charge to spin conversion ratio and is called Spin Hall Angle, (SHA).

The SHE contribution to this bilayer system can be inserted in the LLG using a Slonczewski-like torque as:

$$\boldsymbol{\tau_{SH}} = -\gamma \boldsymbol{M} \times (\boldsymbol{M} \times H_{\mathrm{SH}}(z \times \boldsymbol{J}))$$

Where H_{SH} is:

$$H_{SH} = \frac{\hbar \theta_{SH} J}{2eM_s t}$$

and parametrizes the spin Hall effective field because of the SHE. J is the current density in the non-magnetic underlayer, and t is the thickness of the magnetic layer.

2.4. Dzyaloshinskii Moriya Interaction

The Dzyaloshinskii-Moriya interaction (DMI)[80,81] is an antisymmetric exchange coupling between neighboring spins and leads to chiral order in magnetic structures. It can be caused by broken inversion symmetry and spin-orbit interactions[82,83].

The Dzyaloshinskii-Moriya interaction has the Heisenberg form Hamiltonian and is defined as:

$$\mathcal{H} = \boldsymbol{D_{12}} \cdot (\boldsymbol{S_1} \times \boldsymbol{S_2})$$

With $\boldsymbol{D_{12}}$ describing the strength of the interaction. Compared to the Heisenberg exchange interaction, the Dzyaloshinskii-Moriya Interaction favors a canting of neighboring spins (moments).

DMI is found in several reports to stabilize Néel Domain Walls. Moreover, because it is innately chiral, it sets the chirality so that ↑↓ and ↓↑ DWs have conserved chirality, (clockwise or counterclockwise). When chirality is conserved, all DWs with their different configurations (↑↓ or ↓↑) move in the same direction, with current application, for acting spin orbit torques such as from SHE. This is of major significance for racetrack application, because opposing DWs move in the same direction and the domain sizes (representing the bits) are preserved. It is shown later (chapter 4) that a DMI contribution is found in these PMA Heusler films and is shown to be along the axis of the wire, stabilizing Néel DWs and has a strong dependence when examining the current induced chiral DW motion under externally applied in-plane fields.

3. Underlayer Chemical Templating Technique to promote the Heusler Growth

High quality films are grown with the methods described in chapter 1. The Mn_3Z (Z=Ge, Sn, Sb) sub-family of Heuslers, can be tetragonally distorted along one of the crystal axes, to minimize the unit cell crystal energy configuration. The tetragonal unit cell will be 45° rotated compared to the cubic configuration and will elongate along the *c* axis. An appropriate underlayer can promote the growth of tetragonal Mn_3Z which is the origin of their PMA[84,85]. In this chapter is discussed the role of a new Chemical Template Layering (CTL) technique as underlayers for the Heuslers, which results in great PMA for Mn_3Z as seen in Figure 3.10 and in chapter 4.

3.1. Properties

The Chemical Templating Layer is formed by elements which have the CsCl ordering structure. The CsCl crystal structure can be considered as two interpenetrating primitive cubic cells where the corner of one cell is at the body center position of the other. CsCl is in the cubic crystal system space group $Pm\bar{3}m$, usually referred to as B2 type shown in Figure 3.1.

The B2 type structure is schematically illustrated using Pearson's crystal database for the case of CoGa showing the unit cell and the ordering when viewing along the 100 and 110 orientations for a 2x2x2 cell presenting alternating layers of Co and Ga.

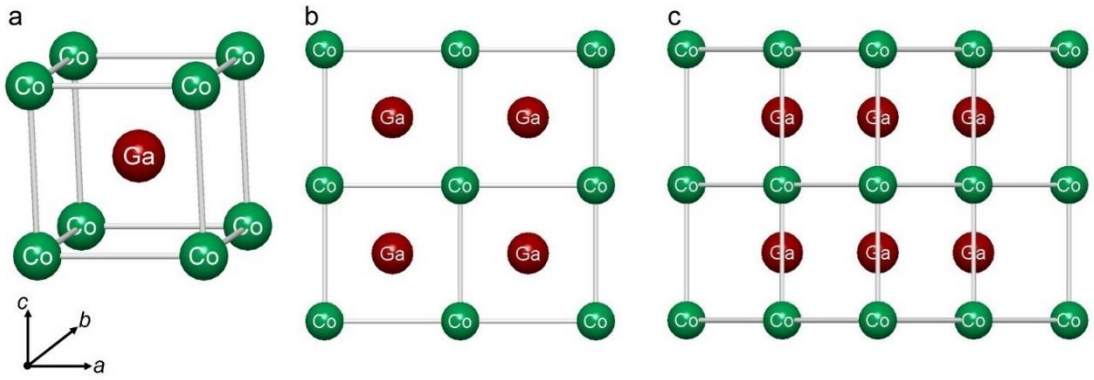

Figure 3.1 (a) CoGa unit cell for CsCl type structure (b) 2x2x2 cell when viewed from the 100 direction (c) 2x2x2 cell when viewed from the 110 direction

The Chemical Templating Layers X'Z' are formed from non-magnetic binary alloys, where the X' element is a transition metal (in this case Co) and Z' is a main group element (Al, Ga, Ge, or Sn) and they are not detrimental to the magnetic properties of the Mn_3Z. Furthermore, it is pivotal that the in-plane lattice constant closely matches that of the Mn_3Z. The CTL is chemically ordered with alternating layers. This CTL structure via chemical interaction promotes the growth of alternating atomic layers within the Heusler compound with distinct chemical composition even in the ultrathin regime and even for room temperature deposition. In so, when there are atomic steps in the surface of the CTL, the Mn_3Z Heusler will grow preferentially Mn-Z over X' terminated surface and Mn-Mn over Z' terminated surface and thus the Heusler will grow atomically ordered. In Figure 3.2 is shown the schematic illustration of the atomic templating concept viewed along the CoGa CTL [110] and Mn_3Z Heusler [100] axis.

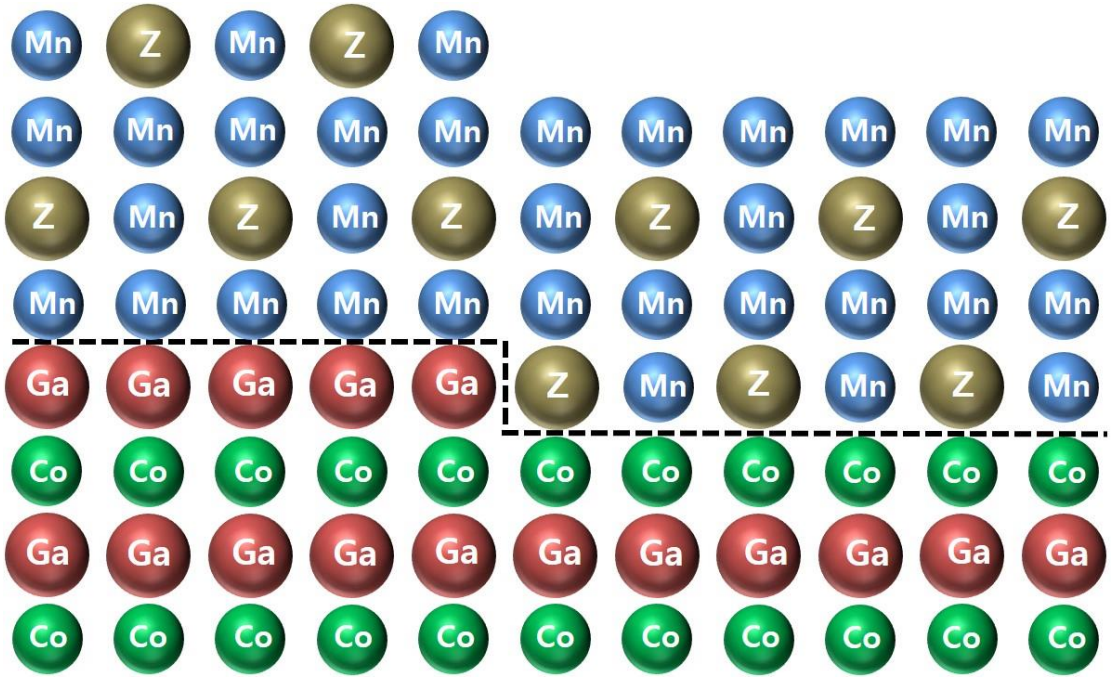

Figure 3.2 Schematic illustration of the Chemical Templating concept, as viewed from the [110] axis of CoGa CTL and [100] of Mn_3Z Heusler. The CTL grows in alternating layers of Co (X') and Ga (Z'). The dashed line marks the atomic step. MnMn grows preferentially over Ga (Z') terminated CTL surface, whereas, MnZ grows over Co (X') terminated CTL surface due to their preferential chemical bonding. The overgrown Mn_3Z Heusler is atomically ordered.

The overgrown Mn_3Z Heusler is tetragonally distorted and grows in the $D0_{22}$ structure, rotated by 45° compared to the CTL. The $D0_{22}$ structure is shown in Figure 3.3 for the Mn_3Z tetragonal unit cell with the corresponding atomic spin arrangement.

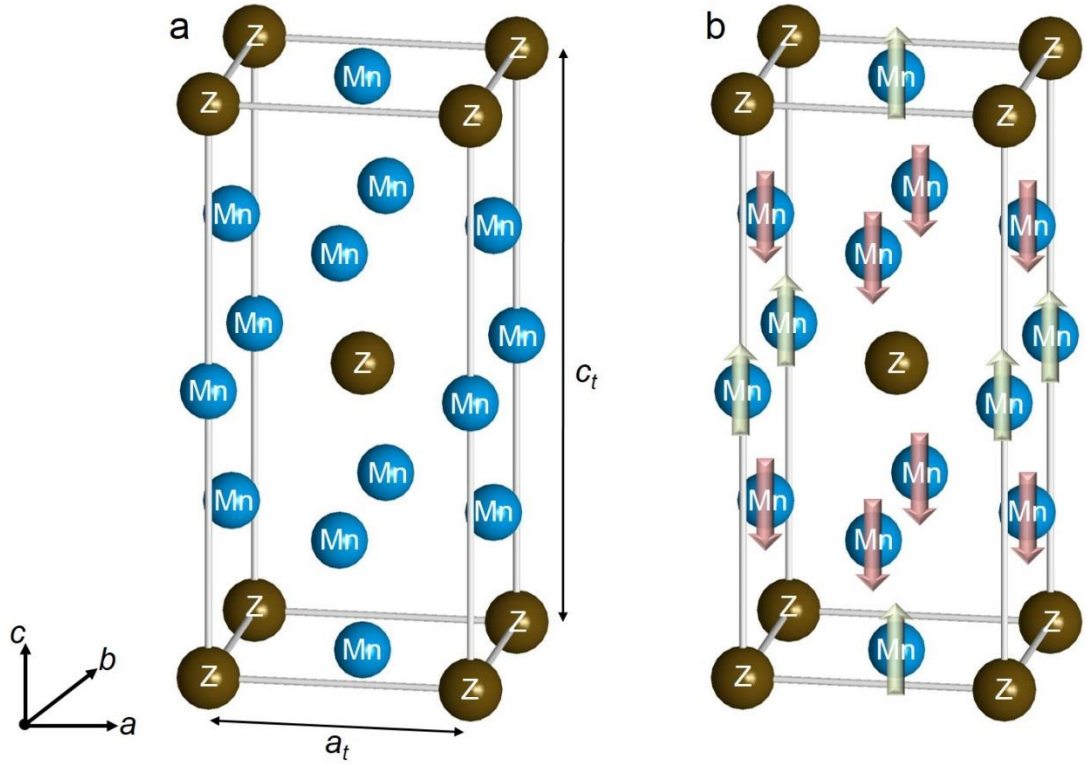

Figure 3.3 (a) $D0_{22}$ tetragonal unit cell of Mn_3Z and (b) denoting the ferrimagnetic moment alignment

The CTL is effective also for ternary Heusler alloys and demonstrates the universality of the CTL concept. In addition to CoAl, CoGa, CoGe, CoSn which are presented in the next section, many more candidate materials which could be used as CTLs are identified, but are not limited to those, and are presented in Table 3.1 as taken from Pearson's crystal data which have a comparatively small lattice mismatch with Mn_3Sn.

Type	X'Z'	Lattice constant (Å)	[%] Mismatch with: Mn_3Sn
Intermetallic	NiAl	2.89	4.0
Intermetallic	FeAl	2.91	4.5
Intermetallic	RhAl	2.97	6.4
Intermetallic	ReAl	2.88	3.5
Intermetallic	NiGa	2.88	3.5
Intermetallic	MnNi	2.97	6.4
Intermetallic	MnV	2.94	5.5
Intermetallic	FeTi	2.98	6.7
Intermetallic	CuZn	2.95	5.8
Intermetallic	BeTi	2.94	5.5
Silicide	CoSi	2.82	1.4
Silicide	OsSi	2.96	6.1
Silicide	RuSi	2.91	4.5
Fluoride	AgF	2.94	5.5

Table 3.1 CTL candidates with a B2 structure and a lattice constant between 2.8 and 3Å, (not including CoAl, CoGa, CoGe, CoSn).

In Table 3.2 are shown the calculated values for the tetragonal structure of the three Mn_3Z Heusler alloys which are the main focus of this study, Mn_3Ge, Mn_3Sn and Mn_3Sb, as taken from Faleev *et.al*[10,11].

	a_t (Å)	c_t (Å)	m (emu/cm^3)	Spin polarization
Mn_3Ge	3.73	7.08	188	Negative
Mn_3Sn	3.93	7.46	160	Negative
Mn_3Sb	3.82	7.79	163	Positive

Table 3.2 Theoretical calculated values for the Mn_3Z (Z=Ge, Sn, Sb) tetragonal structure using the parameters found in Faleev *et.al*[10,11].

The measured Heusler resistivities are: 265 μΩ · cm for Mn_3Ge, 239 μΩ · cm for Mn_3Sn and 212 μΩ · cm for Mn_3Sb, measured from nominally 500 Å thick calibration films

grown on Silicon substrates by sheet resistance measurement as introduced in section 1.2.1. Similarly, CoAl resistivity is 234 μΩ · cm and CoGa is 231 μΩ·cm.

3.2. CoAl – CoGa – CoGe – CoSn

At this point, four CTLs were identified and studied in addition to the candidates of Table 3.1. CoAl, CoGa, CoGe and CoSn are demonstrated to function as great Chemical Templating Layers proving excellent ordering for the overgrown Heusler. These layers are all grown at ambient temperature and then are subsequently annealed at T_{AN} to improve their ordering.

In Table 3.3 are shown the lattice constants for CoAl, CoGa, CoGe, CoSn in their B2 structure from Pearson's crystal database and the experimental values from their XRD data for a CsCl type structure which is further described in the next two sections. Note that CoGe is not documented in B2 structure in Pearson's database, and is found to form alternating layers of Co and Ge only for a certain T_{AN}.

CTL	Lattice constant (Å) Pearson's crystal data	Lattice constant (Å) Experimental	[%] Mismatch with:		
			Mn_3Ge	Mn_3Sn	Mn_3Sb
CoAl	2.86	2.84	7.3	2.3	5.0
CoGa	2.88	2.88	8.7	3.8	6.5
CoGe	--	2.71	2.8	-2.3	0.4
CoSn	2.93	2.98	11.7	6.9	9.5

Table 3.3 Chemical Templating Layers and their corresponding lattice mismatch from the experimental lattice constant

CoAl shows even improved properties as a CTL and the necessary atomic ordering occurs even at ambient temperature without the need for a subsequent anneal. Mn_3Sn has the closest lattice matching for CoAl, CoGa, CoSn but CoGe.

3.3. CTL Results – X-ray diffraction

As mentioned, CoAl, CoGa, CoGe, and CoSn are deposited at ambient temperature and subsequently annealed to achieve better ordering. A series of samples was grown for each case where no annealing and different T_{AN} were used for each sample. All films were 300 Å thick. XRD measurements were performed on CTLs and show the presence of both (001) and (002) peaks for selected T_{AN}. The existence of (001) superlattice peak, proves that there is alternating layering of the transition metal and the main group element (the constituent elements of the CTL).

For the CoAl CTL which is at this time identified as the best CTL candidate, the XRD measurement (diffractogram) of 300 Å CoAl CTL in Figure 3.4 displays the existence of CoAl (001) superlattice peak for all the 5 different samples without any annealing of the CoAl layer and with annealing at T_{AN}=200, 300, 400, 500 °C. The sample stacks were grown as: MgO (001) | 20 Å MgO | 300 Å CoAl -T_{AN}| 20 Å MgO | 30 Å Ta. All layers are grown at ambient temperature and for CoAl, it was first grown at ambient temperature and subsequently annealed at T_{AN} or not annealed at all.

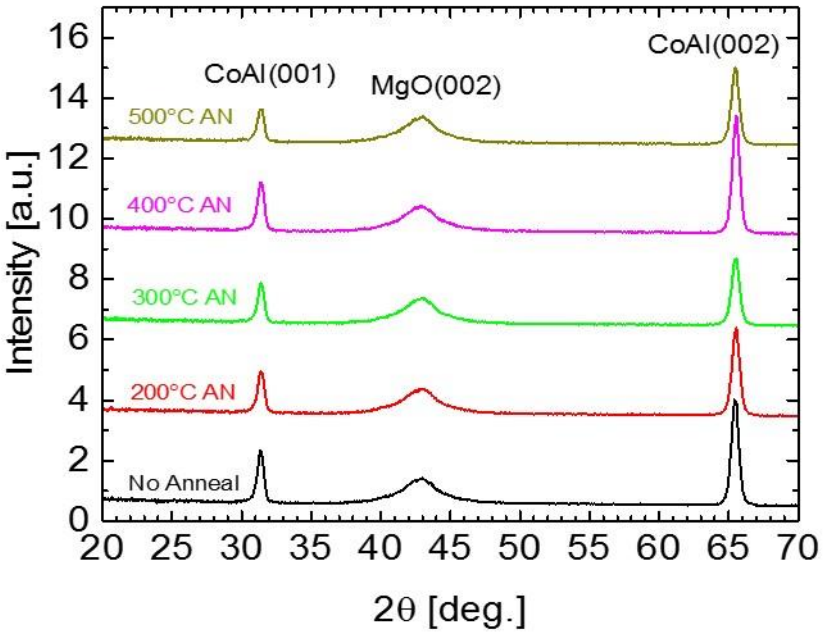

Figure 3.4 XRD diffractogram vs T_{AN} for CoAl CTL in the film stacks: MgO (001) | 20 Å MgO | 300 Å CoAl -T_{AN}| 20 Å MgO | 30 Å Ta.

Note that the low measured intensity of the MgO (002) peak was captured due to the step size limitation of the X-ray area detector. The step size was selected such that the CoAl (001) and (002) peaks fall close to the center of the areal detector used.

CoAl shows alternating layering of Co and Al even without any subsequent annealing and atomic ordering is obtained in the as-deposited state for the films which are grown at ambient temperature.

Similarly, the XRD diffractogram of 300 Å CoGa CTL is shown in Figure 3.5. The sample stacks are: MgO (001) | 20 Å MgO | 300 Å CoGa -T_{AN}| 20 Å MgO | 30 Å Ta. For CoGa, the T_{AN} is critical for the ordering within the layer. The sample without any subsequent annealing shows a very low intensity signal for (001) and (002) peaks. Nevertheless, the existence of the (001) superlattice peak show that there is alternating layering. The ordering improves with increasing T_{AN} as seen from the increased peak intensities.

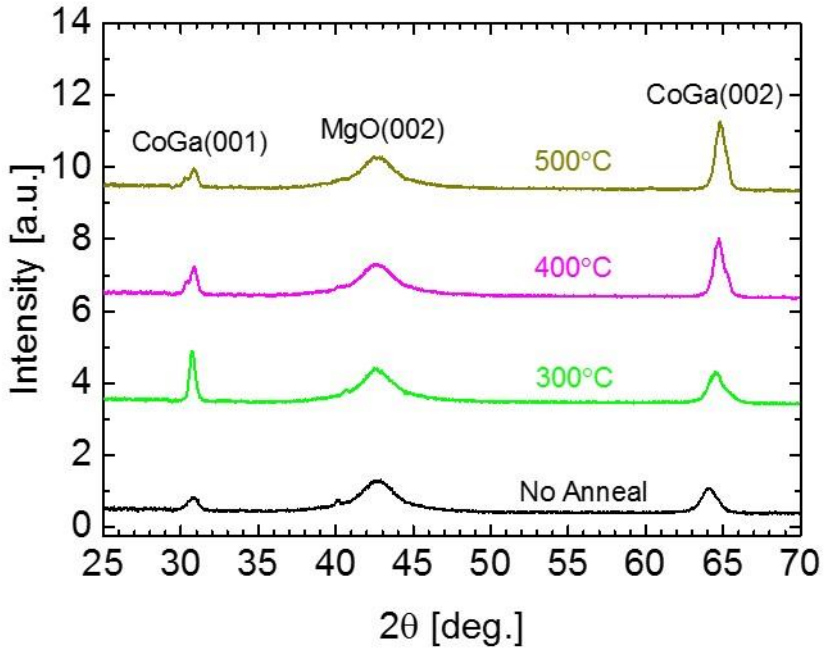

Figure 3.5 XRD diffractogram vs T_{AN} for CoGa CTL in the film stacks: MgO (001) | 20 Å MgO | 300 Å CoGa -T_{AN}| 20 Å MgO | 30 Å Ta.

Films with CoGe were also deposited 300 Å thick in the stacks: MgO (001) | 20 Å MgO | 400 Å Cr | 300 Å CoGe-T_{AN} | 20 Å MnGa | 20 Å MgO | 30 Å Ta. Similarly, in this case, MnGa was grown to confirm the ordering from XRD and P-MOKE as shown next. Figure 3.6 shows the XRD diffractograms of these films. For T_{AN} = 300 and 400 °C, the CoGe (001) peak does not appear, whereas for T_{AN} = 500 °C, the CoGe (001) superlattice peak is present, and the P-MOKE data in Figure 3.10 also confirms the successful PMA for the grown of the MnGa layer.

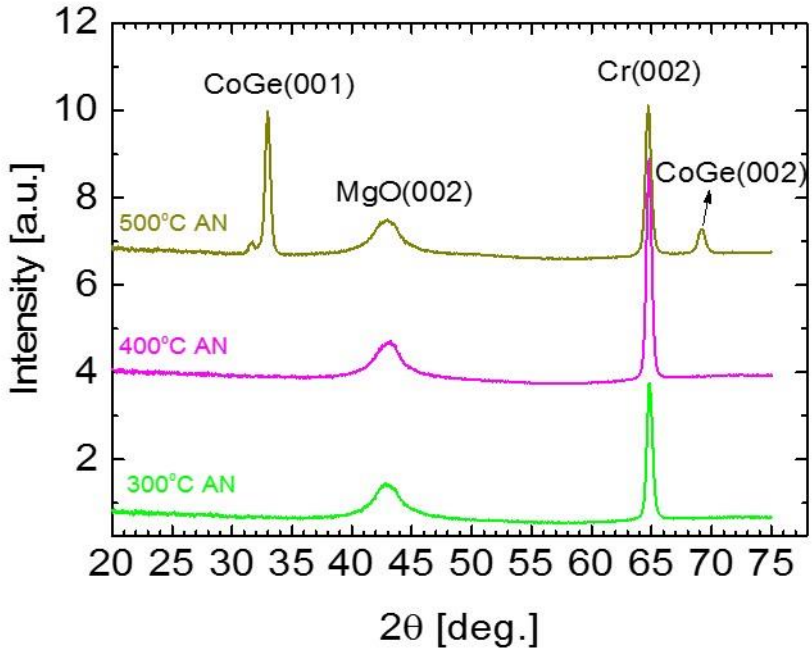

Figure 3.6 XRD diffractogram vs T_{AN} for CoGe CTL in the film stacks: MgO (001) | 20 Å MgO | 400 Å Cr | 300 Å CoGe-T_{AN} | 20 Å MnGa | 20 Å MgO | 30 Å Ta.

Lastly, the XRD diffractogram of 300 Å of CoSn CTL is shown in Figure 3.7. The samples were grown in the stacks: MgO (001) | 20 Å MgO | 400 Å Cr | 300 Å CoSn-T_{AN} | 20 Å MgO | 30 Å Ta. The (001) CoSn superlattice peaks show the alternating layering for no annealing and for T_{AN} = 200 and 300 °C. The samples annealed at higher T_{AN} = 400 and 500 °C, do not show the ordering as both the (001) and (002) CoSn peaks vanish. This is the case due to increased film roughness, CoSn becomes very rough at these annealing temperatures. Thus, the knowledge of the roughness of these CTLs is crucial for their application as layers promoting the growth of ultrathin Heuslers.

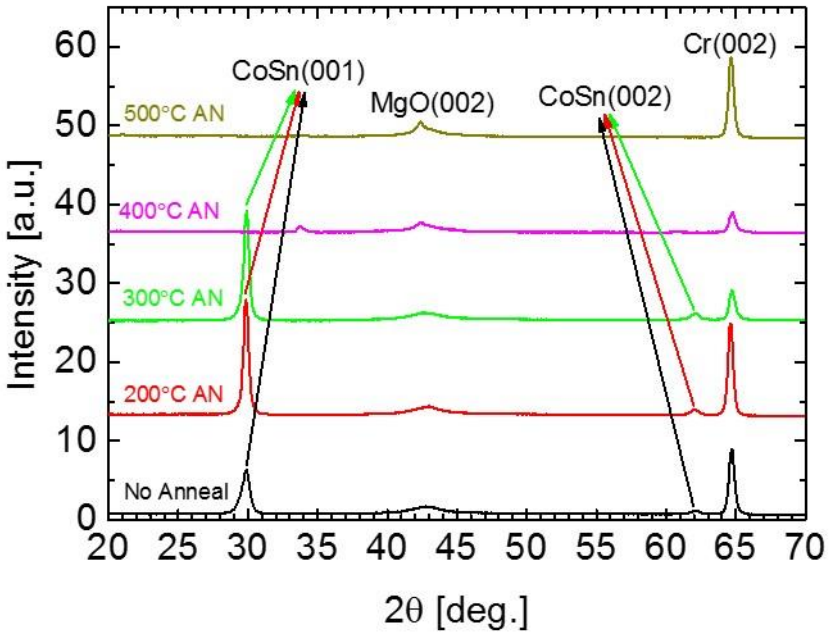

Figure 3.7 XRD diffractogram vs T_{AN} for CoSn CTL in the film stacks: MgO (001) | 20 Å MgO | 400 Å Cr | 300 Å CoSn-T_{AN} | 20 Å MgO | 30 Å Ta.

3.4. CTL Results – AFM and surface roughness with T_{AN}

The surface roughness of the grown CTL is affected by the composition and annealing temperature, impacting the templating role of the CTL and consequently the atomic ordering of the Heusler. For practical device application, the surface roughness must be the lowest possible especially when having multilayered structures.

Careful development of the CTL, requires a co-study of composition change with AFM surface roughness and XRD verification. In a similar way to the XRD film stacks presented in the previous section, the composition was varied with T_{AN}. In all cases AFM measurements on the CTLs were performed for 300 Å films which were first grown at ambient temperature and subsequently annealed at T_{AN}. The results are shown in Figure 3.8 and summarize the CTLs film roughness.

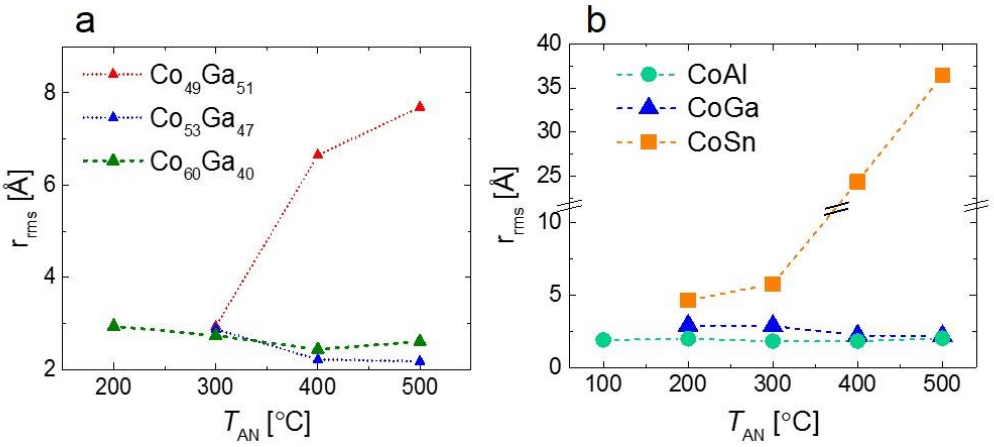

Figure 3.8 (a) Film roughness dependence on the composition of $Co_{1-x}Ga_x$ for different annealing temperatures. (b) Film roughness dependence on annealing temperature for different CTL layers: $Co_{51}Al_{49}$, $Co_{53}Ga_{47}$, $Co_{51}Sn_{49}$.

The AFM measurement results, demonstrate that the composition is critical to have smooth films. Additionally, in the case of CoSn, the disappearance of the XRD (001) and (002) CoSn peaks for T_{AN} = 400 and 500 °C is confirmed, since the film roughness increases dramatically for $T_{AN} \geq 400$ °C and the films are not smooth anymore.

From XRD and AFM measurements, the optimal composition and T_{AN} of the CTLs are determined. Atomically smooth films are chosen, with r_{rms} ~ 2 Å at the annealing temperature that provides enhanced ordering.

Therefore, the CTLs are optimized and for ease of reference, CoAl refers to $Co_{51}Al_{49}$ with T_{AN} = 400 °C, CoGa refers to $Co_{53}Ga_{47}$ with T_{AN} = 500 °C and CoSn refers to $Co_{51}Sn_{49}$ with T_{AN} = 300 °C, unless a bilayer is used and specified.

3.5. Transmission Electron Microscopy

The chemical templating concept and moreover the ordering within the Heusler layer is observed by means of cross sectional scanning Transmission Electron Microscopy (TEM). TEM images were taken for samples with CoAl, CoGa and CoSn CTLs with the Heusler grown over the CTL. Mn_3Ge, Mn_3Sn and Mn_3Sb are all imaged to confirm

their ordered growth and the images are presented in Figure 3.9. All images show epitaxy and ordering of both the chemical templating layers and the Mn_3Z Heuslers. Furthermore, the alternating layers of the CoAl, CoGa, and CoSn CTLs can be viewed. Similarly, the chemical ordering within the Heusler layers is evidently seen. The ordering can be clearly seen for Mn_3Sb, since the Sb atoms are much heavier (higher atomic number) compared to Mn and provide a better contrast. The ordering can also be observed in Mn_3Sn, and the contrast weakens in Mn_3Ge. The Mn-Sb and Mn-Sn layers are distinguishable from the Mn-Mn layers representing the altermatic atomic layers and the chemical ordering within the Heusler. Note that CoSn CTL here, refers to a bilayer of first grown $Co_{53}Ga_{47}$ annealed at 500 °C and then $Co_{51}Sn_{49}$ with T_{AN} = 400 °C. In this case, the bilayer remains atomically smooth with great ordering even when annealing at 400 °C.

Electron Energy Loss Spectroscopy (EELS) line scans performed on cross sectional TEM micrographs on CoGa CTL with Mn_3Sn Heusler film stack, display the relative concentration of various elements in the stack with atomic resolution. The EELS of the sample is pictured in Figure 3.9e and shows the alternating intensity signals for the CoGa CTL as a function of the film stack position. Where there is a maximum in the intensity signal for Co, it is a minimum for Ga and vice versa so that the intensities oscillate, thus indicating the alternating layers in the CoGa CTL used.

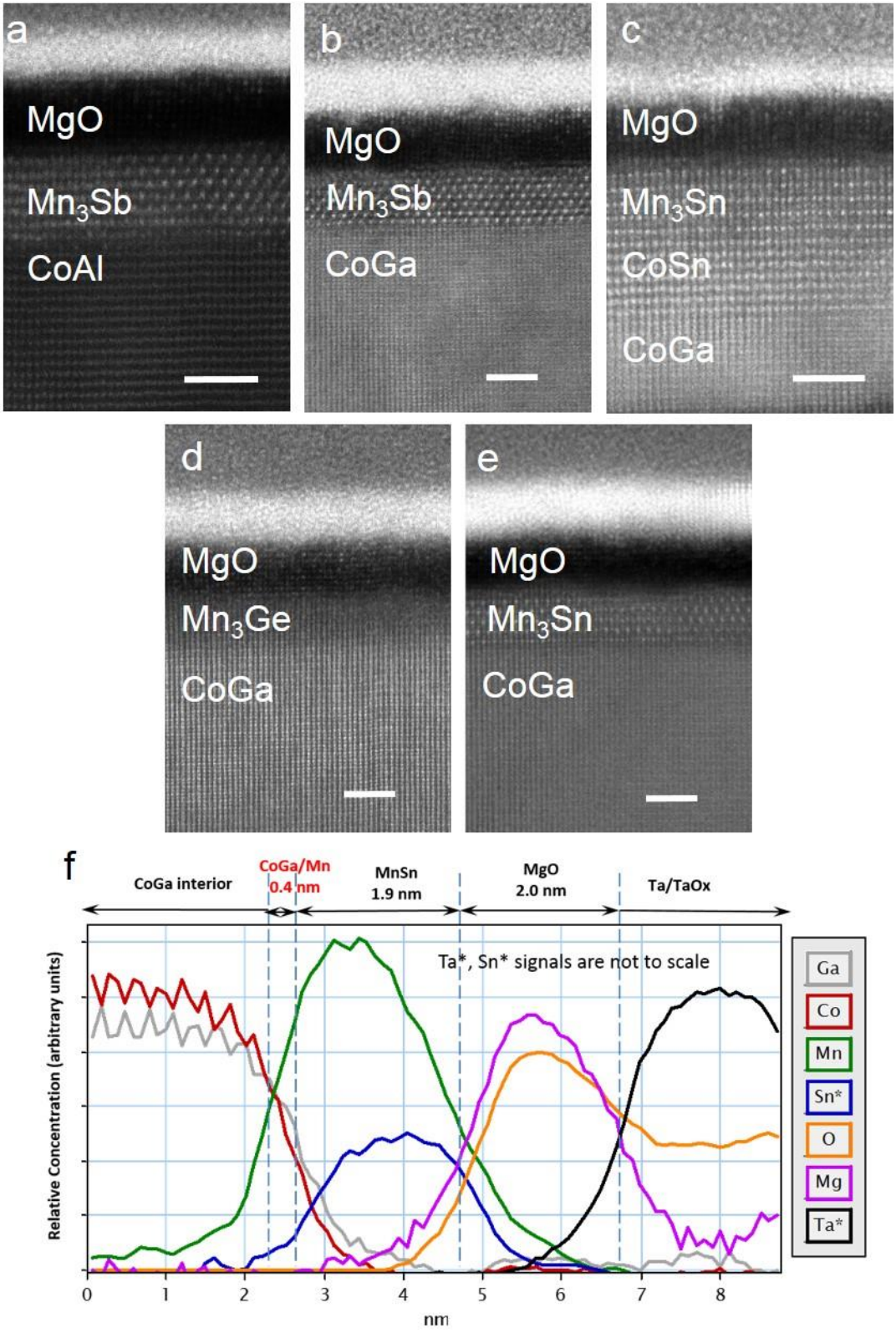

Figure 3.9 Cross sectional scanning TEM images performed on CoAl, CoGa, CoSn CTLs with 2 nm of Mn_3Z Heusler grown in the films stacks: (a) MgO (001) | 20 Å MgO | 300CoAl | 20 Å

Mn_3Sb | 20 Å MgO | 20 Å Ta. (b) MgO (001) | 20 Å MgO | 400 Å Cr | 300CoGa | 20 Å Mn_3Sb | 20 Å MgO | 20 Å Ta. (c) MgO (001) | 20 Å MgO | 30 Å CoGa | 20 Å CoSn | 20 Å Mn_3Sn | 20 Å MgO | 20 Å Ta. (d) MgO (001) | 20 Å MgO | 400 Å Cr | 300CoGa | 20 Å Mn_3Ge | 20 Å MgO | 20 Å Ta. (e) MgO (001) | 20 Å MgO | 400 Å Cr | 300CoGa | 20 Å Mn_3Sn | 20 Å MgO | 20 Å Ta. The scale bar lengths denote 2 nm. (f) EELS profile of the film stack from (e).

3.6. Results – P-MOKE of Heuslers grown on CTL and ordering with T_{AN}

The substantial improvement of the chemical ordering with T_{AN} can be seen from P-MOKE hysteresis loop measurements of the Heusler films grown onto the CTLs. As seen in Figure 3.10, the magnetic properties of the Heusler layers are strongly affected by the CTL's chemical ordering. The magnetic properties of the Heuslers grown on CTL show preferential growth of Mn-Z and Mn-Mn on X' and Z' CTL atoms, respectively.

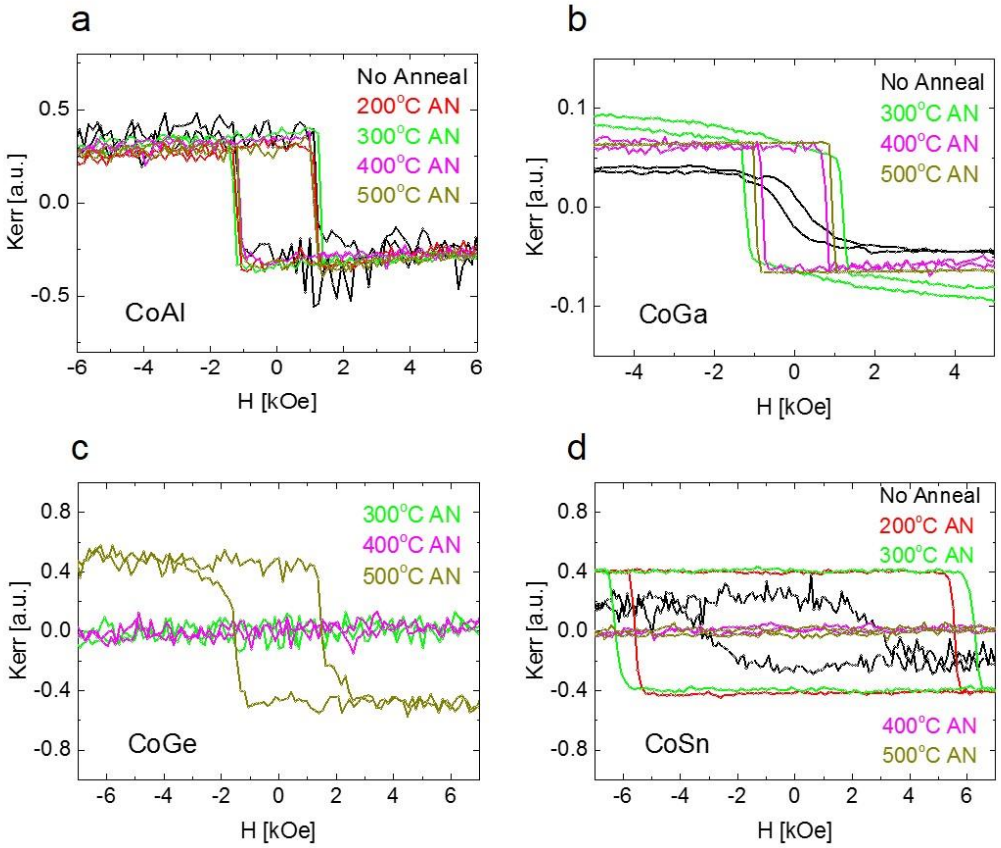

Figure 3.10 Heusler P-MOKE hysteresis loops for different CTLs used as a function of the CTL annealing temperature. (a) CoAl CTL with the film stack: MgO (001) | 20 Å MgO | 300 Å CoAl -T_{AN}| 20 Å MgO | 30 Å Ta. (b) CoGa CTL with the film stack: MgO (001) | 20 Å MgO | 300 Å CoGa -T_{AN}| 20 Å MgO | 30 Å Ta. (c) CoGe CTL with the film stack: MgO (001) | 20 Å MgO | 400 Å Cr | 300 Å CoGe-T_{AN} | 20 Å MnGa | 20 Å MgO | 30 Å Ta. (d) CoSn CTL with the film stack: MgO (001) | 20 Å MgO | 400 Å Cr | 300 Å CoSn-T_{AN} | 20 Å MgO | 30 Å Ta.

Excellent PMA with square hysteresis loops is found for all annealing temperatures of CoAl CTL and also without any annealing in the as-deposited state which is ordered. PMA was found for CoGa when it was annealed at 400 °C and above. For CoGe PMA was found for T_{AN} = 500 °C and for CoSn at T_{AN} = 200 and 300 °C.

Furthermore, to prove that the CTL and the chemical ordering is essential for the Heusler ordering, a series of samples are prepared and their P-MOKE response is measured, Figure 3.11. 15 Å Mn_3Sn is grown in three cases: 1. Using a CoGa CTL to promote the Heusler growth, 2. Using Cr as the underlayer for the Heusler growth and, 3. Inserting a non-magnetic thin layer of Sb in between the CTL and the Heusler. The

chemical templating, CTL (in this case CoGa) promotes growth whereas Cr layer and an Sb insertion layer cannot give rise to PMA for the similarly grown 15 Å Mn_3Sn Heusler layer.

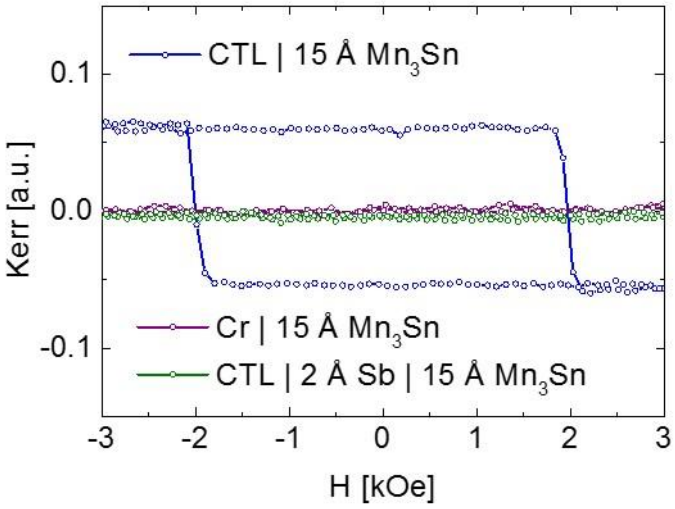

Figure 3.11 P-MOKE hysteresis loops for 15 Å Mn_3Sn when using CTL underlayer, Cr underlayer and CTL underlayer with Sb insertion layer. The film stack for the CTL is: MgO (001) | 20 Å MgO | 300 Å CoGa CTL | 15 Å Mn_3Sn | 20 Å MgO |20 Å Ta. For the Cr underlayer the film stack is: MgO (001) | 20 Å MgO | 400 Å Cr | 15 Å Mn_3Sn | 20 Å MgO |20 Å Ta. For the Sb insertion layer, the film stack is: MgO (001) | 20 Å MgO | 300 Å CoGa CTL | 2 Å Sb | 15 Å Mn_3Sn | 20 Å MgO |20 Å Ta.

When the CTL is used, excellent PMA is found for the Heusler. Whereas, no loop is observed when Cr is used, because Cr cannot promote chemical ordering for the overgrown Heusler. Additionally, no magnetization is observed when 2 Å of non-magnetic Sb layer is inserted between the CTL and the Heusler, because Sb obstructs the chemical templating for the Heusler.

3.6.1.Ambient Temperature and Room Temperature growth

In this study, the growth of the layers was performed at ambient temperature. Whenever there was an annealing step, before proceeding to the next layer growth, there was first a waiting time until the temperature of the carrier holding the substrate would be below 100 °C. After that wait time, the next layer sequence would initiate and so on. In practice, after the wait time, the deposition system sets to prepare and complete all the necessary steps for the next layer, such as moving the substrate carrier to the desired target position, set the gas environment, ignite the plasma and strike the target, complete a pre-sputtering routine of the target before starting to grow the film. That time can vary from 7-20 minutes in which, the carrier temperature drops even more down to ~75 °C. For contiguity, in Figure 3.12, is shown a comparison of P-MOKE for a 20 Å Mn_3Ge film which was grown at 100 °C and a similar film where the 20 Å Mn_3Ge was grown at 30 °C. The magnetic properties are very similar and hence in the current study, ambient deposition temperature refers to samples deposited in the temperature range between 30 °C and 100 °C.

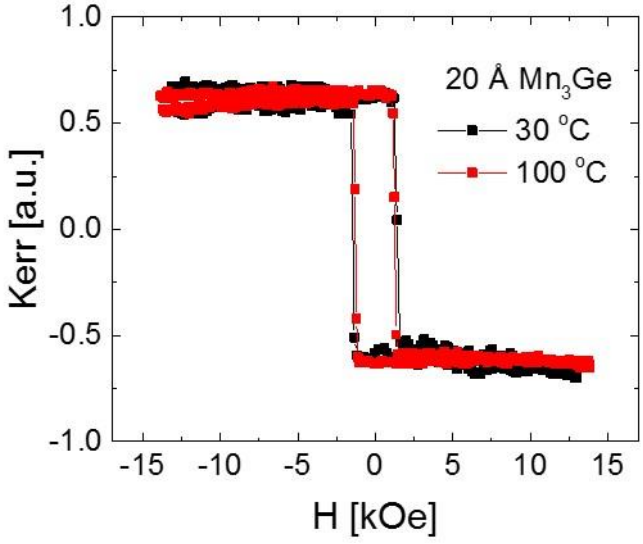

Figure 3.12 P-MOKE of 20 Å Mn_3Ge grown at 100 °C and at 30 °C. The film stacks are both MgO (001) | 20 Å MgO | 50 Å CoGa | 20 Å Mn_3Ge | 20 Å MgO |20 Å Ta with the Mn_3Ge layer grown at different carrier temperatures.

3.7. CTL – Heusler growth on Silicon substrate and P-MOKE, S-VSM

The CTL concept allows for excellent growth of ultrathin Mn_3Z Heuslers with great PMA. The study is mainly focused on growth over single crystalline MgO (001) substrates. CoAl is a great CTL candidate material and can enable great PMA for the overgrown Heusler when used on Silicon substrates. Figure 3.13 shows the P-MOKE hysteresis loop for 20 Å Mn_3Sb grown on CoAl CTL using a Silicon substrate with an amorphous thermally grown SiO_2. Additionally, Squid-Vibrating Sample Magnetometry (S-VSM) is performed to show the out-of-plane magnetization. A reference sample without the Mn_3Sb Heusler layer was also grown and measured for comparison.

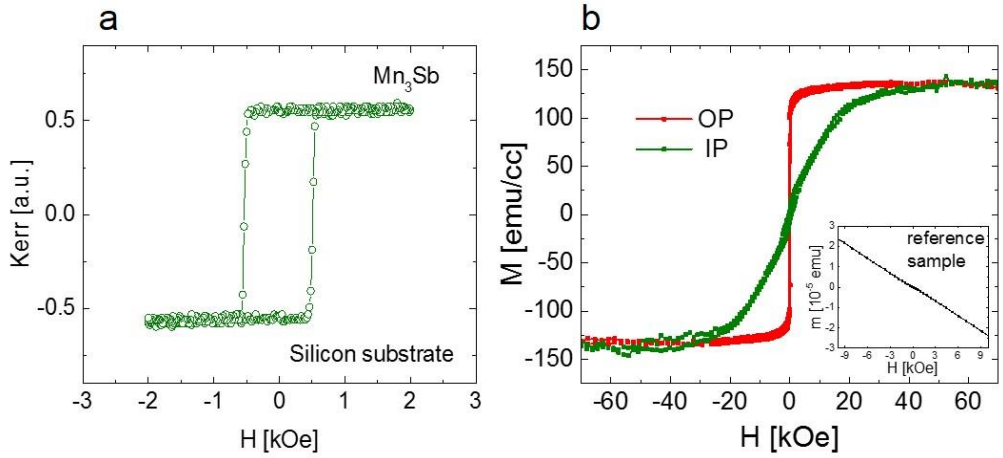

Figure 3.13 P-MOKE and out-of-plane (OP), in-plane (IP) S-VSM for 20 Å Mn_3Sb on Silicon substrate. In the inset is a control sample grown with the exact same structure without the Heusler layer The Heusler film stack is: Si (001) | 250 Å SiO_2 | 50 Å Ta| 3 Å CoFeB | 30 Å MgO | 50 Å CoAl | 20 Å Mn_3Sb | 20 Å MgO |20 Å Ta. The reference sample stack is: Si (001) | 250 Å SiO_2 | 50 Å Ta| 3 Å CoFeB | 30 Å MgO | 50 Å CoAl | 20 Å MgO |20 Å Ta and does not show any moment.

The Mn_3Sb magnetic hysteresis loops shows great PMA with magnetization ~ 145 emu/cm^3. The reference sample does not show any loop. The deviation from the predicted value of 163 emu/cm^3 can be due to a small magnetic dead layer which is

estimated to be within a fraction of a unit cell, since great PMA is observed even for 7.5 Å (unit cell thick) Mn_3Sn and 10 Å Mn_3Sb. Note that the MgO substrates have a significant moment themselves from contaminants within the substrates which is comparable to the ferrimagnetic moment of the Mn_3Z Heuslers when performing magnetometry on Heuslers grown on MgO substrates.

3.8. Conclusions

A new technique utilizing Chemical Templating Layers is developed and demonstrated. Ultrathin Mn_3Z, (Z=Ge, Sn, Sb) Heuslers can be grown atomically ordered and exhibit great magnetic properties, having PMA with square P-MOKE hysteresis loops.

The concept is that a non-magnetic binary alloy X'Z' where X' is a transition metal and Z' is a main group element, grows ordered in the B2 structure. This layer provides the chemical ordering for the overgrown Heusler which grows tetragonally distorted. The key parameters for this Chemical Templating Layer is 1. to have its in-plane lattice constant, closely matching that of the Heusler. 2. Consist of elements that are not detrimental to the magnetic properties of the Heusler. And 3. to be chemically ordered with alternating layers of X' and Z', so that even when an atomic step occurs in the surface of the CTL, then a Mn-Z layer will grow preferentially over the X' terminated surface and a Mn-Mn layer will grow over a Z' terminated surface due to their preferential chemical bonding. In such way, the Heusler will be atomically ordered of alternating layers of Mn-Mn and Mn-Z.

A list of candidate CTL materials are presented and four of them are studied. CoAl, CoGa, CoGe and CoSn can promote chemical ordering. CoAl grows chemically ordered at room temperature without any subsequent annealing. CoGa, CoGe and CoSn improve their ordering with an additional in-situ annealing step. The CTL is so effective that even single unit cell thick Heusler exhibits great PMA (see Figure 4.2). Moreover, the successful growth of PMA ultrathin Heusler is demonstrated, using CTL on amorphous Silicon substrate with thermally grown SiO_2.

4. Ultrathin Heusler DW motion under Kerr microscopy

Mn_3Ge, Mn_3Sn and Mn_3Sb films are grown epitaxially, chemically ordered over a CTL with the detailed methods discussed. The high quality of the films is verified with AFM, XRD and their magnetic properties with P-MOKE. Applying the developed fabrication techniques described, nanowires are patterned from deposited blanket films. In the current racetrack literature, the term nanowire is used to suggest the thickness of the wires is in nm regime. Hence the conventional nomenclature is used, with the racetrack thicknesses being less than 2 nm.

All the films consist of MgO (001) substrate which is annealed at 650 °C for 30 minutes and then cooled down to room temperature (below ~100 °C). All layers are deposited at room temperature and in the case of the CTL, subsequently annealed, resulting in smooth CTLs, with r_{rms}<2 Å. It is followed by a cool-down waiting time to room temperature for the growth of the next layer – the ultrathin Mn_3Z (Z=Ge, Sn, Sb) Heusler. Then the Mn_3Z Heusler layer. The capping layers are 20Å MgO and 20Å Ta.

The thickness of the underlayer chosen is 50 – 100 Å. This range is the optimal found for great PMA for the Heusler grown over the CTL and having resistance closely matching the one of the Heusler. All different CTLs are considered equivalent to choose from, in terms of Heusler overgrowth, seen from their PMA, and CoGa was used for most of the DW motion study.

4.1. Main results and Mn_3Z DW motion

Nanowires were fabricated from these blanket films, using the patterning procedure discussed in section 1.4. Each fabricated sample contains an array of nanowires with

different orientations on the MgO substrate and with varying wire dimensions. An optical microscopy image shows the wire positioned between the two wider areas which serve as contact pads (Figure 4.7). Wire bonds to the device contact pads are made using an Aluminum wire bonder. Prior to that, the device to be measured was examined under an optical microscope for any visual defects from the fabrication process and if any, another equivalent device was chosen. The device was brought under the Kerr microscope to study DW motion and then was electrically connected to the experimental setup.

4.1.1. Single DW creation to allow for DW motion experiments

To create a DW within the wire, the method developed and used throughout the study requires to determine three parameters: 1. domain nucleation voltage, 2. propagation field and 3. the lowest voltage required for DW motion. Note that, for creating DWs, the applied generator voltage is referred instead of the induced current density. Initially, an external out of plane field was applied to saturate all the moments at an Up (↑) or Down (↓) magnetic state through the entire device. This out of plane field is much higher that the coercive field of the blanket film and it was also verified that it can switch the whole device by viewing the Kerr contrast change in the entire device when switching between the two states. The voltage at which domain nucleation takes place is determined (and equivalently determines the limit of the current density to be applied for DW motion). As the pads are much wider than the wire, the highest current density is carried in the wire and thus domain reversal can take place[86–90].

For the DW injection, two voltage generators were used (see section 1.3.2). The first one with a +50V, -45V limit and the second one, only positive pulse generator with a limit of 100V. Depending on the device resistance (which is determined by selected wire length and width), if +50V is not sufficient to create nucleation of opposite domains, the +100V limit generator was instead used to nucleate an opposite domain and then changed back to the picosecond pulse generator to perform the measurements.

A small out of plane field, in the opposite direction of the saturated moment of the device, assists to the domain nucleation.

Next, the out of plane propagation field was determined by increasing slowly the external out of plane field until the nucleated domain (or domains) started expanding. Under the propagation field, which is applied in the direction of the nucleated domains, the nucleated domains expand within the wire until they consolidate to a single domain. This single domain is within the wire and is of opposite direction to the starting magnetization.

At this point, the device pads are of opposite magnetization to the wire and two DWs separate these regions. To study the DW motion, a single DW is shifted in the wire. To do so, the nucleated domain within the wire is preferentially expanded towards one side of the device until it completely takes over the device pad. What remains, is a device with two opposing magnetization domains, separated by the DW located in the wire.

Explaining the last step, current pulses are used to move the two DWs, and thus the domain towards one end of the wire with the wire pad since the two DWs move in the same direction depending on the polarity of the applied pulse. The lowest applied voltage that can initiate DW motion is determined by observing the start of the motion of the entire domain. Controlling the applied field, the expansion of the nucleated domain is favored, and expands in both directions. At the same time, applied current pulses can keep one side of the domain within the wire, while the other side keeps expanding to the wire pad due to the applied field. Therefore, of the two DWs initially in the wire, separating the nucleated domain, one DW is maintained within the wire with current pulses, while the other DW moves under the applied field which expands the nucleated domain to one side of the device.

The outcome is having a single DW placed within the wire, separating the two sides of the device which have opposite magnetization direction.

4.1.2. Mn_3Z DW velocity dependence on the applied current density

Having a single DW within the wire, the DW motion is studied throughout the whole length of the wire applying current pulses. The current pulses are 100 ns long. The DW is moved in a lock step mode with the pulse or pulses applied. DW travelling distance of at least 2-5 μm is used in every DW step motion to clearly distinguish the motion. Depending on the current density, especially when it is low, a pulse train is necessary to get the DW to move for such distance. The pulse train consists of multiple 100 nanosecond long current pulses, each one followed by a DW relaxation time of 10 milliseconds. The 10 milliseconds relaxation time does not account for the DW motion as no current is applied during that time. The DW velocity is then determined for this pulse or pulse train by dividing the distance travelled by the DW to the integrated current pulse duration (number of pulses in the pulse train -n), $n \cdot 100$ ns. Several current pulse trains are applied to cover almost the full extent of the wire. The final DW velocity is determined as the averaged velocity from the distance travelled by the integrated pulse trains. Positive and negative pulses are used to move the DW in opposite directions. During the DW motion experiments, caution was given to not move the DW at the boundary with the wire pad as then the current density would be different from the estimated value and would cause a systematic error in the DW velocity measurements.

Mn_3Ge, Mn_3Sn and Mn_3Sb with thicknesses of one, two unit cells, or little thicker, are prepared with CoGa CTLs. The current induced DW motion for the Mn_3Z, is presented in Figure 4.1 for Mn_3Ge, in Figure 4.2 for Mn_3Sn, and in Figure 4.3 for Mn_3Sb. Alongside, their P-MOKE hysteresis loops show square loops for all the films. Increasing the thickness of the Heusler increases the coercive field of the film. The figures include the different Heusler thicknesses -t used. The film stacks are: MgO (001) | 20 Å MgO | 50 Å CoGa | t-Mn_3Z | 20 Å MgO | 20 Å Ta.

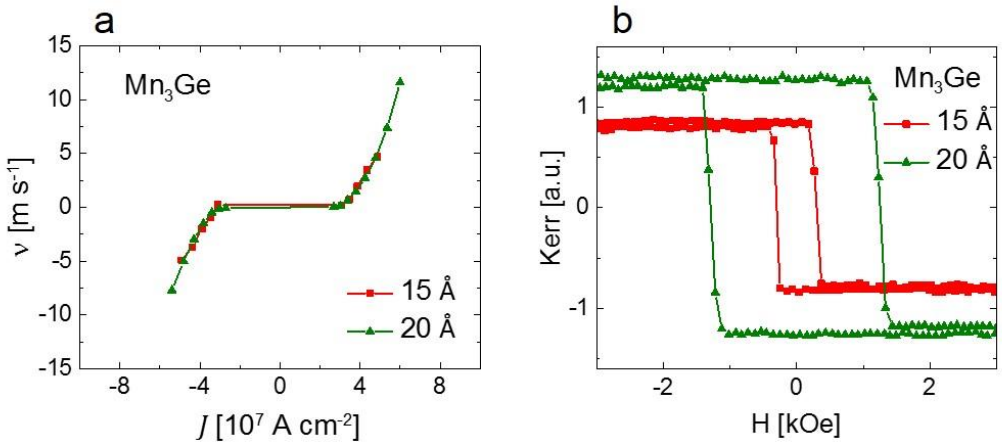

Figure 4.1 (a) 15 and 20 Å thick Mn_3Ge DW velocity versus current density *J*. (b) Corresponding P-MOKE signals. The films stacks are: MgO (001) | 20 Å MgO | 50 Å CoGa | 15 or 20 Å Mn_3Ge | 20 Å MgO | 20 Å Ta.

The top DW velocity for Mn_3Ge is 11.5 ms^{-1} and the direction of motion is along the current flow. Note that the pulse generator has higher positive pulse limit of 50V compared to -45V for negative pulses, and thus the measured velocity was higher for the higher positive current density. Nevertheless, it was confirmed with the higher voltage pulse generator that 50V was around the highest applicable voltage before DW nucleation takes place. The critical current density to initiate the DW motion is $J_c = 2.8 \cdot 10^7 A\,cm^{-2}$.

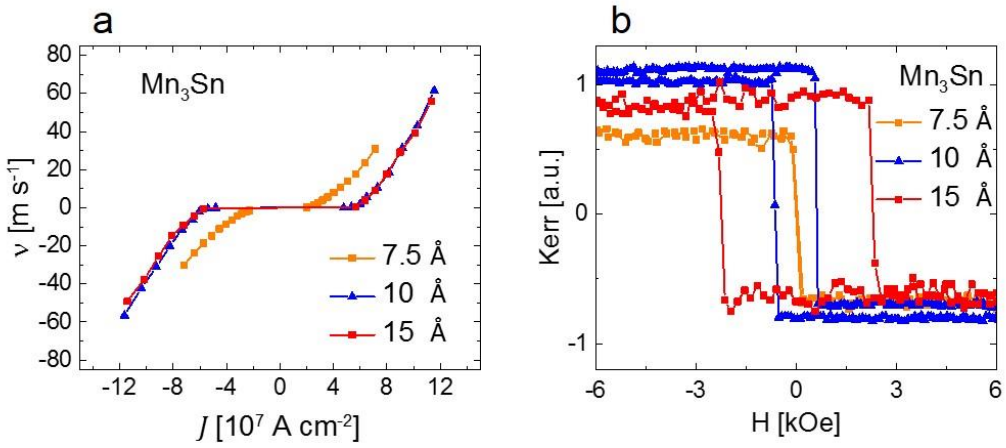

Figure 4.2 (a) 7.5, 10 and 15 Å thick Mn_3Sn DW velocity versus current density *J*. (b) Corresponding P-MOKE signals. The films stacks are: MgO (001) | 20 Å MgO | 50 Å CoGa | 7.5 or 10 or 15 Å Mn_3Sn | 20 Å MgO | 20 Å Ta.

The highest DW velocity for Mn_3Sn is 61 ms^{-1} also with the direction of motion to be along the current flow. Critical current density for the unit cell 7.5 Å thick Mn_3Sn is $J_c = 2 \cdot 10^7 A\,cm^{-2}$ and for the 10-15 Å thick is $J_c = 4.9 \cdot 10^7 A\,cm^{-2}$.

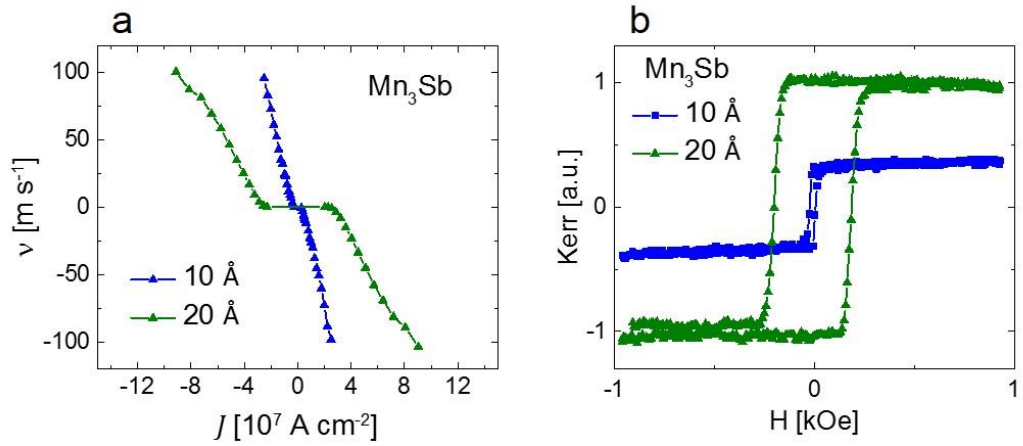

Figure 4.3 (a) 10 and 20 Å thick Mn_3Sb DW velocity versus current density *J*. (b) Corresponding P-MOKE signals. The films stacks are: MgO (001) | 20 Å MgO | 50 Å CoGa | 10 or 20 Å Mn_3Sb | 20 Å MgO | 20 Å Ta.

The topmost DW velocity for Mn_3Sb is -103 ms^{-1} and the direction of motion is along the electron flow (it is shown in the next section for $Mn_{3.1}Sb$ that the DW speed can reach -129 ms^{-1}). Critical current density for the 20 Å thick Mn_3Sb is $J_c = 2.3 \cdot 10^7 A\,cm^{-2}$ and a low critical current density of $J_c = 2.8 \cdot 10^6 A\,cm^{-2}$, is found for 10 Å Mn_3Sb.

The data for Mn_3Z, Z=Ge, Sn, Sb, shows the motion for both positive and negative current pulses. Positive and negative pulses move the DW in opposite direction but at a similar velocity, for the same current density. Furthermore, the direction of motion does not depend on the Up-Down (↑↓) or Down-Up (↓↑) domain wall configuration seen in the experiments. The main important finding is that the direction of motion is determined by the bulk spin polarization, *P*, of the Mn_3Z which is negative for Mn_3Ge and Mn_3Sn but positive for Mn_3Sb, as seen in Table 3.2. Thus, the main driving mechanism for the DW motion is the volume spin transfer torque[88,91,92]. Lastly, the critical current density J_c to initiate DW motion is much smaller for single unit-cell thick Heusler films due to lower intrinsic pinning, seen in Mn_3Sn and Mn_3Sb. The J_c increases but varies little for the thicker films studied.

4.2. DW motion for CoSn, CoAl, CoGa CTL layers in Mn_xSb (x=2.0, 2.7, 3.1)

As demonstrated in chapter 3, CoAl, CoGa and CoSn are all exemplary candidates for Chemical Templating Layers and the DW motion of Heuslers grown on CoAl and CoSn is also investigated. The overgrown Heuslers show excellent PMA from P-MOKE hysteresis loops. Furthermore, using the methods described for co-sputtering deposition, the composition of the Heusler grown is modified, by controlling the power output set to the elemental targets Mn, Mn and Sb, and verified by RBS measurements. Thus, demonstrating the universality of the CTL concept, even when changing the composition of the Heusler away from the Mn_3Z. Figure 4.4 shows the DW velocity dependence on the current density applied for different CoAl, CoGa, CoSn CTLs with Mn_xSb Heusler magnetic material, where x=2.7, 3.1, 2.0 respectively. The details of the stacks are given in the figure caption.

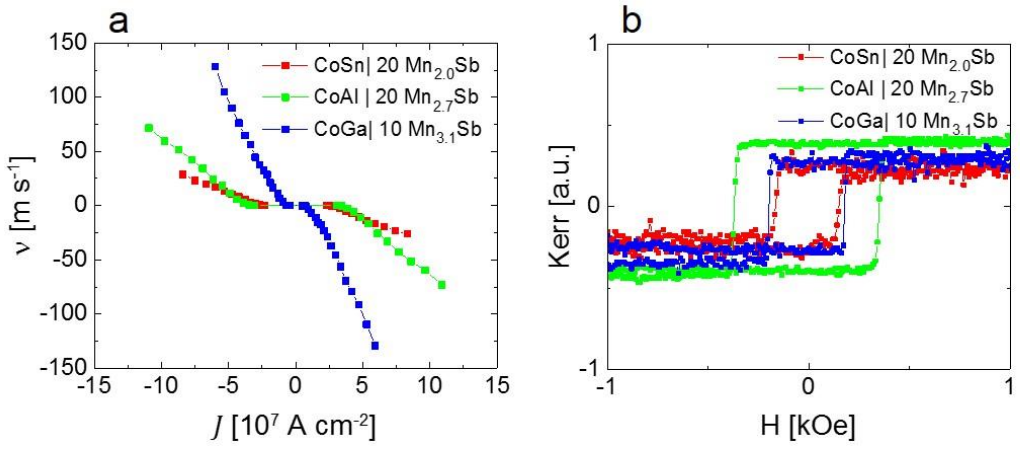

Figure 4.4 (a) Mn_xSb Heusler (x=2.7, 2.0, 3.1) DW velocity versus current density *J* for CoAl, CoSn and CoGa CTL respectively. (b) Their corresponding P-MOKE measurements. The film stacks are: MgO (001) | 20 Å MgO | 30 Å CoGa | 20 Å CoSn | 20 Å $Mn_{2.0}Sb$ | 20 Å MgO | 20 Å Ta shown in red. MgO (001) | 20 Å MgO | 50 Å CoAl | 20 Å $Mn_{2.7}Sb$ | 20 Å MgO | 20 Å Ta shown in green. MgO (001) | 20 Å MgO | 50 Å CoGa | 10 Å $Mn_{3.1}Sb$ | 20 Å MgO | 20 Å Ta shown in blue.

The variances in highest DW velocity can be attributed to the change in the total magnetization of the different composition of the Mn_xSb Heusler as more (or less) Sb atoms replace Mn atoms (see Figure 3.3b). Intrinsic pinning can account for the varying critical current densities, with the smallest one being for the thin 10 Å $Mn_{3.1}Sb$. Notably, the highest achieved DW velocity in this study of Heusler DW motion is achieved at -129 ms^{-1} for $Mn_{3.1}Sb$ with a critical current density of $J_c = 5.0 \cdot 10^6 A\,cm^{-2}$. The CTL concept is further verified by the successful DW motion in these different Heusler composition layers, grown onto three different CTLs. Furthermore, the Heusler magnetic materials also show high tunability in composition and properties, which will be the subject of chapter 5.

4.3. DW motion dependence on nanowire width

Wires of different dimensions (widths and lengths) are studied. The DW motion was found independent of the width of the nanowire for the widths: 2, 5, 10 and 20 μm. In Figure 4.5, the DW velocity versus *J* is shown for the stack: MgO (001) | 20 Å MgO | 50 Å CoGa | 7.5 Å Mn_3Sn | 20 Å MgO | 20 Å Ta for different wire widths. As mentioned, the voltage limits of the power supply are +50V and -45V, so that the width of the nanowire limits the maximum current density that can be applied. Therefore, the current density is constricted by the width of the wire selected. And the higher current densities can only be achieved with the 2 μm wire widths. This justifies the selection of the 2 μm wire width to be the center of this study as in this case the maximum DW velocity could be achieved. The duration of the pulses used is 100 ns.

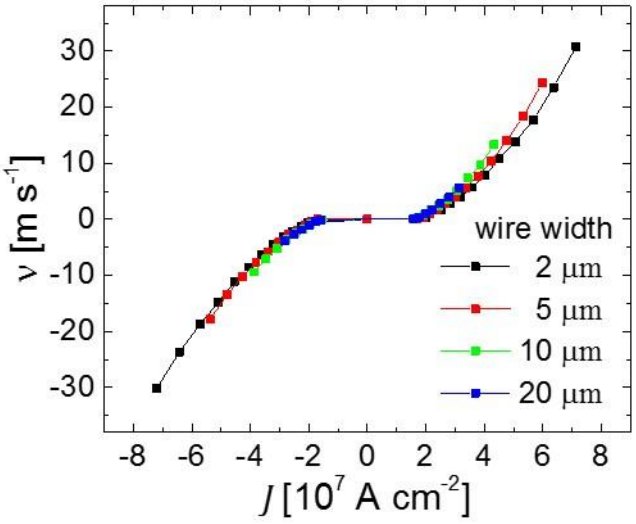

Figure 4.5 DW velocity vs applied current density J, for different wire widths of 2, 5, 10, 20 μm in the case of 7.5 Å Mn_3Sn grown over 50 Å CoGa CTL Film stack : MgO (001) | 20 Å MgO | 50 Å CoGa | 7.5 Å Mn_3Sn | 20 Å MgO | 20 Å Ta.

In all the Heuslers and underlayers used in this study, no DW tilt[93] is found to be associated with the DW motion, when applying current in both directions and for both DW configurations, observed from the experiments.

4.4. Current pulse length dependence for different Heusler film thicknesses

The DW velocity dependence on the Heusler film thickness for various current pulse lengths was explored. In addition, the critical current density for DW motion, J_c, is compared for current pulse lengths varying from 5 ns for Mn_3Sn and 20 ns for Mn_3Ge up to 100 ns for all the thicknesses studied. Figure 4.6 shows the DW motion results for different Heusler thicknesses and current pulse lengths. The decreasing wire resistivity with Heusler layer thickness and DW dynamics[94–96] can account for this dependence. For thicker films, the DW motion becomes insensitive to the pulse length.

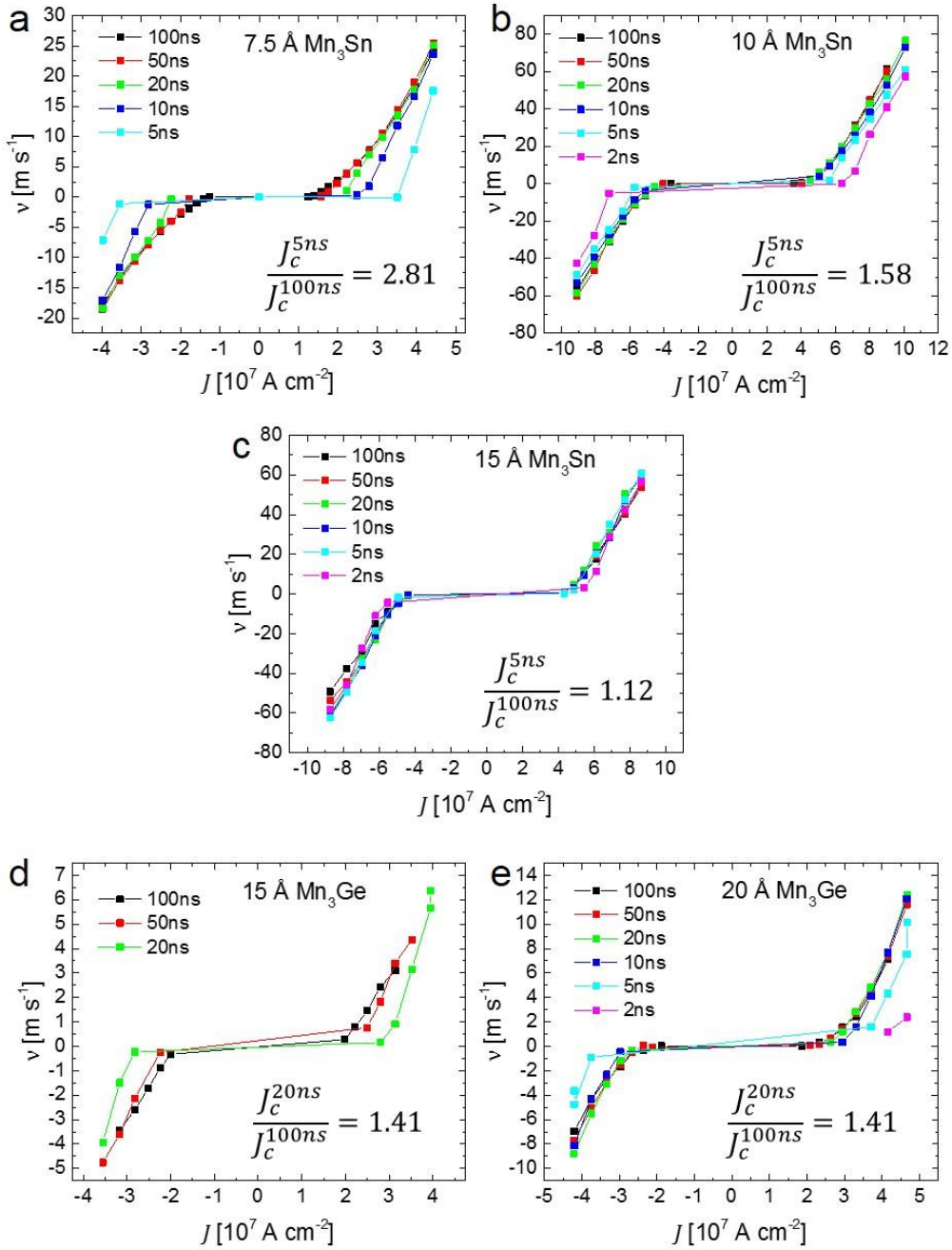

Figure 4.6 (a) – (c) Pulse length dependence of the DW velocity for Mn_3Sn. The film stacks are: MgO (001) | 20 Å MgO | 50 Å CoGa | 7.5 or 10 or 15 Å Mn_3Sn | 20 Å MgO | 20 Å Ta. (d) – (e) Pulse length dependence for Mn_3Ge. The films stacks are: MgO (001) | 20 Å MgO | 50 Å CoGa | 15 and 20 Å Mn_3Ge | 20 Å MgO | 20 Å Ta.

4.5. Under external Fields – unraveling the mechanism of DW motion

To examine the DW dynamics, an in-plane magnetic field can be exerted to the DW motion since the in-plane field efficiently controls the internal structure of DW[31,97,98], which is crucial to uncovering the underlying physics of the DW motion. An external magnet which can apply in-plane fields, is fitted on the Kerr microscope setup, so that the sample is always centered to the two magnet cores. The direction of the applied field can be changed by rotating the sample in respect to the magnet. Fields can be applied along x and y axes, namely H_x and H_y.

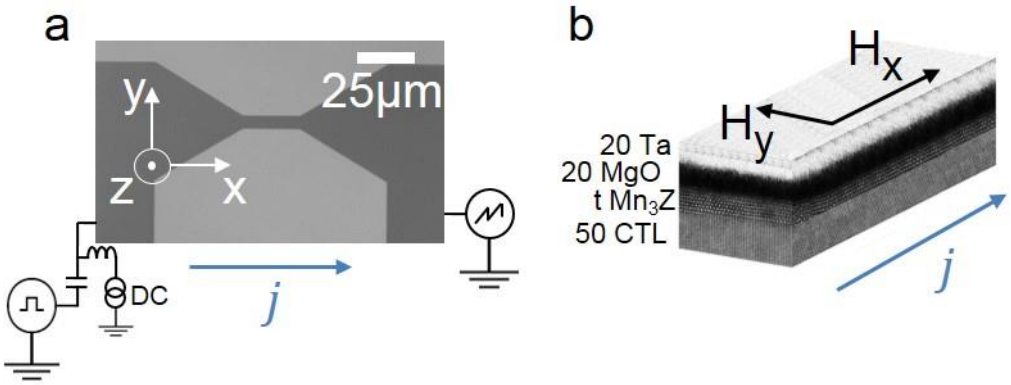

Figure 4.7 (a) Microscopy image of the nanowire with the contact pads, schematically representing the direction of the *x y z* axes and current direction. (b) Illustration of the wire with the layers it comprises of. Also showing positive directions of H_x, H_y and the direction of positive current flow.

Delicate alignment is required to level the sample with respect to the field. In other words, to make sure that the field is applied parallel to the sample plane as to eliminate any out of plane component field contribution to the DW motion. To do so, a relatively high in-plane field is applied and with a given current density it is confirmed that the DW would move for the same distance when creating symmetric conditions of opposite field/current direction.

Lastly, a certain current density, maintaining 100 ns pulse duration for consistency, was chosen such that the DW can freely move ($J > J_c$). As well, the current density cannot

be too high, because in some cases, when under in-plane fields, the DW velocity becomes 5 or even 10 times faster, the DW travels throughout the entire wire in a single pulse step. In most cases, the current density used is the value centered between J_c and the maximum current density before DW nucleation takes place and allows for several pulse steps to lessen the measured velocity error by averaging.

In Figure 4.8 is shown the DW motion for ↑↓ DW configuration of 15 Å Mn_3Ge and both ↑↓, ↓↑ for 20 Å Mn_3Ge. Note that different current densities were used for H_x and H_y. The applied field is span from positive to negative values and plotted. Moreover, both positive and negative current pulses are used and represented by closed and open symbols respectively.

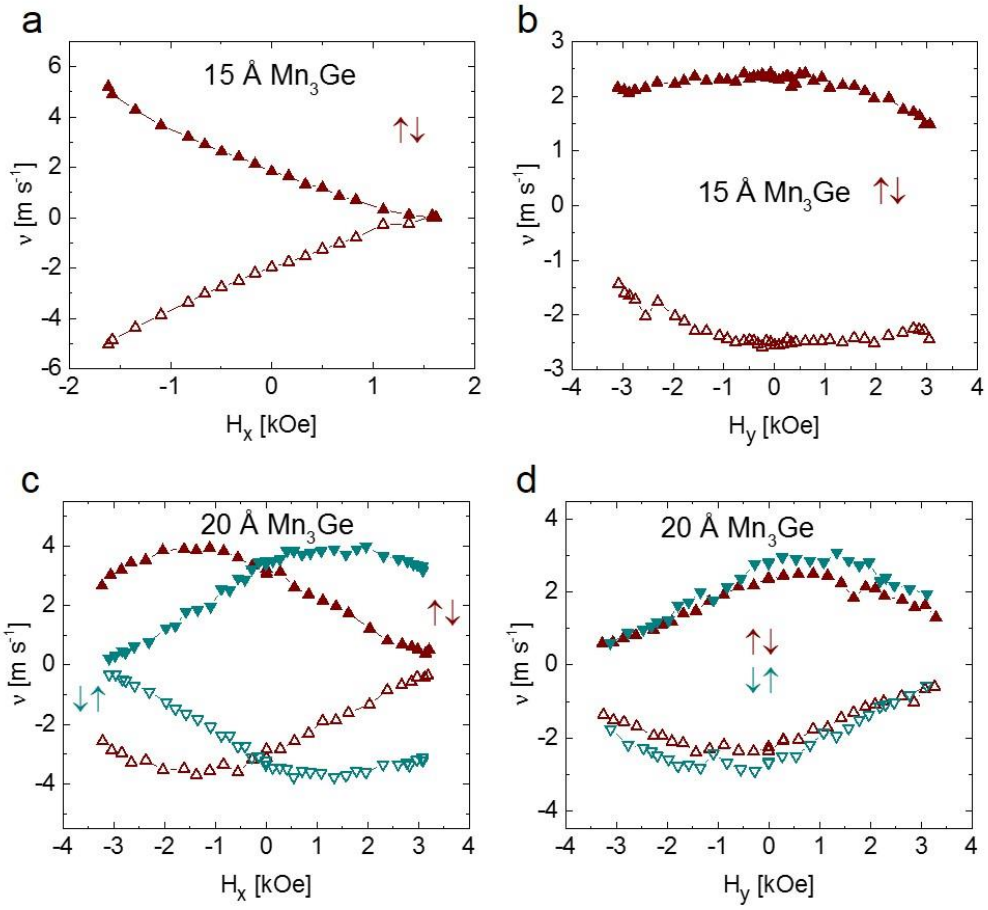

Figure 4.8 15 Å Mn_3Ge DW velocity dependence for (a) H_x and (b) H_y external fields for ↑↓ DW configuration with current densities: $|J^{Hx}| = 3.3 \cdot 10^7$ A cm^{-2} and $|J^{Hy}| = 3.5 \cdot 10^7$ A cm^{-2}. 20 Å Mn_3Ge DW velocity dependence for (c) H_x and (d) H_y external fields for ↑↓ and ↓↑ DW configurations. Current densities used: $|J^{Hx}| = 4.7 \cdot 10^7$ A cm^{-2} and $|J^{Hy}| = 4.3 \cdot$

10^7 A cm^{-2}. Closed (open) symbols represent positive (negative) current flow. Films stacks: MgO (001) | 20 Å MgO | 50 Å CoGa | 15 and 20 Å Mn_3Ge | 20 Å MgO | 20 Å Ta.

In Figure 4.9 is shown the DW velocity dependence on the applied in-plane fields H_x and H_y for 7.5, 10 and 15 Å Mn_3Sn thick Heusler films.

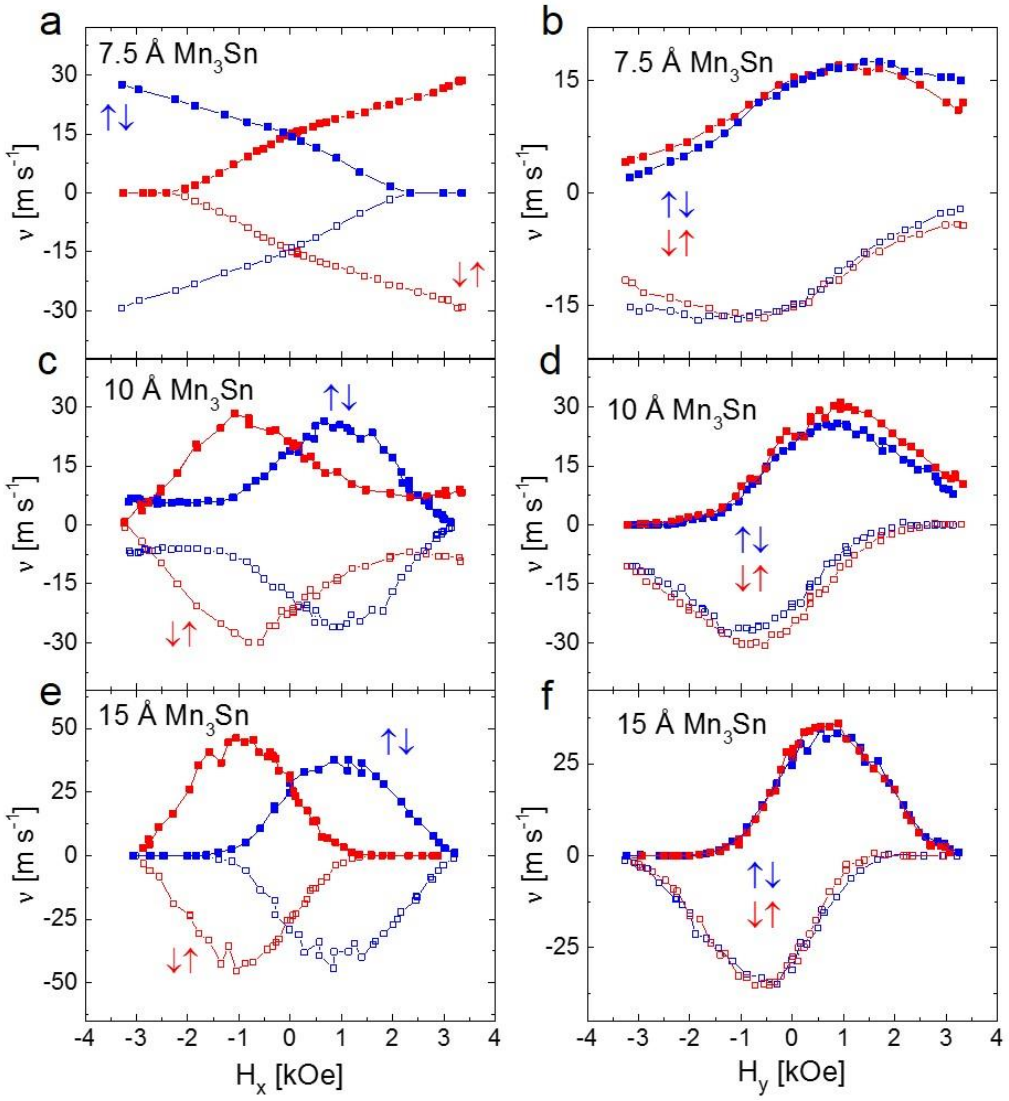

Figure 4.9 7.5 Å Mn_3Sn DW velocity dependence for (a) H_x and (b) H_y external fields for ↑↓ and ↓↑ DW configurations with current densities: $|J^{Hx}| = 5.1 \cdot 10^7$ A cm^{-2} and $|J^{Hy}| = 5.0 \cdot 10^7$ A cm^{-2}. 10 Å Mn_3Sn DW velocity dependence for (c) H_x and (d) H_y external fields for ↑↓ and ↓↑ DW configurations. Current densities used: $|J^{Hx}| = 8.5 \cdot 10^7$ A cm^{-2} and $|J^{Hy}| = 8.6 \cdot 10^7$ A cm^{-2}. 15 Å Mn_3Sn DW velocity dependence for (e) H_x and (f) H_y external fields for ↑↓

and ↓↑ DW configurations. Current densities used: $|J^{Hx}| = 9.0 \cdot 10^7$ A cm^{-2} and $|J^{Hy}| = 9.3 \cdot 10^7$ A cm^{-2}. Closed (open) symbols represent positive (negative) current flow. Films stacks: MgO (001) | 20 Å MgO | 50 Å CoGa | 7.5 or 10 or 15 Å Mn_3Sn | 20 Å MgO | 20 Å Ta.

Similar behavior is observed for the 20 Å Mn_3Sb DW velocity dependence on H_x and H_y shown in Figure 4.10.

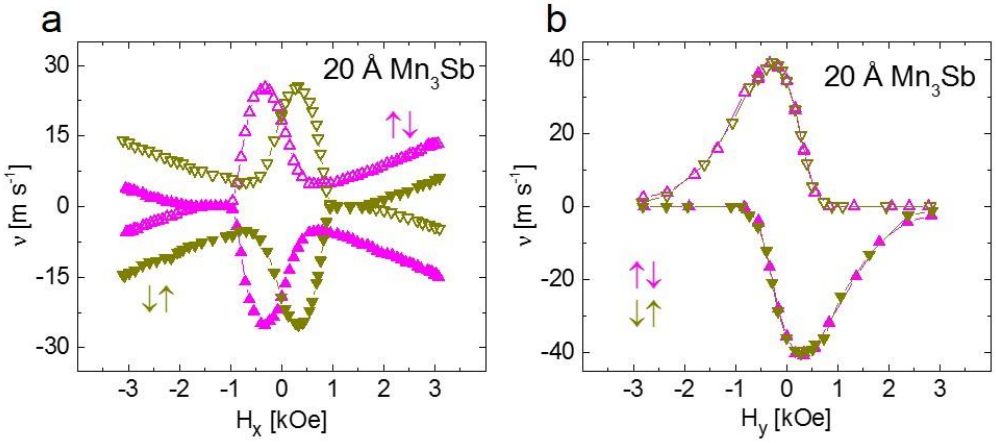

Figure 4.10 20 Å Mn_3Sb DW velocity dependence for (a) H_x and (b) H_y external fields for ↑↓ and ↓↑ DW configurations with current densities: $|J^{Hx}| = 3.1 \cdot 10^7$ A cm^{-2} and $|J^{Hy}| = 3.9 \cdot 10^7$ A cm^{-2}. Closed (open) symbols represent positive (negative) current flow. Films stack: MgO (001) | 20 Å MgO | 50 Å CoGa | 20 Å Mn_3Sb | 20 Å MgO | 20 Å Ta.

Comparing the DW velocity dependence on external applied in-plane fields shows some characteristic features and the collected data has a similar dependence for all the films. In the H_x field dependence, the DW velocity has a linear component, seen in higher H_x fields, which is obstructed by the dome shape feature. A significant finding is that in the case of Mn_3Sn, where three different thicknesses (7.5, 10, 15 Å) were grown, fabricated and measured, that there is a common dome peak in H_x centered around ±1000 Oe (+ ↑↓, − ↓↑) regardless of the thickness of the magnetic Heusler.

For all the Mn_3Z (Z=Ge, Sn, Sb) in study, the DW velocity dependence on H_x field, is a mirror image for the two DW configurations, ↑↓ and ↓↑. The findings on the DW motion in Heusler films reflect chiral DW motion and are indication for a DMI field[97,99–103], H_{DM}, oriented along the x-axis. Previous reports on DW motion under in-plane fields have found similar H_x field dependence on the presence of a DMI field

along the x-axis[31,79,86,102,103] and a dome shape feature and are explained in the next section. This DMI field, oriented along the x-axis, sets the DWs to be of Néel type, and the orientation of H_{DM} sets the chirality, left (counterclockwise) or right (clockwise).

Whereas in the dependence on H_y field, the DW velocity is unchanged for the two different DW configurations, but the curves are reversed for positive and negative applied current pulses. This DW velocity dependence on H_y field shows that there is a contribution from spin-orbit torques arising from the interface with the CTL.

4.5.1. Illustration of the DW within a nanowire showing the torques and fields

To explain the DW motion driving mechanism following the H_x, H_y applied field findings, a depiction of the nanowire is illustrated with the acting torques from v-STT and the influence of H_x, H_{DM} or H_y in Figure 4.11. The nanowire is represented in a top view, so the ↑ domain is indicated as ⊙ and the ↓ domain as ⊗. The magnetization profile of the DW is set accordingly to the presence of an H_x, H_{DM} or H_y field only.

Considering positive spin polarization ($P > 0$), when the current J starts been applied from right to left in the nanowire, spin polarized electrons start traversing through the DW from left to right. The volume spin torque causes the moments in the DW to rotate out of the plane of the wire in the +z direction. This torque is $\boldsymbol{\tau_{STT}}$ indicated in Figure 4.11b. As a result, this gives rise to a damping torque $\boldsymbol{\tau_d} = \alpha \boldsymbol{M} \times {}^{d\boldsymbol{M}}/_{dt}$, whose direction is along y. This damping torque causes the precessional motion of the DW along the wire motion. At the same time, the DW moments experience the $\boldsymbol{H_x}$ or $\boldsymbol{H_{DM}}$ because they are non colinear and a torque $\boldsymbol{\tau_x} = -\gamma \boldsymbol{M} \times \boldsymbol{H_x}$ or $\boldsymbol{\tau_{DM}} = -\gamma \boldsymbol{M} \times \boldsymbol{H_{DM}}$ arises, as illustrated in Figure 4.11d. This torque, counteracts $\boldsymbol{\tau_{STT}}$. The upper bound of $|\boldsymbol{\tau_x}|$ or $|\boldsymbol{\tau_{DM}}|$ is $\gamma M H_x$ or $\gamma M H_{DM}$ respectively. And the DW velocity is maximum when the applied H_x field is $H_x = -H_{DM}$, at the center (peak) of the dome. The DW velocity decreases away from this point for any increasing or decreasing in-plane fields, creating this dome shape characteristic feature curves.

The position of the dome peak in H_x field, defines the magnitude of the H_{DM} field and is of opposite sign and is found to be unchanged for different Heusler thicknesses. Its sign does change though depending on the Mn_3Z Heusler material. H_{DM} is positive for Mn_3Ge and Mn_3Sb, when considering an ↑↓ (⊙|⊗) DW and have clockwise chirality. And H_{DM} is negative for Mn_3Sn for an ↑↓ DW, which gives counterclockwise chirality.

In Figure 4.11e-h is illustrated in a similar way the scenario where only H_y is applied. The contribution from a chiral spin-orbit torque that arises from a spin Hall effect in the CoGa CTL, accounts for the asymmetry of the domes observed in H_x field dependence, thus the domes appear geometrically distorted. Also, the spin Hall effect accounts for the off-centering that appears in the H_y dependence, which is opposite for positive and negative applied currents.

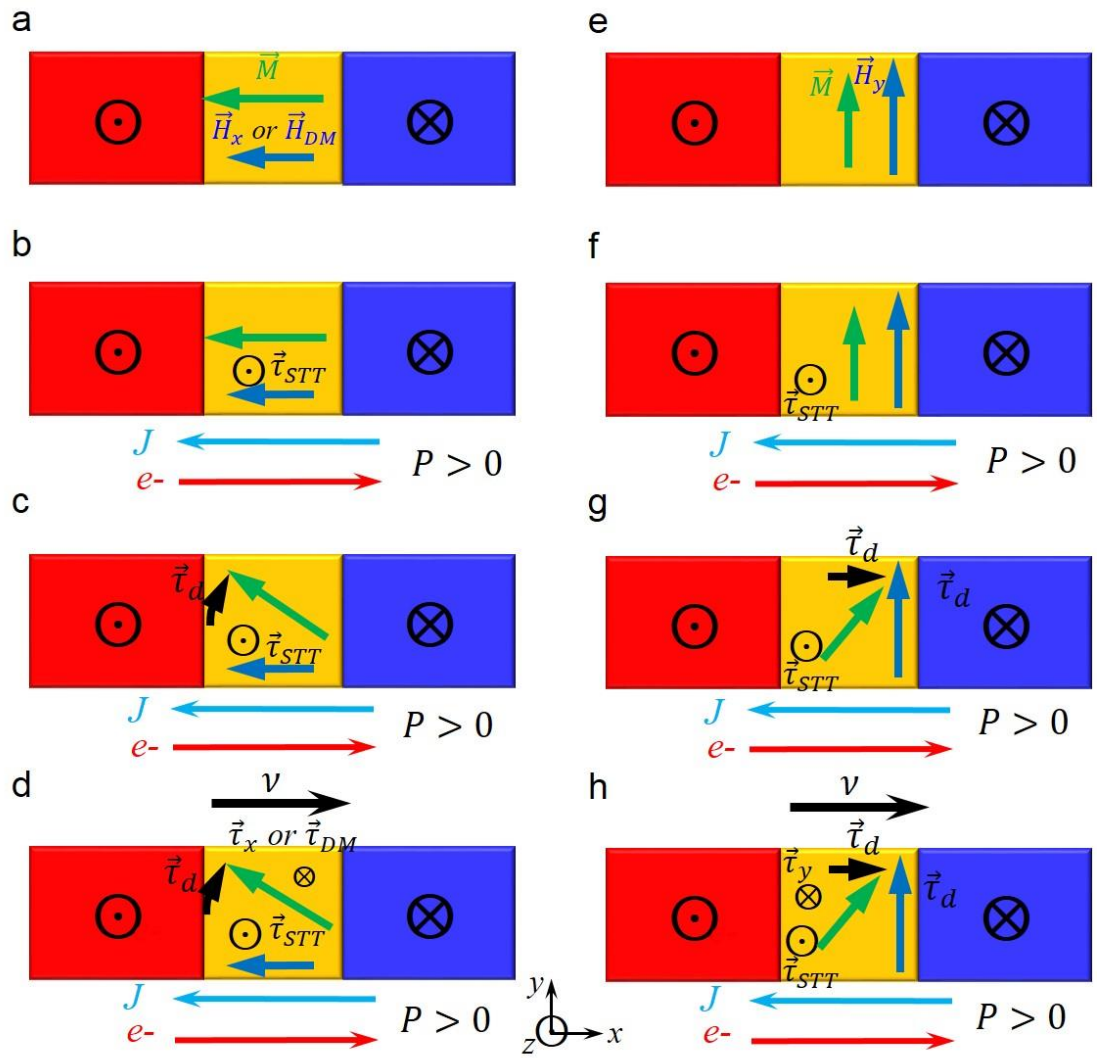

Figure 4.11. Top view illustration of current driven DW motion for an ⊙|⊗ DW when $P > 0$. The generated and acting torques are illustrated sequentially starting from $J = 0$ to applying a current in the right to left direction. (a) – (d) In the presence of H_x or H_{DM}. (e) – (h) In the presence of H_y.

4.6. Bulk DMI and Spin-orbit Torques

The most important finding is that there is a DMI attributed to the DW in these Heusler films which sets the chirality (left handed or right handed as explained). The origin of the DMI, as to whether it is interfacial[101,104,105] or bulk[106,107], can be elucidated by eliminating any interfacial contributions. To do so, a layer identical to the CTL was grown directly above the Heusler layer. Indeed, if the chiral DMI[31,97], is of interfacial origin, it would cancel out the contribution from each layer (bottom or top) as they would compensate each other.

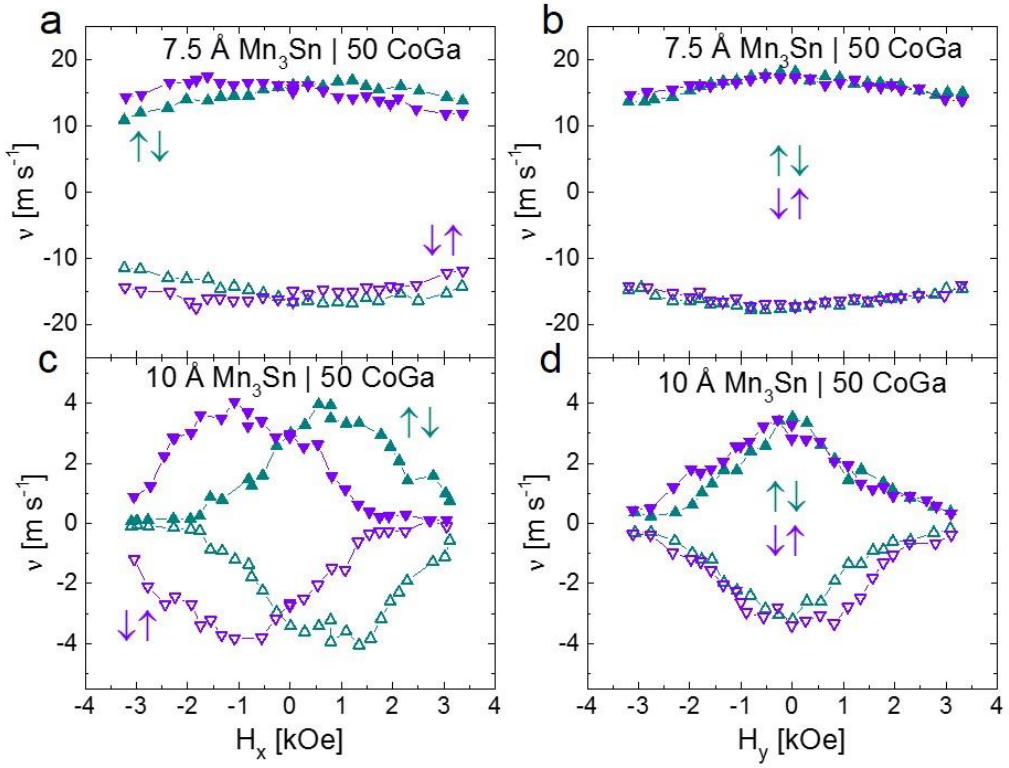

Figure 4.12 DW velocity dependence on in-plane fields with a capping layer identical to the CTL. 7.5 Å Mn_3Sn DW velocity dependence for (a) H_x and (b) H_y external fields for ↑↓ and ↓↑ DW configurations with current densities: $|J^{Hx}| = 5.7 \cdot 10^7$ A cm^{-2} and $|J^{Hy}| = 5.7 \cdot 10^7$ A cm^{-2}. 10 Å Mn_3Sn DW velocity dependence for (c) H_x and (d) H_y external fields for ↑↓ and ↓↑ DW configurations with current densities: $|J^{Hx}| = 6.8 \cdot 10^7$ A cm^{-2} and $|J^{Hy}| = 6.8 \cdot 10^7$ A cm^{-2}. Films stacks: MgO (001) | 20 Å MgO | 50 Å CoGa | 7.5 or 10 Å Mn_3Sn | 50 Å CoGa | 20 Å MgO | 20 Å Ta. Closed (open) symbols represent positive (negative) current flow.

50 Å CoGa is grown directly over 7.5 Å and 10 Å Mn_3Sn Heuslers. This capping layer is grown identical to the 50 Å CoGa CTL used to promote the Heusler growth, without any additional annealing step. In Figure 4.12 is shown the DW velocity dependence on H_x and H_y applied in-plane fields for these films. Comparing this DW motion results with those found in Figure 4.9, where no capping layer similar to the CTL is grown, it is clearly seen that the dome peak position is unchanged which indicates that the DMI is of bulk origin. This is more obvious for the thicker, 10 Å Mn_3Sn Heusler in the H_x field dependence (Figure 4.9c-d and Figure 4.12c-d).

Furthermore, distinct differences appear as a result of the spin-orbit torque suppression. For the 50 Å CoGa capping layer, in the H_y field dependence, the DW velocity does not show the opposite shift for opposite current flow. Additionally, the DW velocity is now centered around $H_y = 0$. This is characteristic of the compensation of the Spin Hall Effect from the bottom interface (50 Å CoGa CTL) with the top interface (similar 50 Å CoGa capping layer). It is also noticeable that the spin transparency at the top (Mn_3Sn | CoGa capping layer) and bottom (CoGa CTL | Mn_3Sn) interfaces is almost identical since the DW velocity is centered around $H_y = 0$ such that the spin Hall effects from the two interfaces are almost completely compensated. Lastly, the characteristic dome shape in H_x field dependence is no longer distorted and it is now symmetric.

In the thinner 7.5 Å Mn_3Sn, where the respective contribution of the chiral spin torque is comparatively larger with respect to the thicker 10 Å Mn_3Sn, the introduction of the 50 Å CoGa capping layer makes the dome visible in the H_x field dependence. This is again due to the compensation of the bottom and top spin Hall effect contributions to the spin-orbit torque. In the H_y field dependence of the DW velocity, the dependence

on the current direction is eliminated and it is centered around $H_y = 0$, as previously discussed.

4.7. Conclusions

In this chapter, utilizing the methods described in chapter 3, Mn_3Ge, Mn_3Sn and Mn_3Sb ultrathin Heuslers with great perpendicular magnetic anisotropies were grown on different CTLs. Nanowire devices are patterned from these films and the current induced domain wall motion is studied for all three Heuslers on CoAl, CoGa and CoSn chemical templating layers.

The fastest DW velocity achieved is -129 ms^{-1} for 10 Å $Mn_{3.1}Sb$ with a critical current density of $J_c = 5.0 \cdot 10^6 \mathrm{A\ cm}^{-2}$. The lowest current density recorded was found for 10 Å Mn_3Sb and is $J_c = 2.8 \cdot 10^6 \mathrm{A\ cm}^{-2}$.

The main mechanism driving the DWs in these Heusler films is volume spin transfer torque (STT) and the DWs move in a precessional motion along the current flow for Mn_3Ge and Mn_3Sn while the DWs move along the electron flow in Mn_3Sb as per spin polarization being negative for Mn_3Ge, Mn_3Sn and positive for Mn_3Sb.

Important contributions to the DW motion under externally applied in-plane fields H_x and H_y reveal a significant bulk chiral Dzyaloshinskii-Moriya exchange interaction along the *x* axis and sets Néel type DWs with a given chirality. This is further confirmed using capping layers directly over the Heuslers which are identical to the CTL. The bulk DMI accounts for the appearance of a dome shape feature in the H_x field dependence of the DW velocity for these Heusler films.

Chiral spin-orbit torques reveal a spin Hall effect contribution from the CoGa CTL which is of the same sign as in Pt/ferromagnet. This torque accounts for the observation that the dependence of the DW velocity on H_y is not centered around $H_y = 0$.

Mn_3Ge, Mn_3Sn and Mn_3Sb DMI fields are extracted from the dome peak position in the H_x field dependence of the DW velocity. The DMI field stabilizes the Néel

configuration and gives a chirality to the DW. When a current is applied along the wire axis, the spin accumulation from the spin Hall effect exerts a torque transverse to the H_{DM} direction. Thus, the DW experiences a chiral spin-orbit torque (SOT) whose direction in *z* is influenced by the direction of the H_{DM} since the spin Hall angle is set by the CoGa CTL[97,98]. That leads to the favorable or disadvantageous contribution of the SOT to the DW motion driven mainly by STT. The results are summarized in Table 4.1.

Mn_3Z Heusler	STT direction	chirality	H_{DM} (Oe)	CoGa θ_{SH}	SOT contribution
Mn_3Ge	Current flow	CW	1400	positive	unfavorable
Mn_3Sn	Current flow	CCW	-1000	positive	favorable
Mn_3Sb	Electron flow	CW	350	positive	favorable

Table 4.1 Summary of spin polarization direction, DMI direction, SHA and SOT contribution to the DW motion driven mainly by STT for Mn_3Ge, Mn_3Sn and Mn_3Sb. Note that H_{DM} is along the *x* axis.

5. Tailoring the SOTs and Bulk DMI field

Spin-orbit torques are widely used in spintronic devices and are proposed for future technological applications. Depending on the application requirements, the spin-orbit torque contribution is greatly valued, and it can be of key importance to the functionality of the device. Moreover, previous work[97,103] has shown the influence on the spin-orbit torque when different overlayers or underlayers are introduced in thin ferromagnetic films and the DW motion is examined.

The chemical template layering concept, along with the tunable, multi-functional Heuslers, allow for introducing overlayers while preserving the magnetic properties of the ultrathin Heuslers. The overlayers are chosen so that the chiral spin-orbit torques generated will affect drastically the domain wall motion in the ultrathin ferrimagnetic Heuslers grown on Chemical Templating Layers. Overlayers of Pt, W, grown by DC-sputtering, are introduced and the SOT contribution is altered. Additionally, the tunability of the Heusler films is demonstrated by changing its composition which in turn tunes the bulk DMI field.

5.1. Tuning the spin-orbit torques by atomically engineering the overlayers

In the previous chapter, a CoGa overlayer was introduced to evidence the bulk DMI in the Heusler films. To extend the scope of the overlayers that can be used, one can think of using heavy metals which have high Spin Hall Angle (SHA) such as tungsten[75] (W) or platinum (Pt)[108]. The Spin Hall Angle is defined as $\theta_{SH} = \frac{J_y}{j_{total}}$ and represents the amount of spin current that can be generated when flowing electrical current in the transverse direction. To avoid any interfacial effects arising from direct contact of the W or Pt with the Heusler, a 5 Å CoGa layer first capped the Heusler and the W or Pt

overlayer was grown subsequently. The resistivities for the W and Pt overlayers used, are: $\rho^{W} = 173\ \mu\Omega\,\text{cm}$ and $\rho^{Pt} = 19.3\ \mu\Omega\,\text{cm}$, as measured from calibration films. From the resistivity of W, it is expected that it is mostly alpha phase W[75].

20 Å Mn_3Sb was used in all cases, while the overlayer changed from 20 Å W to 5 Å Pt, 10 Å Pt and 20 Å Pt. All films exhibited great PMA and the DW motion vs the current density *J*, is shown in Figure 5.1.

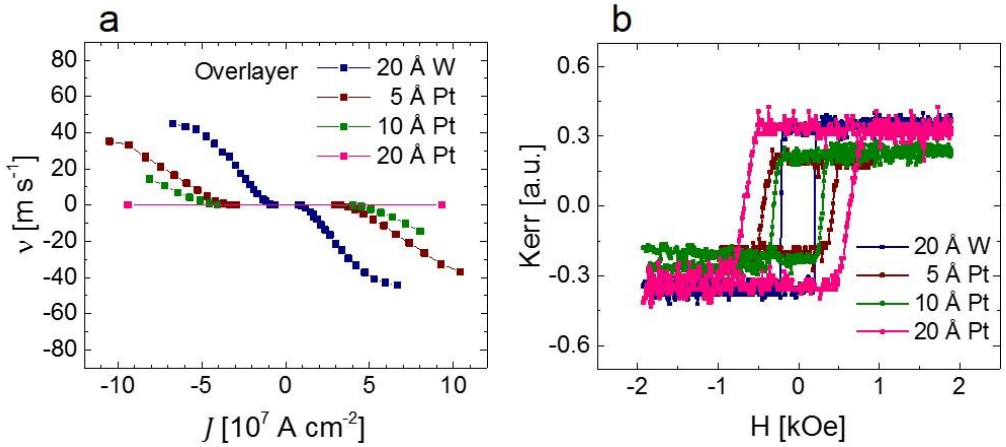

Figure 5.1 (a) Domain Wall motion dependence on W and Pt overlayer vs current density. (b) Corresponding P- MOKE hysteresis loops. The film stacks are: MgO (001) | 20 Å MgO | 50 Å CoGa | 20 Å Mn_3Sb | 5 Å CoGa | 20 Å W or 5, 10, 20 Å Pt | 20 Å MgO | 20 Å Ta.

The DW velocity is strongly affected by these capping layers and has opposite effects for the 20 Å W as compared to the 5 Å, 10 Å and 20 Å Pt. Pt is known to have an opposite spin Hall angle to the one of W (negative for the first and positive for the latter). From the systematic decrease of the DW velocity, with the increase of Pt overlayer thickness, one can deduce that the spin-orbit torques are suppressed. The suppression of the spin-orbit torques with Pt overlayer signifies that CoGa CTL and Pt have the same sign of SHA, as their respective contribution opposes each other. Very interestingly, the dependence of the DW velocity to in-plane applied fields reveals that this holds true, as seen in Figure 5.2. For increasing Pt thickness, the overall spin-orbit torques are suppressed to a point that the spin Hall effect reverses when a thicker 10 Å Pt overlayer is introduced, as seen from the H_y field dependence.

On the other hand, for the W overlayer, the enhancement of the spin-orbit torques can be visibly identified by the disappearance of the dome shaped feature in the DW velocity dependence on H_x and is therefore dominated by the slope (Figure 5.2a-b).

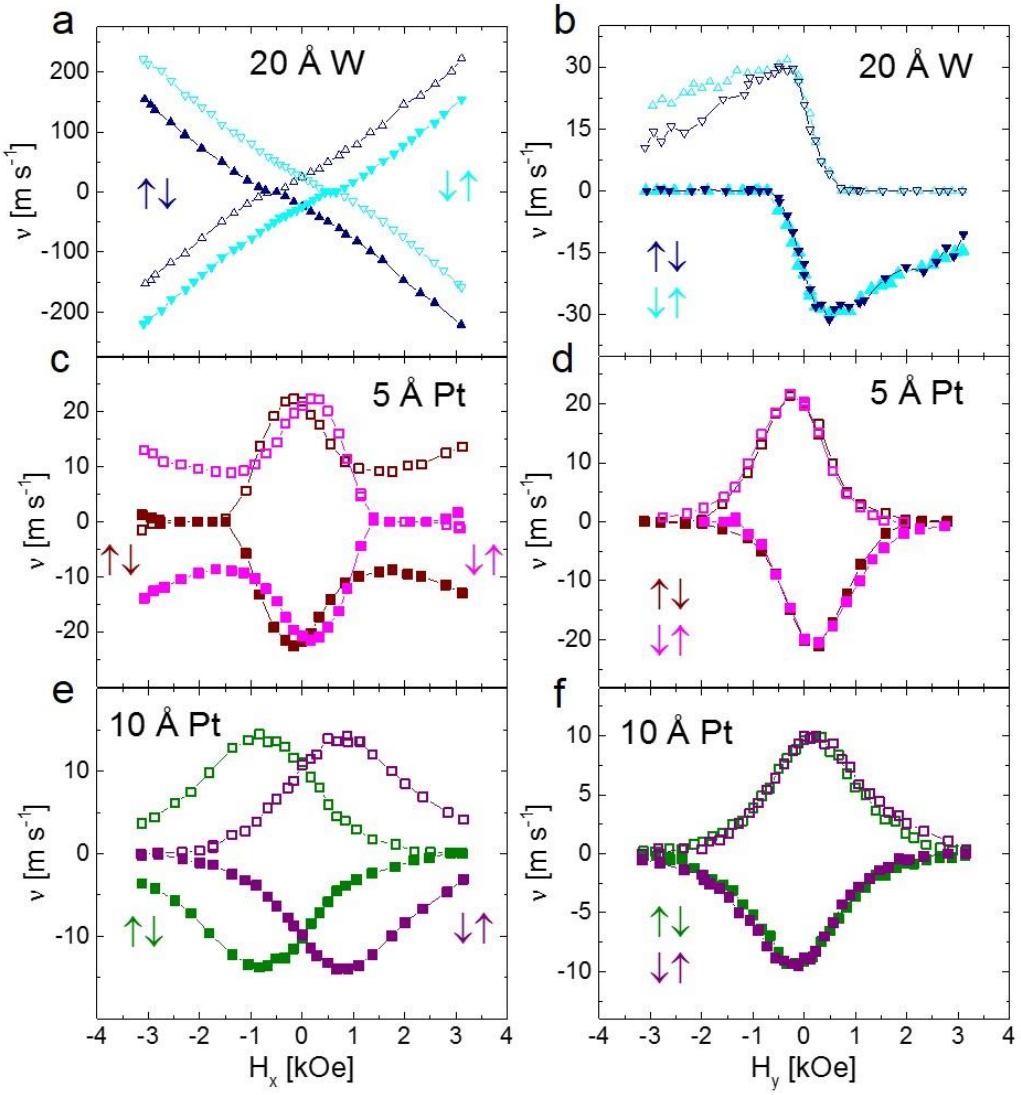

Figure 5.2 ↑↓ and ↓↑ DW velocity dependence on (a) H_x and (b) H_y external fields for 20 Å W overlayer with current densities: $|J^{Hx}| = 3.4 \cdot 10^7$ A cm^{-2} and $|J^{Hy}| = 3.5 \cdot 10^7$ A cm^{-2}. ↑↓ and ↓↑ DW velocity dependence on (c) H_x and (d) H_y external fields for 5 Å Pt overlayer with current densities: $|J^{Hx}| = 7.4 \cdot 10^7$ A cm^{-2} and $|J^{Hy}| = 7.2 \cdot 10^7$ A cm^{-2}. ↑↓ and ↓↑ DW velocity dependence on (e) H_x and (f) H_y external fields for 10 Å Pt overlayer with current densities: $|J^{Hx}| = 7.2 \cdot 10^7$ A cm^{-2} and $|J^{Hy}| = 7.0 \cdot 10^7$ A cm^{-2}. The film stacks are: MgO (001) | 20 Å MgO | 50 Å CoGa | 20 Å Mn_3Sb | 5 Å CoGa | 20 Å W or 5, 10 Å Pt | 20 Å MgO | 20 Å Ta. Closed (open) symbols represent positive (negative) current flow.

In addition, the DW velocity vs H_y, shows that for 10 Å Pt, the H_y field asymmetry changes sign which means that the dominant spin-orbit torque contribution derives from the top layer and is overcoming the contribution from the bottom one. For 20 Å Pt, the spin-orbit torque from the top layer is high enough to reduce the DW velocity so low that the DW would not move with the in-plane fields.

5.2. Tailoring the bulk DMI field with composition of Mn_xSb

The chemical templating technique is so effective that the tunability of the Heusler compound can be beneficially used, in this case changing the Mn_xSb composition for x= 2.0, 2.4, 2.5, 3.0, 3.3. A new series of samples was grown where the DC co-sputtering gun levels for the power supply of the Sb target used to achieve these compositions are correspondingly: 20, 22, 24, 26 and 28 Watts. The two Mn co-sputtering gun target power supplies are set at 66 Watts and remain unchanged. The composition of Mn_xSb of each film was verified by RBS and PIXE on the films before patterning. In Figure 5.3 is shown the corresponding DW motion and P-MOKE hysteresis loops for 20 Å Mn_xSb grown on CoGa CTL with x=20, 2.4, 2.5, 3.0 and 3.3.

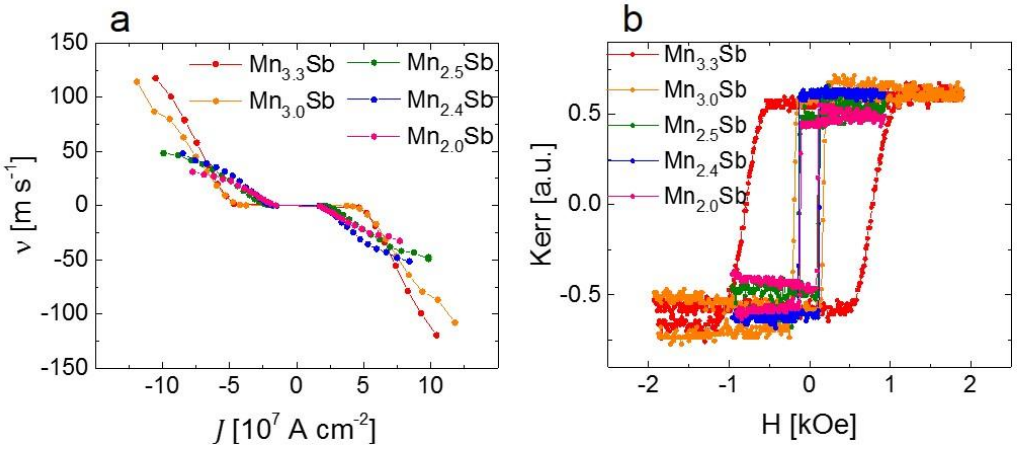

Figure 5.3 (a) Mn_xSb DW velocity vs current density *J*. (b) Corresponding P-MOKE hysteresis loops. The films stacks are: MgO (001) | 20 Å MgO | 50 Å CoGa | 20 Å Mn_xSb | 20 Å MgO | 20 Å Ta, x= 2.0, 2.4, 2.5, 3.0, 3.3.

The critical current density, J_c, lowers when Mn concentration is reduced which can be due to lower intrinsic pinning. The DW velocity versus in plane field dependence for these films (in Figure 5.4a), shows that the dome, and as a result, the peak of the dome, is shifted to lower H_x fields with decreasing Mn concentration. In Figure 5.4b is shown the H_y in plane field dependence to the velocity of an ↑↓ DW. ↑↓ DW configuration and different current densities are used for the H_x field dependence to better visualize the shift of the dome peak.

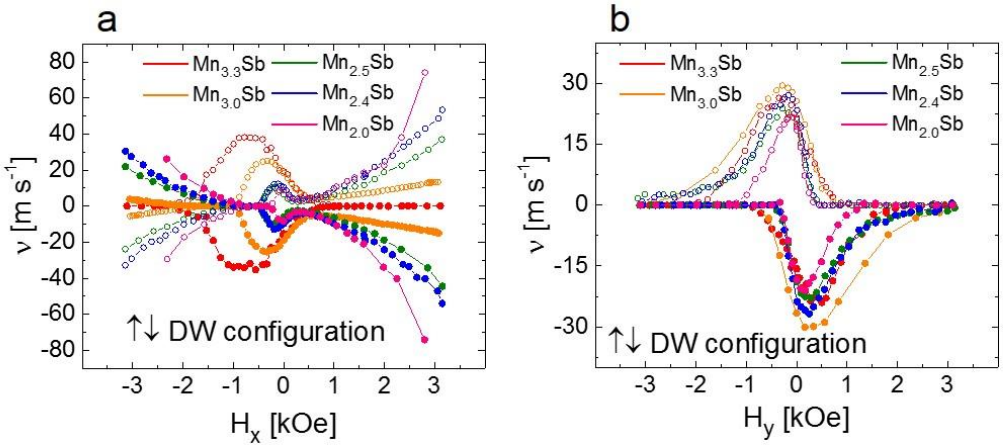

Figure 5.4 (a) 20 Å Mn_xSb DW velocity dependence on H_x for ↑↓ DW configuration with current densities used: $|J^{Hx}| = 2.8, 2.9, 3.1, 3.1, 5.9 \cdot 10^7$ A cm^{-2}. (b) 20 Å Mn_xSb DW velocity dependence on H_y for ↑↓ DW configuration with current densities used: $|J^{Hy}| = 4.3, 4.2, 5.0, 3.7, 5.9 \cdot 10^7$ A cm^{-2}. The films stacks are: MgO (001) | 20 Å MgO | 50 Å CoGa | 20 Å Mn_xSb | 20 Å MgO | 20 Å Ta, x= 2.0, 2.4, 2.5, 3.0, 3.3 respectively. Closed (open) symbols represent positive (negative) current flow.

The dome peak position in the H_x field represents the DMI field since H_x counterbalances H_{DM} at the dome position, as discussed in chapter 4.5. Therefore, it is clearly seen that by tuning the Mn_xSb composition, the bulk DMI field changes dramatically. The different compositions of $Mn_{2.0}Sb$, $Mn_{2.4}Sb$, $Mn_{2.5}Sb$, $Mn_{3.0}Sb$, $Mn_{3.3}Sb$ can have different magnetization values which proportionally changes the DMI field.

5.3. Conclusions

In this chapter, the tunability and multi-functionality of the ultrathin Heusler films and the effectiveness of the chemical template layering is demonstrated.

Overlayers with high spin Hall effect contribution are introduced, resulting in tweaking the chiral spin-orbit torques seen from the Heusler Domain Wall motion. More specifically, when W (tungsten) or Pt (platinum) overlayers are introduced, the spin-orbit torques are enhanced or suppressed, respectively. The SHA of the CoGa CTL is of the same sign as the Pt is. Thus, increasing the Pt overlayer thickness results in the systematic reduction of the DW velocity.

The high tunability of the Heusler films is further confirmed by the systematic increase of the bulk DMI field when changing the Heusler composition from $Mn_{2.0}Sb$ to $Mn_{2.4}Sb$, then $Mn_{2.5}Sb$ then $Mn_{3.0}Sb$ and finally $Mn_{3.3}Sb$. In all cases, 20 Å of Heusler film thickness is used. The DW velocity dependence on H_x in plane field shows the shift of the characteristic peak dome position. In Figure 5.5, is plotted the field value of the position of the peak of the dome with respect to x-composition of Mn_xSb which represents the DMI field, H_{DM}.

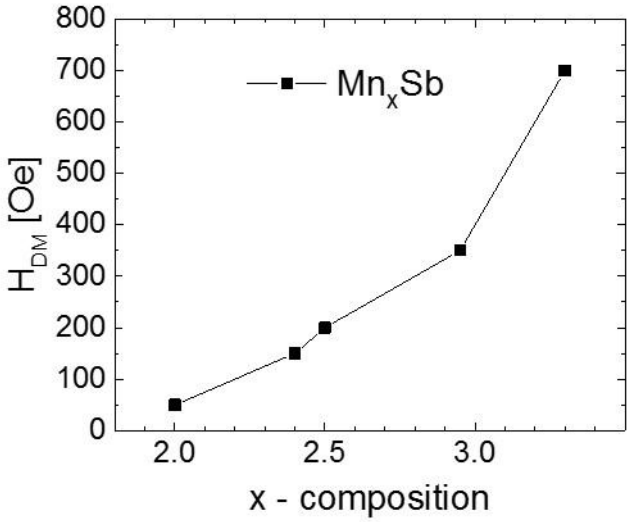

Figure 5.5 DMI field, H_{DM}, as a function of Mn_xSb composition.

The class of Heusler materials has extraordinary properties. The ability to tune the overlayers and the spin-orbit torque along with the Heusler itself, tuning the bulk DMI field by up to an order of magnitude shows significant advantages towards potential spintronic device applications now that it is demonstrated that these compounds can be prepared in ultrathin layers.

6. Mn_3Ge ex-situ annealing temperature dependence

The properties of ultrathin Mn_3Ge on CoAl CTLs with great PMA are studied post deposition. 20 Å Mn_3Ge Heuslers are grown with the methods described in chapter 3. The P-MOKE hysteresis loop of the blanket films are measured. Following, the films are annealed for 30 minutes each time, in vacuum, in a high field annealing furnace (ex-situ) with base pressure of $3 \cdot 10^{-8}$ Torr, under 1 Tesla out of plane applied field. The P-MOKE hysteresis loops are measured after each annealing step and the film is then annealed to a higher temperature.

6.1. P-MOKE dependence on ex-situ annealing temperature

The P-MOKE loops after each annealing step are shown in Figure 6.1. The film stacks are included in the figure legend. The black curves, show the hysteresis loop of the samples, as characterized by P-MOKE right after deposition. N.A. indicates that no post deposition annealing is yet applied.

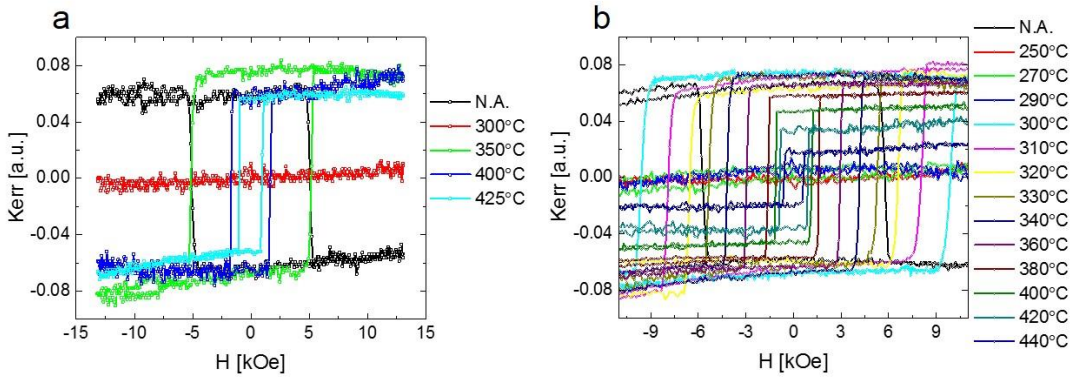

Figure 6.1 Post annealing P-MOKE signal for two films of Mn_3Ge. (a) MgO (001) | 20 Å MgO | 100 Å CoAl | 20 Å Mn_3Ge | 20 Å MgO | 20 Å Ta. (b) MgO (001) | 20 Å MgO | 50 Å CoAl | 20 Å Mn_3Ge | 20 Å MgO | 20 Å Ta.

From these P-MOKE results, it is identified that when no post-deposition annealing is applied yet, the P-MOKE hysteresis loop has a given Kerr signal directionality. When annealing at higher temperatures, the Kerr signal vanishes at about 250 – 300 °C annealing temperature. Subsequent annealing at higher temperatures reverses the Kerr signal direction seen in the P-MOKE hysteresis curves. The maximum temperature that can be applied in the high field furnace is 440 °C.

Of the two samples, introduced in Figure 6.1a and b, one was used for wide temperature step P-MOKE dependence measurements on the blanket film. After the last annealing step on that sample, it was fabricated to examine the DW motion. The other sample is submitted to a more detailed annealing temperature step scan for P-MOKE dependence measurements and both samples show similar P-MOKE study findings.

6.2. Domain Wall velocity dependence on ex-situ annealing temperature

After the last annealing step at 425 °C, the sample shown in Figure 6.1a is fabricated into nanowires in the way described in chapter 1.4. The DW motion is found to be reversed and dramatically improved compared to the DW motion shown in section 4.1.2. The annealed at 425 °C sample DW results are shown in Figure 6.2, along with the previous findings for 20 Å Mn_3Ge (taken from 4.1.2) for comparison. Their corresponding P-MOKE hysteresis loops are also shown.

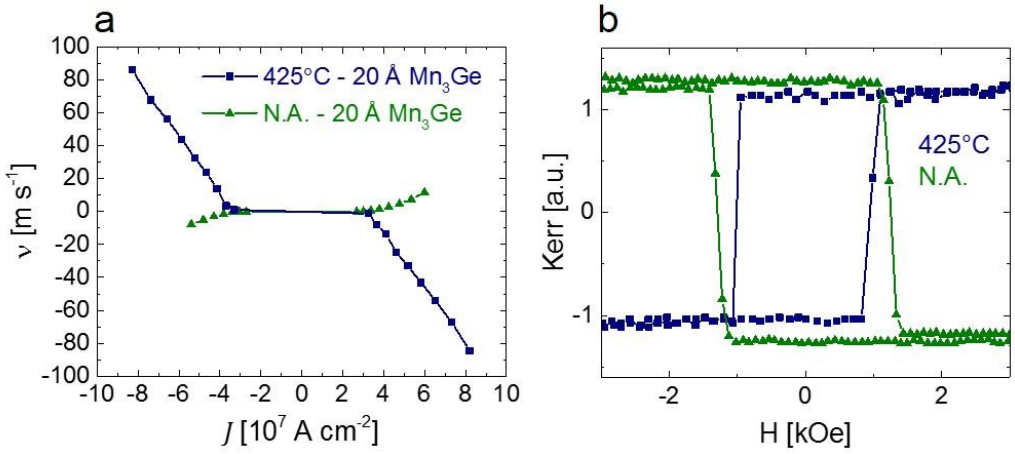

Figure 6.2 (a) DW velocity vs current density for the 20 Å Mn_3Ge Heusler film annealed at 425 °C in blue. (b) In blue is the corresponding P-MOKE hysteresis loop. Also showing for comparison the previous DW motion findings for the 20 Å Mn_3Ge Heusler films in green. The films stack for the 425 °C annealed film, in blue, is: MgO (001) | 20 Å MgO | 100 Å CoAl | 20 Å Mn_3Ge | 20 Å MgO | 20 Å Ta. The film stack for the not annealed Mn_3Ge is: MgO (001) | 20 Å MgO | 50 Å CoGa | 20 Å Mn_3Ge | 20 Å MgO | 20 Å Ta.

An important finding is that the direction of motion is now reversed, which indicates that the spin polarization is reversed and the DW motion reversal follows the reversal of the Kerr signal in the P-MOKE study. The DW velocity maximum is 86 ms^{-1} along the electron flow.

The DW velocity is also measured under externally applied in-plane fields H_x and H_y for ↑↓ and ↓↑ DW configurations, with the characteristic dome appearance in the H_x field dependence, but with much smaller H_{DM}. From the DW velocity dependence on the H_y applied field, the typical contribution from the SHE causes the asymmetry for the different positive and negative applied currents used. The results are presented in Figure 6.3.

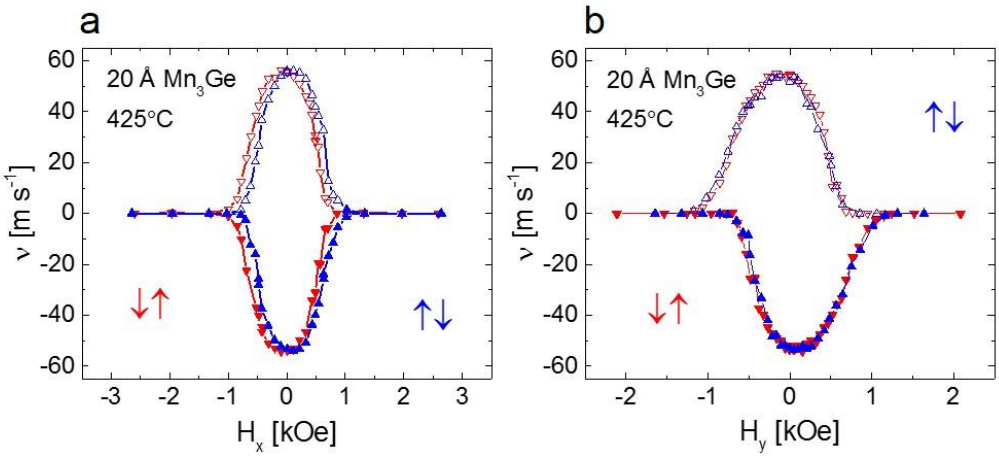

Figure 6.3 ↑↓ and ↓↑DW velocity vs (a) H_x and (b) H_y applied in plane fields. The film stack is: MgO (001) | 20 Å MgO | 100 Å CoAl | 20 Å Mn_3Ge | 20 Å MgO | 20 Å Ta, annealed at 425 °C ex-situ Closed, and open symbols represent positive and negative current respectively.

6.3. Conclusions

In this chapter, ultrathin Mn_3Ge Heusler compounds with great perpendicular magnetic anisotropy are grown on chemical templating layers of CoAl. Their PMA is seen from P-MOKE hysteresis curves in the as-deposited state. Using an ex-situ high field annealing furnace, the films are sequentially annealed and then their P-MOKE hysteresis loops is measured. The annealing duration is set to 30 minutes and the field applied in the furnace is 1 Tesla, out of plane direction.

Surprisingly, the P-MOKE hysteresis curves show a critical temperature where the Kerr signal minimizes and, at higher annealing temperatures, the Kerr signal reverses.

Domain Wall motion experiments are carried out in nanowires patterned from the Mn_3Ge film after the last annealing step at 425 °C. The DW motion is now opposite to the DW motion found before any annealing. The DW velocity becomes ~8 times higher, and it is along the electron flow direction. These results indicate that the spin polarization of Mn_3Ge changes sign with the annealing temperature.

7. 1-D analytical model for the ultrathin Heusler DW motion

The results observed for the Heusler Domain Wall motion over chemical templating layers study can be simulated, using a one-dimensional analytical model which accounts for the spin transfer term, DMI, applied in plane fields and spin-orbit torques as introduced in chapter 23

The one-dimensional model[66,98,109,110] is developed by Dr. See-Hun Yang and is helpful in providing insight and a quantitative understanding of the current driven domain wall dynamics. This model has been successful in describing the current induced motion of DWs in straight racetracks formed from single magnetic layers with perpendicular magnetic anisotropy (PMA) via a chiral spin torque[31,97], and in synthetic ferromagnets and antiferromagnets via an additional exchange coupling torque[98]. Here, this model is used to investigate the current driven DW motion in nanowires formed from Mn_3Z Heusler alloys.

In this chapter, the parameters on which the model is based on are introduced, along with the basic approximations. Then, the 1-D model fittings to the experimental DW motion results are presented and are in good agreement with the experimental findings shown and discussed in chapters 4 and 5.

7.1. 1-D analytical model for the DW motion in Heusler films

These ferrimagnetic Heuslers, are modeled by a ferromagnetic layer whose magnetization is the net magnetization of the two sub-lattices in the ferrimagnet. This is a reasonable approximation when the two sub-lattices are strongly anti-ferromagnetically coupled. Indeed, as shown in the 1-D model simulations, such a

model well accounts for many details of the current induced domain wall motion in the Heusler films of the study.

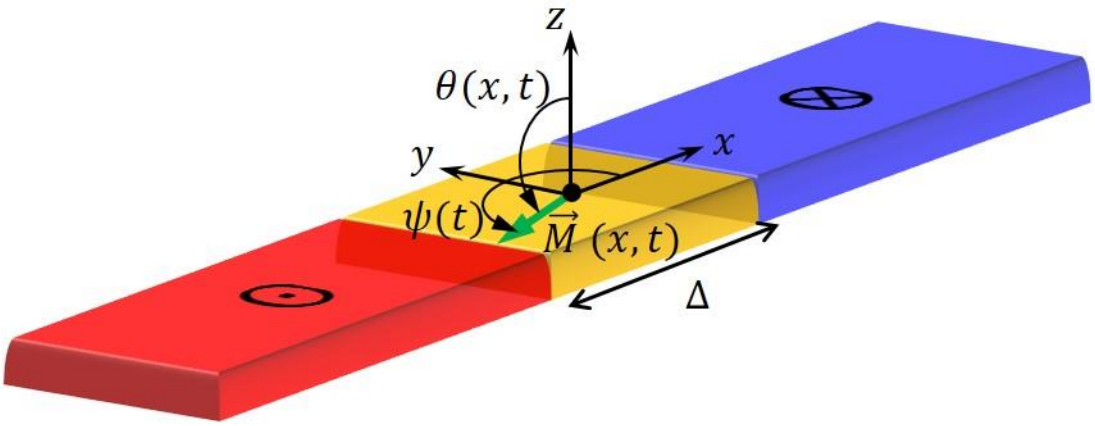

Figure 7.1 Depiction of an ↑↓ (⊙|⊗) Domain Wall within the nanowire, showing the profile of the magnetization, *M*, at the center of the DW, the azimuthal angle ψ and polar angle θ.

As illustrated in Figure 7.1, the basic assumption of the 1-D model is that the DW has a fixed magnetization profile with the magnetization rotated from the direction perpendicular to the layer, i.e. the *z*-axis, by a polar angle θ, and by the azimuthal magnetization angle ψ which is defined in the plane of the wire, with respect to the direction x. Note that ψ is constant and independent of the lateral position of the DW along the wire when it is manipulated either by current or magnetic field or a combination of the two. For the case of perpendicularly magnetized nanowires, the DW dynamics can be described within the 1-D model by two parameters, namely the position q of the DW along the wire and its conjugate momentum $2M_s\psi/\gamma$. M_s is the saturation magnetization. The DW motion in nanowires is governed by ψ, with the domain wall profile located at $\vec{r}$ and at time *t*, given by:

$$\theta(\vec{r},t) = 2\arctan\exp\left(\pm\frac{x-q}{\Delta}\right). \qquad \text{(eq.1)}$$

The upper $(+)$ and lower $(-)$ signs, correspond to the ↑↓, (⊙|⊗) and ↓↑, (⊗|⊙) DW configurations respectively. The full 1-D model derivation is given in the appendix 0.

7.2. 1-D model simulated curves for H_x, H_y DW velocity dependence

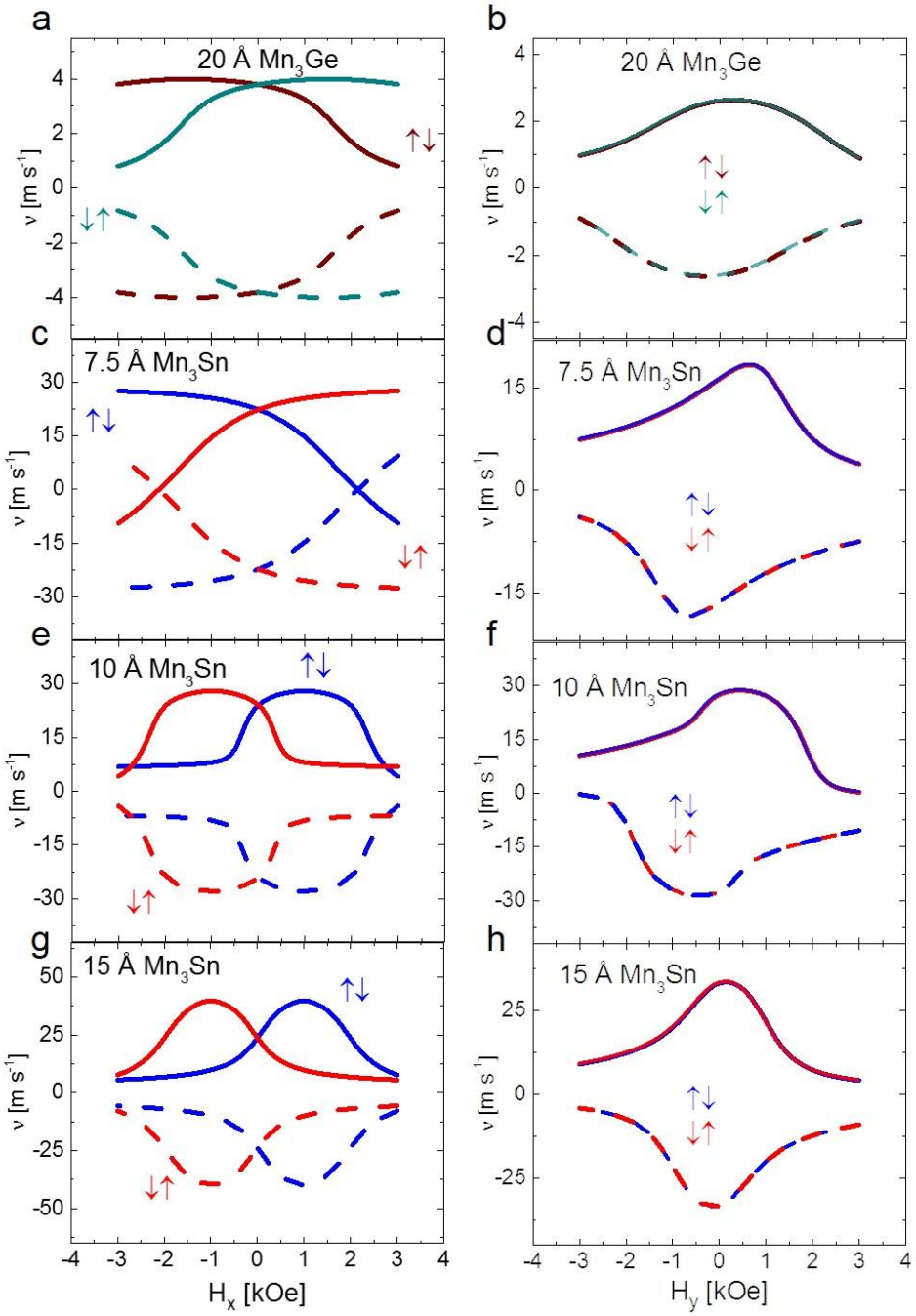

Figure 7.2 1-D model simulation for the Heusler DW motion vs H_x and H_y in-plane fields shown in Figure 4.8 -Figure 4.9. Solid or dashed lines represent positive or negative current, respectively.

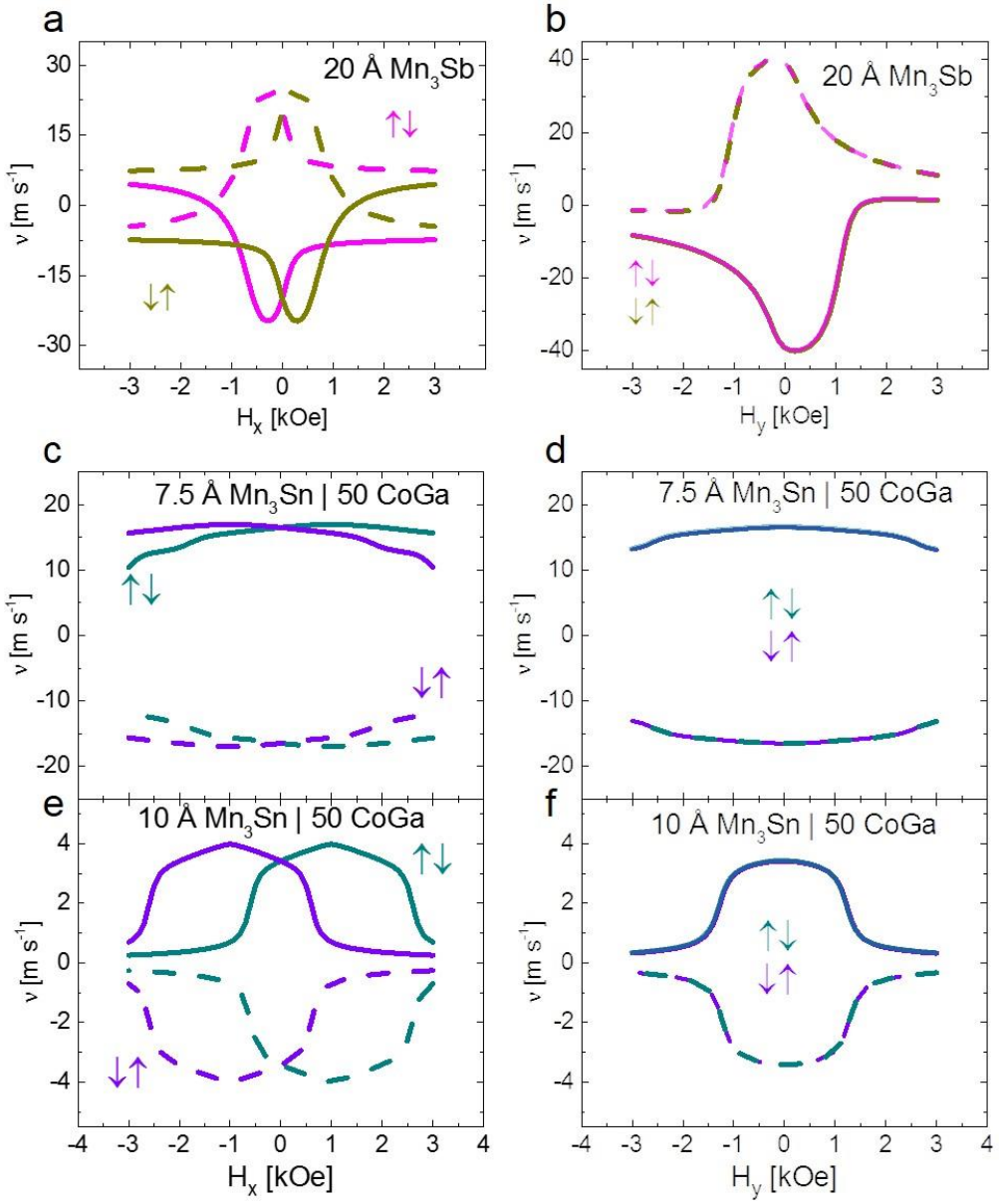

Figure 7.3 1-D model simulation for the Heusler DW motion vs H_x and H_y in-plane fields shown in Figure 4.10 -Figure 4.12. Solid or dashed lines represent positive or negative current, respectively.

The 1-D model fittings match well the experimental data, for the DW motion as seen under the influence of the H_x, H_y applied in-plane fields for all the Heuslers studied, and when the CoGa capping layer is introduced. The model considers the DW dynamics explained in chapter 2, and it describes the precessional Heusler DW motion under the action of v-STT, for a Néel type DW set by a DMI field, H_{DM}. The SHE contribution is

parametrized by the effective field H_{SH}. Thus, the 1-D model validates the DW motion mechanism described in 4.5.1 and is used to fit and extract the DW motion parameters.

The 1-D model is described in the Appendix and the DW fit parameters are presented in Table B.1 –Table B.3. Lastly, in Figure 7.4 are shown the 1-D model fits when tailoring the SOTs and DMI, seen in chapter 5, in good agreement to the experimental results.

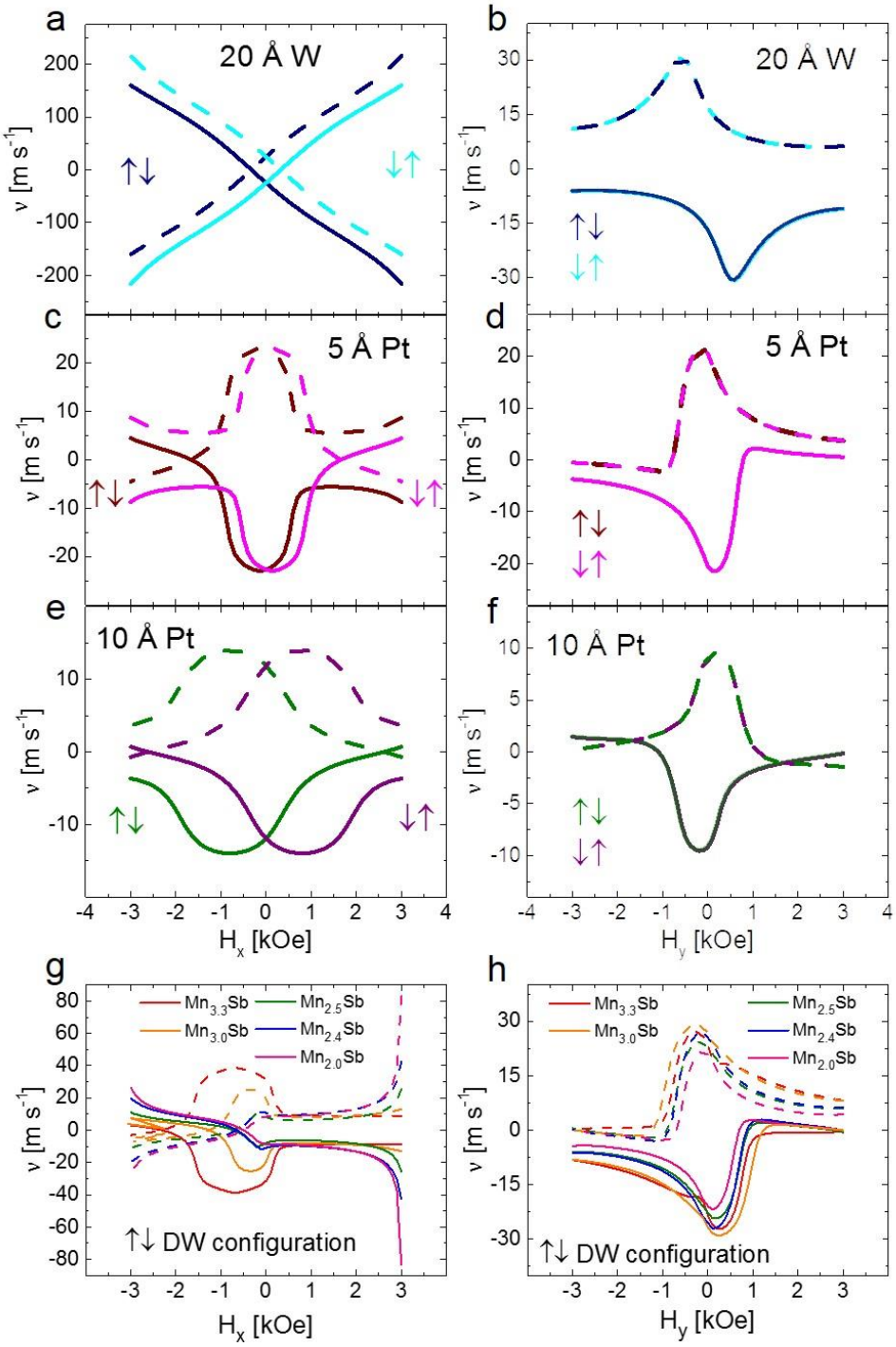

Figure 7.4 1-D model simulation for the Heusler DW motion vs H_x and H_y in-plane fields shown in Figure 5.2 -Figure 5.4. Solid or dashed lines represent positive or negative current respectively.

8. Conclusions

The ability to prepare and grow ultrathin Heusler films with high perpendicular magnetic anisotropy makes their technological application possible. Indeed, it is demonstrated that in unit cell thicknesses, Mn_3Z (Z=Ge, Sn, Sb) Heuslers can be the base of a spintronic device[111], like the Racetrack memory, as shown from their current driven domain wall motion experiments in nanowires.

To achieve these low Heusler thicknesses, while preserving their bulk-like properties, a novel concept of a chemical templating layer (CTL) is introduced and a list of candidate materials is proposed. CoAl, CoGa, CoGe and CoSn are exemplary CTL candidates as seen from their growth in TEM images and XRD. The CTLs form alternating layers which can template and provide chemical ordering for the Heusler growth through preferential chemical bonding even when an atomic step is encountered at the surface of the CTL. The CTL technique is so powerful that it works even for amorphous substrates, and is shown to promote growth for ternary Heuslers while grown at room temperature.

Studying the current induced DW motion in devices made from CTL and ultrathin Heusler provides a valuable source of information about the driving mechanism of the DW motion and corresponding phenomena arising from these structures. Mn_3Ge, Mn_3Sn and Mn_3Sb DW motion is demonstrated in the first spintronic device using ultrathin Heusler alloys. The DW driving mechanism is mainly due to the volume spin transfer torque. When examining the DW motion under externally applied in-plane fields, significant contributions from spin orbit torques are found. A bulk DMI field is discovered, which is directed along the nanowire length and sets the chirality of the DWs. SHE contributions from the CTLs are also accounting for the DW velocity results versus in-plane fields.

Lastly, the extraordinary abilities of Heusler compounds as materials for spintronic devices is demonstrated by tuning the Mn_xSb Heusler composition, which as a result

can tune the bulk DMI effective field by up to an order of magnitude. Moreover, Mn_3Ge is shown to reverse its sign of bulk spin polarization with increasing annealing temperature. Furthermore, the SHE contribution is also tuned by adding capping layers that can suppress or enhance the spin orbit torques.

1-D analytical modeling that accounts for all the torques, DMI and SHE is used to fit the experiment data and the fits are in good agreement with the data.

These results are the first demonstration of domain wall motion in ultra-thin Heusler alloys with complex and tunable magnetic properties. Additionally, showing that now these Heuslers can be grown in thin films, while retaining their bulk-like properties, sets the first step for the exploration of Heuslers for a wide range of applications and devices, from magnetic to topological[112,113]. This work is an important step to enable Heusler spintronics applications and with the remarkable class[12,114,115] of Heusler materials of more than 1500 members, I would like to envision it as extending to "Heusler-tronics".

APPENDIX A

A.1 P-MOKE for Mn_2CoSn on CoGa CTL

The CTL technique also allows for the growth of ultrathin layers of ternary layers Heusler alloys with excellent magnetic properties. An example is shown with Mn_2CoSn using a CoGa CTL.

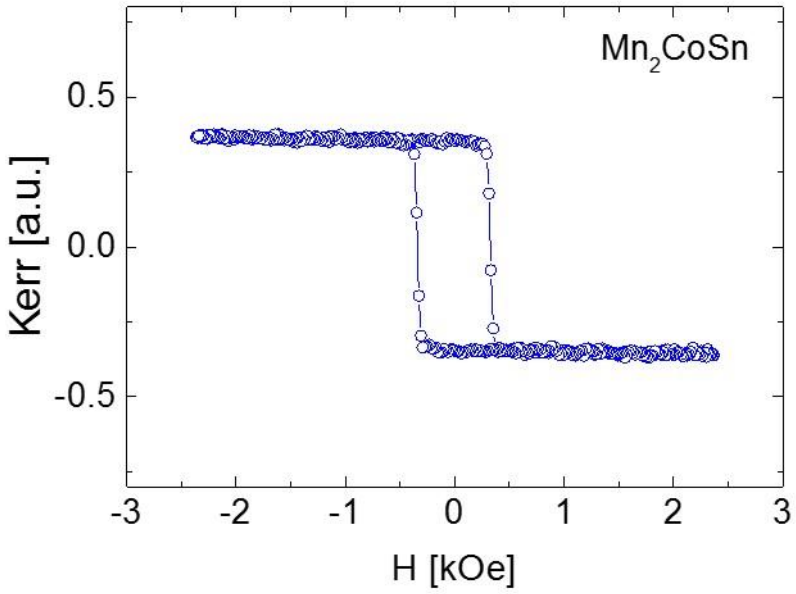

Figure A.1 P-MOKE hysteresis loop for 20 Å Mn_2CoSn. The film stack is: MgO (001) | 20 Å MgO | 300 Å CoGa | 20 Å Mn_2CoSn | 20 Å MgO | 20 Å Ta.

A.2 DW velocity vs H_x and H_y for CoSn and CoAl CTLs

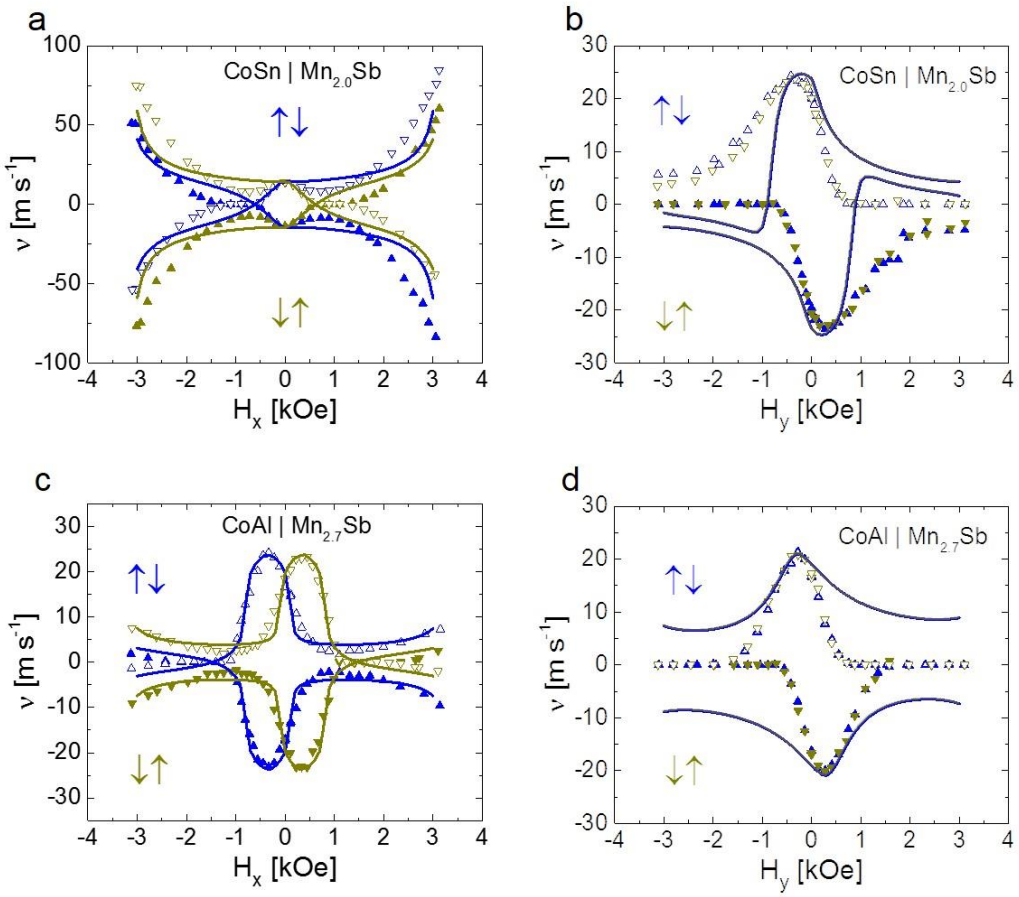

Figure A.2 ↑↓ and ↓↑ DW velocity dependence on (a) H_x and (b) H_y, in-plane fields for $Mn_{2.0}Sb$ Heusler with CoSn CTL in the stack: MgO (001) | 20 Å MgO | 30 Å CoGa | 20 Å CoSn | 20 Å $Mn_{2.0}Sb$ | 20 Å MgO | 20 Å Ta with current densities: $|J^{Hx}| = 5.2 \cdot 10^7$ A cm^{-2} and $|J^{Hy}| = 6.6 \cdot 10^7$ A cm^{-2}. ↑↓ and ↓↑ DW velocity dependence on (c) H_x and (d) H_y, in-plane fields for $Mn_{2.7}Sb$ Heusler with CoAl CTL in the stack: MgO (001) | 20 Å MgO | 50 Å CoAl | 20 Å $Mn_{2.7}Sb$ | 20 Å MgO | 20 Å Ta with current densities: $|J^{Hx}| = 5.4 \cdot 10^7$ A cm^{-2} and $|J^{Hy}| = 5.6 \cdot 10^7$ A cm^{-2}.

APPENDIX B

B.1 1-D analytical model for Heusler films

Starting from (eq.1), the Lagrangians are formulated that include the adiabatic and non-adiabatic spin transfer torques (STTs), external field driven torques, the spin Hall current torque, and the Dzyaloshinskii-Moriya exchange field. The equations of motion are then derived by the Lagrange-Rayleigh equations[57].

With the DW profile function (eq.1), the Lagrangian $\mathcal{L}$ in the nanowire that contains the magnetostatic potential energy, including anisotropy, DW kinetic energy and adiabatic spin-transfer torque is given by:

$$\mathcal{L} = \int \left(\mathcal{E} + \frac{M_s}{\gamma} \psi \dot{\theta} \sin\theta - \frac{u M_s}{\gamma} \psi \frac{d\theta}{dx} \sin\theta \right) dx$$
$$= \Delta\, M_s H_k \cos^2\psi \mp 2 M_s H_z q - \pi\, \Delta\, M_s H_p \cos(\psi - \psi_H)$$
$$- \pi\, \Delta\, M_s H_{DM} \cos\psi \mp \frac{2 w M_s}{\gamma} \phi(\dot{q} + u)$$

(eq.2)

Here the upper and lower signs correspond to the $\odot \mid \otimes$ and $\otimes \mid \odot$ magnetic DW configurations, respectively. $\mathcal{E}$ is the magnetostatic energy density of the domain wall per unit area and is given by:

$$\mathcal{E} = \frac{M_s H_k}{2} \sin^2\theta \cos^2\psi - M_s H_z \cos\theta - M_s H_p \sin\theta \cos(\psi - \psi_H)$$
$$- M_s H_{DM} \sin\theta \cos\psi$$

(eq.3)

(eq.2) can be rewritten as $\mathcal{L} = \sigma + \int \left[\frac{M_s}{\gamma} \phi \dot{\theta} \sin\theta - \frac{u M_s}{\gamma} \phi \frac{d\theta}{ds} \sin\theta \right] dx$ where σ is the magnetostatic potential energy, $\sigma = \int \mathcal{E} dx$. H_k is the magnitude of the in-plane

anisotropy field derived from the shape anisotropy of the DW that favors a Bloch wall over a Néel wall, H_z is the out-of-plane field, H_p and ψ_H are the in-plane magnetic field and its angle with respect to the $+\hat{x}$ direction, respectively. H_{DM} is the Dzyaloshinskii–Moriya interaction exchange field at the DW whose direction is always perpendicular to the DW length direction, thereby favoring Néel type walls but its sign depends on the domain configurations establishing the chirality of the domain walls. The volume spin transfer torque due to the current flowing within the magnetic layer is parameterized by $u = \frac{\mu_B P J}{e M_s}$, where μ_B is the Bohr magneton, *e* is the electron charge, *P* is the spin polarization of the current and *J* is the current density in the magnetic layer. The dissipative function $\mathcal{F}$ that includes damping, non-adiabatic spin-transfer torque, and spin-orbit torque is given by:

$$\mathcal{F} = \int \frac{\alpha M_s}{2\gamma}\left[\left(\frac{d}{dt} - \frac{\beta u}{\alpha}\frac{d}{ds}\right)\vec{m} + \frac{\gamma}{\alpha}H_{SH}\vec{m}\times\hat{y}\right]dx$$
$$= \frac{\alpha M_s}{2\gamma}\left(\frac{2\dot{q}^2}{\Delta} \pm \frac{2\pi\gamma}{\alpha}\dot{q}H_{SH}\cos\psi + \frac{4\beta u}{\alpha\Delta}\dot{q}\right)$$

(eq.4)

Here again, the upper and lower signs correspond to the ⊙ | ⊗ and ⊗ | ⊙ magnetic DW configurations, respectively, β is the non-adiabatic STT coefficient and α is the Gilbert damping. The spin Hall effect (SHE) is parameterized by an effective field H_{SH} in the center of the wire that is given by $H_{SH} = \frac{\hbar\theta_{SH}J_{UL}}{2eM_s t_H}$ where $\hbar$ is $\frac{h}{2\pi}$, h is Planck's constant, J_{UL} is the current density in the underlayer, t_H is the thickness of the magnetic layer, and θ_{SH} is the spin Hall angle (or the effective spin Hall angle that describes the magnitude of the spin accumulation that the magnetic layer is subjected to). Note that the accumulated spin from the spin Hall is transverse to the applied current direction along the wire length *x*, i.e. the spin current is along the $\hat{y}$ direction.

Based on Lagrangians $\mathcal{L}$ and dissipated function $\mathcal{F}$ obtained above, the Lagrange-Rayleigh equations $\frac{\partial\mathcal{L}}{\partial X} - \frac{d}{dt}\left(\frac{\partial\mathcal{L}}{\partial\dot{X}}\right) + \frac{\partial\mathcal{F}}{\partial\dot{X}} = 0$ ($X = q$ and ψ) finally lead to the equations of motion when $H_z = 0$ as following:

$$\alpha\dot{q} \pm \Delta\dot{\psi} = \pm\gamma\Delta H_z - \beta u \mp \frac{\pi}{2}\gamma\Delta H_{SH}\cos\psi$$

(eq.5a)

$$\dot{q} \mp \alpha\Delta\dot{\psi} = -u \pm \frac{\gamma\Delta}{2}\left[-H_k \sin 2\psi + \pi H_p \sin(\psi - \psi_H) + \pi H_{DM}\sin\psi\right]$$

(eq.5b)

Here again, the upper and lower signs correspond to the $\odot \mid \otimes$ and $\otimes \mid \odot$ domain magnetic configurations, respectively.

The (eqs.5a,b) can be rewritten as

$$(1+\alpha^2)\dot{q} = -(1+\alpha\beta)u \mp \gamma\Delta\left[\frac{H_k}{2}sin2\psi - \frac{\pi H_p}{2}\sin(\psi - \psi_H) - \frac{\pi H_{DM}}{2}\sin\psi + \frac{\alpha\pi H_{SH}}{2}\cos\psi\right]$$

(eq.6a)

$$(1+\alpha^2)\dot{\psi} = \mp\frac{\beta-\alpha}{\Delta}u + \gamma\left[\frac{\alpha H_k}{2}sin2\psi - \frac{\alpha\pi H_p}{2}\sin(\psi - \psi_H) - \frac{\alpha\pi H_{DM}}{2}\sin\psi - \frac{\pi H_{SH}}{2}\cos\psi\right]$$

(eq.6b)

(upper signs: $\odot \mid \otimes$ and lower signs: $\otimes \mid \odot$).

When the spin Hall torque is very small, i.e. $H_{SH} \approx 0$, from (eqs.6a,b) is obtained:

$$\dot{q} = -\frac{\beta}{\alpha}u \mp \frac{\Delta}{\alpha}\dot{\psi} \qquad \text{(eq.7)}$$

(eq.6b) tells us about the steady state condition, i.e. $\dot{\psi} = 0$, such that:

$$\left(\frac{\beta}{\alpha} - 1\right)u = \pm\Delta\gamma\left[\frac{H_k}{2}sin2\psi - \frac{\pi H_p}{2}\sin(\psi - \psi_H) - \frac{\pi H_{DM}}{2}\sin\psi\right]$$

(eq.8)

For example, when $H_k = 0$ and $H_{DM} = 0$, if $|u| > \left|\frac{\pi\,\Delta\gamma H_p}{2}\frac{\alpha}{\beta-\alpha}\right|$ there exists no zero of ψ to satisfy $u = \pm\frac{\pi\Delta\gamma H_p}{2}\frac{\alpha}{\beta-\alpha}\sin(\psi-\psi_H)$ so that the DW magnetization keeps on precessing. On the other hand, if $|u| \le \left|\frac{\pi\Delta\gamma H_p}{2}\frac{\alpha}{\beta-\alpha}\right|$, $\dot{\psi} = 0$, i.e., a steady state DW motion exists, thus leading to $\dot{q} = -\frac{\beta}{\alpha}u$. In the case of $\beta = 0$, $\dot{q} = \mp\frac{\Delta}{\alpha}\dot{\psi}$ so that the DW moves only when the DW magnetization precesses, that is, the steady state does not exist. In other words, if $|u| > \left|\frac{\pi\,\Delta\gamma H_p}{2}\right|$ the DW magnetization precesses and the DW continues to move, while if $|u| \le \left|\frac{\pi\,\Delta\gamma H_p}{2}\right|$, this corresponds to the steady state and consequently the DW stops moving. As a result, the DW velocity decreases with increasing $|H_p|$ by suppressing the DW magnetization precession, thereby forming a maximum velocity $v_{max} = |u|$ at $H_p = 0$. The DW velocity becomes zero at a threshold field, $H_{th} \equiv |H_p| = \left|\frac{2u}{\pi\,\Delta\gamma}\right|$ thus forming a dome-like v versus H_P curve that is symmetric with respect to $H_p = 0$. Note that H_{th} depends only on u and Δ, thus showing that H_{th} increases with increasing u and decreasing Δ, which enables us to uniquely determine the values of u and Δ by fitting v_{max} and H_{th} from v versus H_x curves.

Let us investigate which factors determine the width of the dome. To qualitatively understand this, let us make an aggressive approximation that $\sin\psi \sim \psi$ for $0 \le \psi \le 1$ when $\beta = 0$, $H_k = 0$, $H_p = H_x$ and $\psi_H = 0$. Then from (eq.6b) and (eq.6a), for $0 \le \psi \le 1$ we obtain $\psi \sim \frac{2u}{\gamma\pi H_x\Delta}\left[1-\exp\left(-\frac{\pi\alpha\gamma H_x}{2(1+\alpha^2)}t\right)\right]$ and $q \sim \frac{2u}{\gamma\pi H_x\alpha}\left[1-\exp\left(-\frac{\pi\alpha\gamma H_x}{2(1+\alpha^2)}t\right)\right]$ respectively. Hence, the time needed for the DW magnetization to reach $\psi = 1$ is $\delta t \sim -\frac{1+\alpha^2}{\alpha}\frac{2}{\pi\gamma H_x}\log\left(1-\frac{\pi\gamma H_x\Delta}{2u}\right)$ so that the average DW velocity v for $0 \le \psi \le 1$ would be $\propto \sim \frac{\alpha}{1+\alpha^2}\frac{\pi\gamma H_x}{2\log\left(1-\frac{\pi\gamma H_x\Delta}{2u}\right)}$. This shows that the dome width decreases with decreasing α and H_x and increasing Δ. As a result, the value of α can be uniquely determined as well.

When a longitudinal field $H_p = H_x$, i.e., $\psi_H = 0$, is applied in the presence of H_{DM} and a very small H_k, the dome-like curve is shifted by $-H_{DM}$ thus forming a maximum at $H_x = -H_{DM}$ since $(1+\alpha^2)\dot{\psi} = \pm\frac{\alpha}{\Delta}u - \frac{\alpha\pi\gamma(H_x+H_{DM})}{2}\sin\psi$, which is observed from the experiments (Figure 4.8 – Figure 4.10). Note that when $\beta \neq 0$, the DW velocity is finite for all H_p values that is different from what we observed from our experimental v vs H_x plot. Hence, we conclude that the non-adiabatic STT contribution in Mn_3Z is very small.

Let us intuitively understand current-induced DW motion in Heusler alloys (Figure B.2 – Figure B.3). First, we assume that $H_k = H_{SH} = 0$ and $H_p = H_x < 0$ or $H_{DM} < 0$ in $\odot$ | $\otimes$ DW configuration and $|H_x|$ or $|H_{DM}|$ are large (Figure B.1). In the absence of J, H_x (or H_{DM}) stabilizes the Néel wall structure in an anti-clockwise chirality (Figure B.1a). When an electric current J is applied along the $-\hat{x}$ direction, i.e, the conduction electrons e- with positive spin polarization ($P > 0$) flow along $\hat{x}$ direction, the volume spin-transfer torque $\vec{\tau}_{STT}$ starts to rotate the DW magnetization $\vec{M}$ along $+\hat{z}$ direction (Figure B.1b). The volume STT driven motion induces a damping torque $\vec{\tau}_d = \alpha\vec{M}\times\frac{d\vec{M}}{dt}$ that rotates $\vec{M}$ along the $-\hat{\psi}$ direction, i.e. clockwise rotation from the top view (Figure B.1c). This leads to a non-collinearity between $\vec{M}$ and $\vec{H}_x$ (or $\vec{H}_{DM}$), thus giving rise to $\vec{\tau}_x = -\gamma\vec{M}\times\vec{H}_x$ (or $\vec{\tau}_{DM} = -\gamma\vec{M}\times\vec{H}_{DM}$). Note that $\vec{\tau}_x$ (or $\vec{\tau}_{DM}$) is always along the $-\hat{z}$ direction, thereby compensating $\vec{\tau}_{STT}$ and slowing down the DW motion (Figure B.1d). $\vec{\tau}_d$ rotates $\vec{M}$ along $-\hat{\psi}$ direction until $\vec{\tau}_x$ completely cancels $\vec{\tau}_{STT}$ thus stopping the DW motion at $\psi = \arcsin\frac{2u}{\pi\Delta\gamma H_x}$ (Figure B.1e), which corresponds to $|u| \leq \left|\frac{\pi\Delta\gamma H_x}{2}\right|$, as discussed above. Here the upper bound of torque τ_x (or τ_{DM}) is $\gamma M_s H_x$ (or $\gamma M_S H_{DM}$). On the other hand, if H_x (or H_{DM}) is small, so that τ_{STT} is larger than $\gamma M_s H_x$ (or $\gamma M_S H_{DM}$), $\vec{M}$ continuously precesses and the DW keeps on moving, which corresponds to $|u| > \left|\frac{\pi\Delta\gamma H_x}{2}\right|$ (Figure B.2). Note that the DW velocity and precession angular velocity are maximum when the magnetization in the middle of the DW is directed along the $\hat{x}$-direction while they are minimum when the magnetization in the middle of the DW is directed along the $\hat{y}$-direction. Likewise, we

can readily understand the DW motion dependence on H_k (Figure B.3a-d) and $H_p = H_y$ (Figure B.3e-h).

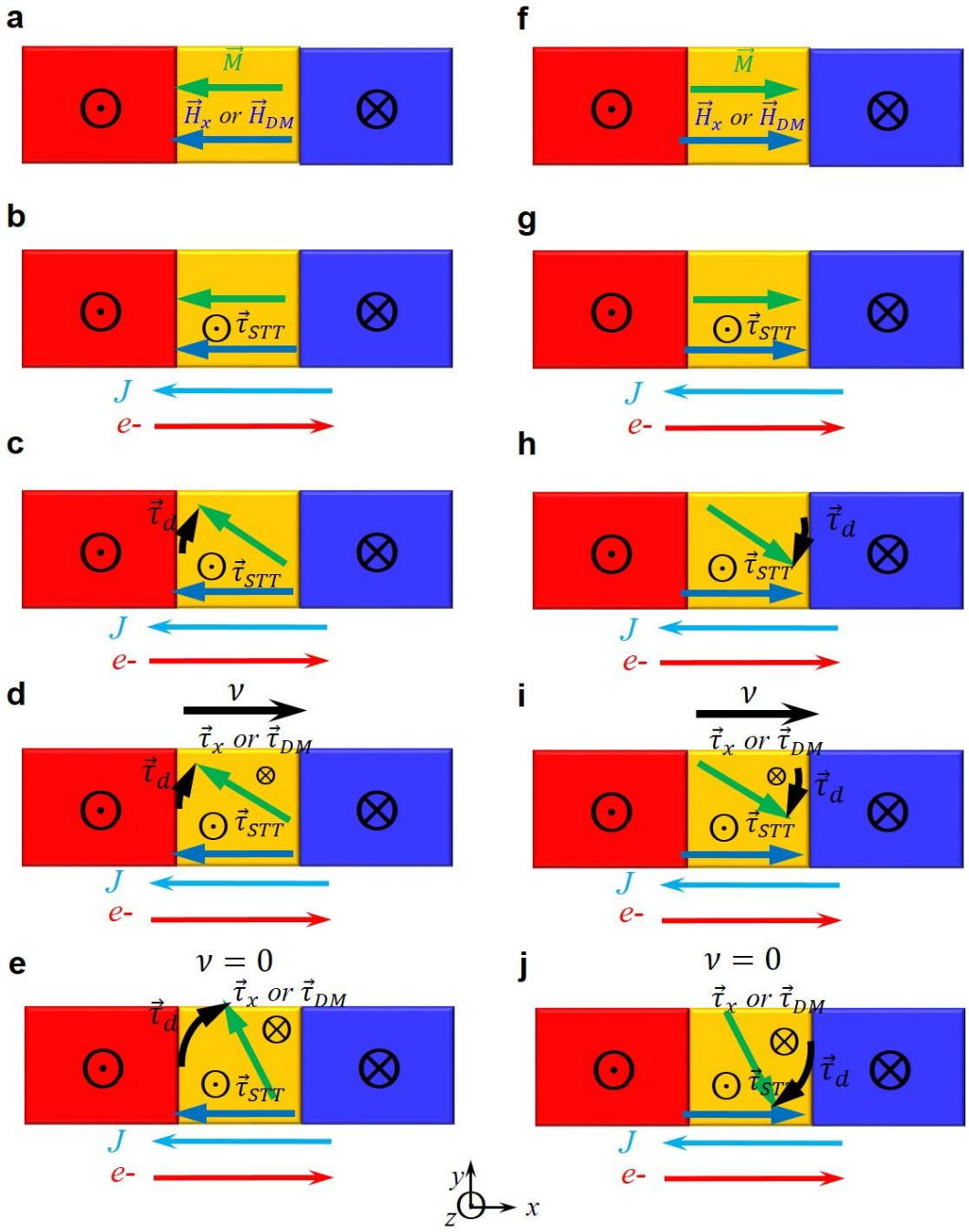

Figure B.1 Top view cartoon of current driven DW motion with ⊙ | ⊗ DW configuration in the presence of H_x or H_{DM} only. The torque $\vec{\tau}_x$ or $\vec{\tau}_{DM}$ generated by these fields are larger than $\vec{\tau}_{STT}$ here. $P > 0$ is considered. (a) Initially $J = 0$. (b)-(e), $J < 0$ for the shown field direction. In a similar way, (f) $J = 0$. (g)-(j), $J < 0$ for the opposite field direction as shown.

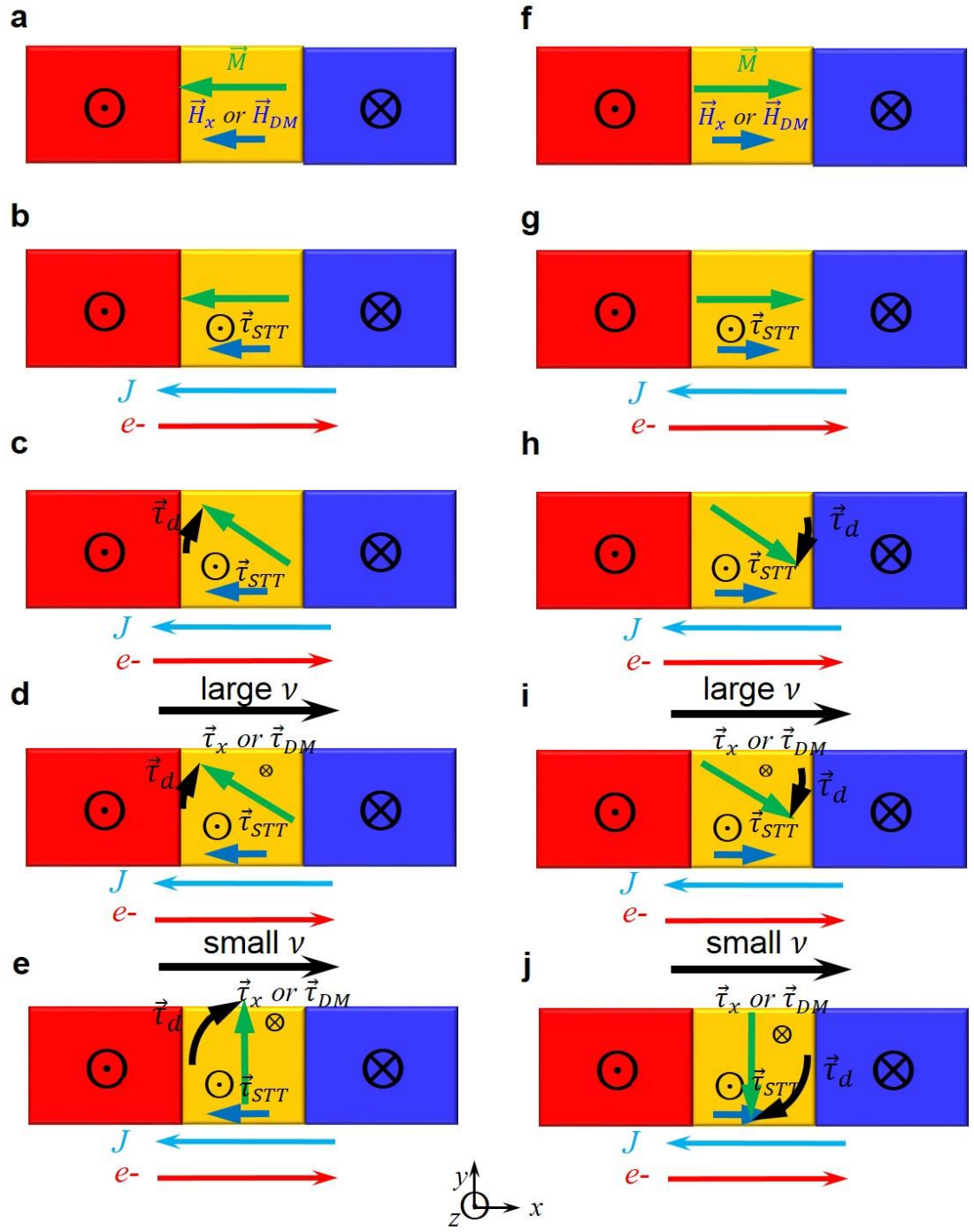

Figure B.2 Top view cartoon of current driven DW motion with ⊙ | ⊗ DW configuration in the presence of H_x or H_{DM} only. The torque $\vec{\tau}_x$ or $\vec{\tau}_{DM}$ generated by these fields are smaller than $\vec{\tau}_{STT}$ here. $P > 0$ is considered. (a) Initially $J = 0$. (b)-(e), $J < 0$ for the shown field direction. In a similar way, (f) $J = 0$. (g)-(j), $J < 0$ for the opposite field direction as shown.

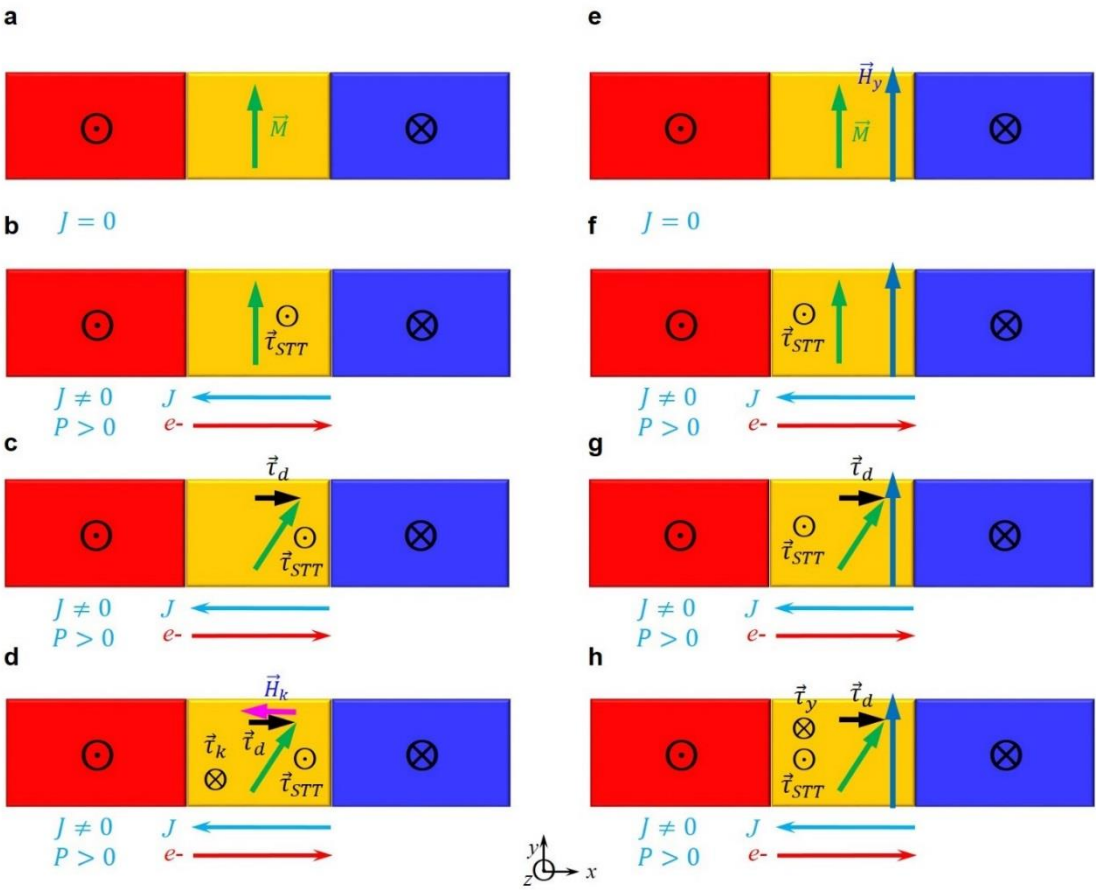

Figure B.3 Top view cartoon of current driven DW motion with ⊙|⊗ DW configuration in the presence of H_k only. (a), Initially J=0. (b)-(d), J<0. Top view cartoon of current driven DW motion with ⊙|⊗ DW configuration in the presence of H_y only. (e), Initially J=0. (f)-(h), J<0.

B.2 1-D model estimated parameter values

	50 Å CoGa 20 Å Mn_3Ge	50 Å CoGa 7.5 Å Mn_3Sn	50 Å CoGa 10 Å Mn_3Sn	50 Å CoGa 15 Å Mn_3Sn	50 Å CoGa 20 Å Mn_3Sb
α	0.01	0.048	0.025	0.02	0.05
β	0	0	0	0	0
Δ (Å)	0.3	5	5	8	12
$H_{\mathrm{k}}(Oe)$	100	100	100	100	100
$H_{\mathrm{SH}}(Oe)$	5	100	13	5	10
θ_{SH}	0.0012	0.0114	0.0012	0.0006	0.0049
$u\ (ms^{-1})$	4	15	30	45	-27
$H_{\mathrm{DM}}(Oe)$	1500 (CW)	-1000 (CCW)	-1000 (CCW)	-1000 (CCW)	300 (CW)

Table B.1 List of fitting parameters for the fits in Figure 7.2 -Figure 7.3.

	50 Å CoSn 20 Å $Mn_{2.0}Sb$	50 Å CoAl 20 Å $Mn_{2.7}Sb$	7.5 Å Mn_3Sn (capped with CoGa)	10 Å Mn_3Sn (capped with CoGa)	20 Å Mn_3Sb (capped with 5 Å Pt)	20 Å Mn_3Sb (capped with 10 Å Pt)
α	0.05	0.09	0.048	0.03	0.03	0.02
β	0	0	0	0	0	0
Δ (Å)	12	14	1.15	0.7	8	2.5
$H_{\mathrm{k}}(Oe)$	100	100	100	100	100	100
$H_{\mathrm{SH}}(Oe)$	20	5	0	0	7	-3
θ_{SH}	0.0055	0.0013	0.0000	0.0000	0.0013	-0.0006
$u\ (ms^{-1})$	-15	-24	17	4	-23	-14
$H_{\mathrm{DM}}(Oe)$	50 (CW)	350 (CW)	-1000 (CCW)	-1000 (CCW)	150 (CW)	800 (CW)

Table B.2 List of fitting parameters for the fits in Figure 7.3 -Figure 7.4 and Figure A.

	20 Å Mn_3Sb (capped with 20 Å W)	20 Å $Mn_{3.3}Sb$	20 Å $Mn_{3.0}Sb$	20 Å $Mn_{2.5}Sb$	20 Å $Mn_{2.4}Sb$	20 Å $Mn_{2.0}Sb$
α	0.12	0.05	0.05	0.07	0.05	0.05
β	0	0	0	0	0	0
Δ (Å)	30	12	14	12	14	14
$H_{\mathrm{k}}(Oe)$	100	100	100	100	100	100
$H_{\mathrm{SH}}(Oe)$	200	10	10	10	10	10
θ_{SH}	0.0838	0.0024	0.0048	0.0046	0.0047	0.0050
$u\ (ms^{-1})$	-10	-39	-25.5	-11	-12	-9
$H_{\mathrm{DM}}(Oe)$	450 (CW)	700 (CW)	350 (CW)	200 (CW)	150 (CW)	50 (CW)

Table B.3 List of fitting parameters for the fits in Figure 7.4.

Bibliography

1. Grünberg, P. *et al.* Layered magnetic structures: Evidence for antiferromagnetic coupling of Fe layers across Cr interlayers. *J. Appl. Phys.* **61,** 3750–3752 (1987).
2. Baibich, M. N. *et al.* Giant Magnetoresistance of (001)Fe/(001)Cr Magnetic Superlattices. *Phys. Rev. Lett.* **61,** 2472–2475 (1988).
3. Reig, C., Cardoso, S. & Mukhopadhyay, S. C. *Giant Magnetoresistance (GMR) Sensors: From Basis to State-of-the-Art Applications*. (Springer-Verlag, 2013).
4. Parkin, S. S. P. Giant Magnetoresistance in Magnetic Nanostructures. *Annu. Rev. Mater. Sci.* **25,** 357–388 (1995).
5. Bhatti, S. *et al.* Spintronics based random access memory: a review. *Mater. Today* **20,** 530–548 (2017).
6. Parkin, S. S. P., Hayashi, M. & Thomas, L. Magnetic Domain-Wall Racetrack Memory. *Science* **320,** 190–194 (2008).
7. Ikeda, S. *et al.* A perpendicular-anisotropy CoFeB–MgO magnetic tunnel junction. *Nat. Mater.* **9,** 721–724 (2010).
8. Sato, H. *et al.* Properties of magnetic tunnel junctions with a MgO/CoFeB/Ta/CoFeB/MgO recording structure down to junction diameter of 11 nm. *Appl. Phys. Lett.* **105,** 062403 (2014).
9. Parkin, S. S. P. *et al.* Giant tunnelling magnetoresistance at room temperature with MgO (100) tunnel barriers. *Nat. Mater.* **3,** 862–867 (2004).
10. Faleev, S. V. *et al.* Origin of the Tetragonal Ground State of Heusler Compounds. *Phys. Rev. Appl.* **7,** 034022 (2017).

11. Faleev, S. V. *et al.* Heusler compounds with perpendicular magnetic anisotropy and large tunneling magnetoresistance. *Phys. Rev. Mater.* **1,** 024402 (2017).
12. Graf, T., Felser, C. & Parkin, S. S. P. Simple rules for the understanding of Heusler compounds. *Prog. Solid State Chem.* **39,** 1–50 (2011).
13. Winterlik, J. *et al.* Design Scheme of New Tetragonal Heusler Compounds for Spin-Transfer Torque Applications and its Experimental Realization. *Adv. Mater.* **24,** 6283–6287 (2012).
14. Faleev, S. V. *et al.* Unified explanation of chemical ordering, the Slater-Pauling rule, and half-metallicity in full Heusler compounds. *Phys. Rev. B* **95,** 045140 (2017).
15. Oogane, M. & Mizukami, S. Tunnel magnetoresistance effect and magnetic damping in half-metallic Heusler alloys. *Philos. Trans. Math. Phys. Eng. Sci.* **369,** 3037–3053 (2011).
16. Hillebrands, B. & Felser, C. High-spin polarization of Heusler alloys. *J. Phys. Appl. Phys.* **39,** (2006).
17. Trudel, S., Gaier, O., Hamrle, J. & Hillebrands, B. Magnetic anisotropy, exchange and damping in cobalt-based full-Heusler compounds: an experimental review. *J. Phys. Appl. Phys.* **43,** 193001 (2010).
18. Gupta, D. C. & Bhat, I. H. Investigation of high spin-polarization, magnetic, electronic and half-metallic properties in RuMn2Ge and RuMn2Sb Heusler alloys. *Mater. Sci. Eng. B* **193,** 70–75 (2015).
19. Kurt, H. *et al.* Exchange-biased magnetic tunnel junctions with antiferromagnetic ε-Mn3Ga. *Appl. Phys. Lett.* **101,** 232402 (2012).

20. Sugihara, A., Mizukami, S., Yamada, Y., Koike, K. & Miyazaki, T. High perpendicular magnetic anisotropy in D022-Mn3+xGe tetragonal Heusler alloy films. *Appl. Phys. Lett.* **104,** 132404 (2014).
21. Jeong, J. *et al.* Termination layer compensated tunnelling magnetoresistance in ferrimagnetic Heusler compounds with high perpendicular magnetic anisotropy. *Nat. Commun.* **7,** 10276 (2016).
22. Kubota, T. *et al.* Tunnel magnetoresistance effect using perpendicularly magnetized tetragonal and cubic Mn-Co-Ga Heusler alloy electrode. *J. Appl. Phys.* **115,** 17C704 (2014).
23. Wu, F. *et al.* Epitaxial Mn2.5Ga thin films with giant perpendicular magnetic anisotropy for spintronic devices. *Appl. Phys. Lett.* **94,** 122503 (2009).
24. Li, M., Jiang, X., Samant, M. G., Felser, C. & Parkin, S. S. P. Strong dependence of the tetragonal Mn2.1Ga thin film crystallization temperature window on seed layer. *Appl. Phys. Lett.* **103,** 032410 (2013).
25. Köhler, A., Knez, I., Ebke, D., Felser, C. & Parkin, S. S. P. Loss of anisotropy in strained ultrathin epitaxial L10 Mn-Ga films. *Appl. Phys. Lett.* **103,** 162406 (2013).
26. Kurt, H., Rode, K., Venkatesan, M., Stamenov, P. & Coey, J. M. D. High spin polarization in epitaxial films of ferrimagnetic Mn3Ga. *Phys. Rev. B* **83,** 020405 (2011).
27. Wu, F. *et al.* Structural and Magnetic Properties of Perpendicular Magnetized Mn2.5Ga Epitaxial Films. *IEEE Trans. Magn.* **46,** 1863–1865 (2010).
28. Suzuki, K. Z., Ranjbar, R., Sugihara, A., Miyazaki, T. & Mizukami, S. Room temperature growth of ultrathin ordered MnGa films on a CoGa buffer layer. *Jpn. J. Appl. Phys.* **55,** 010305 (2015).

29. Suzuki, K. Z., Ono, A., Ranjbar, R., Sugihara, A. & Mizukami, S. Effect of Buffer Layer Annealing on the Growth of (001)-Textured MnGa Ultrathin Films With Perpendicular Magnetic Anisotropy. *IEEE Trans. Magn.* **53,** 1–4 (2017).
30. Suzuki, K. Z. *et al.* Perpendicular magnetic tunnel junctions with Mn-modified ultrathin MnGa layer. *Appl. Phys. Lett.* **112,** 062402 (2018).
31. Ryu, K.-S., Thomas, L., Yang, S.-H. & Parkin, S. Chiral spin torque at magnetic domain walls. *Nat. Nanotechnol.* **8,** 527–533 (2013).
32. Parkin, S. & Yang, S.-H. Memory on the racetrack. *Nat. Nanotechnol.* **10,** 195–198 (2015).
33. Shizgal, B. D. & Weaver, D. P. *Rarefied Gas Dynamics: Technical Papers from the Proceedings of the Eighteenth International Symposium on Rarefied Gas Dynamics, University of British Columbia, Vancouver, British Columbia, Canada, July 26-30, 1992* (American Institute of Aeronautics and Astronautics, Incorporated, 1994).
34. Koebley, S. R., Outlaw, R. A. & Dellwo, R. R. Degassing a vacuum system with in-situ UV radiation. *J. Vac. Sci. Technol. A* **30,** 060601 (2012).
35. Kelly, P. J. & Arnell, R. D. Magnetron sputtering: a review of recent developments and applications. *Vacuum* **56,** 159–172 (2000).
36. Hitchman, M. L. Featuring thin films. Handbook of Thin Film Process Technology. Edited by D. A. Glocker and S. I. Shah, Institute of Physics, Bristol 1995, XII, 798. *Chem. Vap. Depos.* **3,** 144–145 (1997).
37. Frey, H. & Khan, H. R. *Handbook of Thin Film Technology*. (Springer-Verlag, 2015).
38. Ohring, M. *The Materials Science of Thin Films: Deposition and Structure*. (2006).

39. Abdelrahman, M. M. Study of ion beam sputtering using a glow discharge ion source. *Braz. J. Phys.* **40,** 26–29 (2010).

40. Döbeli, M. Subtraction tool for the analysis of RBS data. *Nucl. Instrum. Methods Phys. Res. Sect. B Beam Interact. Mater. At.* **249,** 800–803 (2006).

41. Tsuboi, Y., Albrektsson, T., Sennerby, L., Johansson, C. & Ektessabi, A. M. Characterization of thin films for biomaterial applications using PIXE and RBS. *Nucl. Instrum. Methods Phys. Res. Sect. Accel. Spectrometers Detect. Assoc. Equip.* **353,** 597–600 (1994).

42. Johansson, S. a. E. & Campbell, J. L. PIXE: a novel technique for elemental analysis. (1988).

43. Tabacniks, M. H., Kellock, A. J. & Baglin, J. E. E. PIXE for thin film analysis. *AIP Conf. Proc.* **392,** 563–566 (1997).

44. Fowler, C. A. & Fryer, E. M. Magnetic Domains by the Longitudinal Kerr Effect. *Phys. Rev.* **94,** 52–56 (1954).

45. Hubert, A. & Schäfer, R. *Magnetic Domains: The Analysis of Magnetic Microstructures*. (Springer-Verlag, 1998).

46. Haider, T. A Review of Magneto-Optic Effects and Its Application. *Int. J. Electromagn. Appl.* **7,** 17–24 (2017).

47. Soldatov, I. V. & Schäfer, R. Advances in quantitative Kerr microscopy. *Phys. Rev. B* **95,** 014426 (2017).

48. Jalili, N. & Laxminarayana, K. A review of atomic force microscopy imaging systems: application to molecular metrology and biological sciences. *Mechatronics* **14,** 907–945 (2004).

49. Johnson, M. T., Bloemen, P. J. H., Broeder, F. J. A. den & Vries, J. J. de. Magnetic anisotropy in metallic multilayers. *Rep. Prog. Phys.* **59,** 1409–1458 (1996).

50. Bobeck, A. H., Bonyhard, P., Geusic, J. E. & others. Magnetic bubbles—An emerging new memory technology. *Proc. IEEE* **63,** 1176–1195 (1975).

51. Malozemoff, A. P. & Slonczewski, J. C. *Magnetic Domain Walls in Bubble Materials*. (Elsevier, 1979).

52. De Leeuw, F. H., Van Den Doel, R. & Enz, U. Dynamic properties of magnetic domain walls and magnetic bubbles. *Rep. Prog. Phys.* **43,** 689 (1980).

53. Middelhoek, S. Domain Walls in Thin Ni–Fe Films. *J. Appl. Phys.* **34,** 1054–1059 (1963).

54. Koyama, T. *et al.* Observation of the intrinsic pinning of a magnetic domain wall in a ferromagnetic nanowire. *Nat. Mater.* **10,** 194–197 (2011).

55. DeJong, M. D. & Livesey, K. L. Analytic theory for the switch from Bloch to Néel domain wall in nanowires with perpendicular anisotropy. *Phys. Rev. B* **92,** 214420 (2015).

56. Jung, S.-W., Kim, W., Lee, T.-D., Lee, K.-J. & Lee, H.-W. Current-induced domain wall motion in a nanowire with perpendicular magnetic anisotropy. *Appl. Phys. Lett.* **92,** 202508 (2008).

57. Hubert, A. *Theorie der Domänenwände in geordneten Medien* (Springer).

58. Gilbert, T. L. A phenomenological theory of damping in ferromagnetic materials. *IEEE Trans. Magn.* **40,** 3443–3449 (2004).

59. Mazin, I. I. How to Define and Calculate the Degree of Spin Polarization in Ferromagnets. *Phys. Rev. Lett.* **83,** 1427–1430 (1999).

60. Berger, L. Low-field magnetoresistance and domain drag in ferromagnets. *J. Appl. Phys.* **49,** 2156–2161 (1978).

61. Berger, L. Exchange interaction between ferromagnetic domain wall and electric current in very thin metallic films. *J. Appl. Phys.* **55,** 1954–1956 (1984).

62. Berger, L. Emission of spin waves by a magnetic multilayer traversed by a current. *Phys. Rev. B* **54,** 9353–9358 (1996).

63. Slonczewski, J. C. Current-driven excitation of magnetic multilayers. *J. Magn. Magn. Mater.* **159,** L1–L7 (1996).

64. Thiaville, A., García, J. M. & Miltat, J. Domain wall dynamics in nanowires. *J. Magn. Magn. Mater.* **242–245, Part 2,** 1061–1063 (2002).

65. Zhang, S. & Li, Z. Roles of Nonequilibrium Conduction Electrons on the Magnetization Dynamics of Ferromagnets. *Phys. Rev. Lett.* **93,** 127204 (2004).

66. Thiaville, A., Nakatani, Y., Miltat, J. & Suzuki, Y. Micromagnetic understanding of current-driven domain wall motion in patterned nanowires. *Europhys. Lett. EPL* **69,** 990–996 (2005).

67. Dyakonov, M. I. Spin Hall Effect. *ArXiv12103200 Cond-Mat Physicsphysics Physicsquant-Ph* (2012).

68. Hirsch, J. E. Spin Hall Effect. *Phys. Rev. Lett.* **83,** 1834–1837 (1999).

69. Murakami, S., Nagaosa, N. & Zhang, S.-C. Dissipationless Quantum Spin Current at Room Temperature. *Science* **301,** 1348–1351 (2003).

70. Sinova, J. *et al.* Universal Intrinsic Spin Hall Effect. *Phys. Rev. Lett.* **92,** (2004).

71. Liu, L., Moriyama, T., Ralph, D. C. & Buhrman, R. A. Spin-Torque Ferromagnetic Resonance Induced by the Spin Hall Effect. *Phys. Rev. Lett.* **106,** 036601 (2011).

72. Zhang, W., Han, W., Jiang, X., Yang, S.-H. & Parkin, S. S. P. Role of transparency of platinum–ferromagnet interfaces in determining the intrinsic magnitude of the spin Hall effect. *Nat. Phys.* **11,** 496–502 (2015).

73. Nguyen, M.-H., Ralph, D. C. & Buhrman, R. A. Spin Torque Study of the Spin Hall Conductivity and Spin Diffusion Length in Platinum Thin Films with Varying Resistivity. *Phys. Rev. Lett.* **116,** 126601 (2016).

74. Liu, L. *et al.* Spin-Torque Switching with the Giant Spin Hall Effect of Tantalum. *Science* **336,** 555–558 (2012).

75. Demasius, K.-U. *et al.* Enhanced spin-orbit torques by oxygen incorporation in tungsten films. *Nat. Commun.* **7,** 10644 (2016).

76. Dresselhaus, G. Spin-Orbit Coupling Effects in Zinc Blende Structures. *Phys. Rev.* **100,** 580–586 (1955).

77. Rashba, E. Properties of semiconductors with an extremum loop. 1. Cyclotron and combinational resonance in a magnetic field perpendicular to the plane of the loop. *Sov Phys Solid State* **2,** 1224–1238 (1960).

78. Manchon, A., Koo, H. C., Nitta, J., Frolov, S. M. & Duine, R. A. New perspectives for Rashba spin–orbit coupling. *Nat. Mater.* **14,** 871–882 (2015).

79. Emori, S., Bauer, U., Ahn, S.-M., Martinez, E. & Beach, G. S. D. Current-driven dynamics of chiral ferromagnetic domain walls. *Nat. Mater.* **12,** 611–616 (2013).

80. Dzyaloshinsky, I. A thermodynamic theory of "weak" ferromagnetism of antiferromagnetics. *J. Phys. Chem. Solids* **4,** 241–255 (1958).

81. Moriya, T. Anisotropic Superexchange Interaction and Weak Ferromagnetism. *Phys. Rev.* **120,** 91–98 (1960).

82. Bode, M. *et al.* Chiral magnetic order at surfaces driven by inversion asymmetry. *Nature* **447,** 190–193 (2007).

83. Valizadeh, M. M. & Satpathy, S. Dzyaloshinskii-Moriya interaction in the presence of Rashba and Dresselhaus spin-orbit coupling. *Phys. Rev. B* **97,** 094419 (2018).

84. van Vleck, J. H. On the Anisotropy of Cubic Ferromagnetic Crystals. *Phys. Rev.* **52,** 1178–1198 (1937).

85. Kittel, C. *Introduction to solid state physics*. (Wiley, 2005).

86. Alejos, O. *et al.* Current-driven domain wall dynamics in ferromagnetic layers synthetically exchange-coupled by a spacer: A micromagnetic study. *J. Appl. Phys.* **123,** 013901 (2018).

87. Avci, C. O. *et al.* Current-induced switching in a magnetic insulator. *Nat. Mater.* **16,** 309–314 (2017).

88. Brataas, A., Kent, A. D. & Ohno, H. Current-induced torques in magnetic materials. *Nat. Mater.* **11,** 372–381 (2012).

89. Liu, L., Lee, O. J., Gudmundsen, T. J., Ralph, D. C. & Buhrman, R. A. Current-Induced Switching of Perpendicularly Magnetized Magnetic Layers Using Spin Torque from the Spin Hall Effect. *Phys. Rev. Lett.* **109,** 096602 (2012).

90. Lee, O. J. *et al.* Central role of domain wall depinning for perpendicular magnetization switching driven by spin torque from the spin Hall effect. *Phys. Rev. B* **89,** 024418 (2014).

91. Bhowmik, D. *et al.* Deterministic Domain Wall Motion Orthogonal To Current Flow Due To Spin Orbit Torque. *ArXiv Prepr. ArXiv14076137* (2014).

92. Burrowes, C. *et al.* Non-adiabatic spin-torques in narrow magnetic domain walls. *Nat. Phys.* **6,** 17–21 (2010).

93. Ryu, K.-S., Thomas, L., Yang, S.-H. & Parkin, S. S. P. Current Induced Tilting of Domain Walls in High Velocity Motion along Perpendicularly Magnetized Micron-Sized Co/Ni/Co Racetracks. *Appl. Phys. Express* **5,** 093006 (2012).

94. Thomas, L. *et al.* Oscillatory dependence of current-driven magnetic domain wall motion on current pulse length. *Nature* **443,** 197–200 (2006).

95. Paixão, E. L. M. *et al.* Depinning of the transverse domain wall trapped at magnetic impurities patterned in planar nanowires: Control of the wall motion using low-intensity and short-duration current pulses. *J. Magn. Magn. Mater.* **451,** 639–646 (2018).

96. Moretti, S., Voto, M. & Martinez, E. Dynamical depinning of chiral domain walls. *Phys. Rev. B* **96,** 054433 (2017).

97. Ryu, K.-S., Yang, S.-H., Thomas, L. & Parkin, S. S. P. Chiral spin torque arising from proximity-induced magnetization. *Nat. Commun.* **5,** 3910 (2014).

98. Yang, S.-H., Ryu, K.-S. & Parkin, S. Domain-wall velocities of up to 750 m s−1 driven by exchange-coupling torque in synthetic antiferromagnets. *Nat. Nanotechnol.* **10,** 221–226 (2015).

99. Dzyaloshinskii, I. E. Theory of helicoidal structures in antiferromagnets. 1. Nonmetals. *Sov Phys JETP* **19,** 960–971 (1964).

100. Moriya, T. & Miyadai, T. Evidence for the helical spin structure due to antisymmetric exchange interaction in Cr13NbS2. *Solid State Commun.* **42,** 209–212 (1982).

101. Hrabec, A. *et al.* DMI meter: Measuring the Dzyaloshinskii-Moriya interaction inversion in Pt/Co/Ir/Pt multilayers. *ArXiv Prepr. ArXiv14025410* (2014).

102. Ryu, K. S., Yang, S. h, Thomas, L. & Parkin, S. S. P. Current induced domain wall motion for electron flow in ferromagnetic Pt/Co/Ni/Co/Pt wires. *IEEE Trans. Magn.* 1–1 (2016).

103. Ryu, J., Lee, K.-J. & Lee, H.-W. Current-driven domain wall motion with spin Hall effect: Reduction of threshold current density. *Appl. Phys. Lett.* **102,** 172404 (2013).

104. Dmitrienko, V. E. *et al.* Measuring the Dzyaloshinskii-Moriya interaction in a weak ferromagnet. *Nat. Phys.* **10,** 202–206 (2014).

105. Chaurasiya, A. K. *et al.* Direct Observation of Interfacial Dzyaloshinskii-Moriya Interaction from Asymmetric Spin-wave Propagation in W/CoFeB/SiO2 Heterostructures Down to Sub-nanometer CoFeB Thickness. *Sci. Rep.* **6,** 32592 (2016).

106. Dmitriev, V., Chernyshov, D., Grigoriev, S. & Dyadkin, V. A chiral link between structure and magnetism in MnSi. *J. Phys. Condens. Matter* **24,** 366005 (2012).

107. Turgut, E. *et al.* Engineering Dzyaloshinskii-Moriya interaction in B20 thin-film chiral magnets. *Phys. Rev. Mater.* **2,** (2018).

108. Yang, T., Kohda, M., Seki, T., Takanashi, K. & Nitta, J. Platinum layer thickness dependence of spin-Hall induced effective magnetic field in Pt/Co/Pt structures. *Jpn. J. Appl. Phys.* **53,** 04EM06 (2014).

109. Malozemoff, A. P. & Slonczewski, J. C. *Magnetic Domain Walls in Bubble Materials*. (Elsevier, 1979).

110. Garg, C., Yang, S.-H., Phung, T., Pushp, A. & Parkin, S. S. P. Dramatic influence of curvature of nanowire on chiral domain wall velocity. *Sci. Adv.* **3,** e1602804 (2017).

111. Felser, C. & Fecher, G. H. *Spintronics From Materials to Devices*. (Springer Netherlands, 2013).

112. Chadov, S. *et al.* Tunable multifunctional topological insulators in ternary Heusler compounds. *Nat. Mater.* **9,** 541–545 (2010).

113. Lin, H. *et al.* Half-Heusler ternary compounds as new multifunctional experimental platforms for topological quantum phenomena. *Nat. Mater.* **9,** 546–549 (2010).

114. Felser, C., Wollmann, L., Chadov, S., Fecher, G. H. & Parkin, S. S. P. Basics and prospective of magnetic Heusler compounds. *APL Mater.* **3,** 041518 (2015).

115. Galanakis, I. Theory of Heusler and Full-Heusler Compounds. in *Heusler Alloys* (eds. Felser, C. & Hirohata, A.) **222,** 3–36 (Springer International Publishing, 2016).

Publications

[1] Filippou, P. Ch. *et al.* Chiral domain wall motion in unit-cell thick perpendicularly magnetized Heusler films prepared by chemical templating. *Nature Communications* 9, 4653 (2018)

[2] Critical spin polarization sign change in Mn_3Ge Heusler films. Filippou *et al*. (work in progress)

[3] Coupling adjacent ultrathin Heusler alloys through advanced Chemical Templating Layer materials. Filippou *et al*. (work in progress)

Acknowledgments

To complete my study on this and several other projects, I would like to thank all the people here in IBM Almaden that helped and supported my work while conducting my research. Specifically, of tremendous support were Mahesh, Jaewoo, Yari, See-Hun, Chirag and of course my supervisor, Stuart who is always asking out of the box questions which always inspire for further research.

Of great help, always assisting, are also Kevin, Chris, Manny, who helped in setting the experimental setup, Brian, helping in fabrication, Andy, for the valuable RBS results and Teya, Eric, Eugene for providing excellent TEM images.

Additionally, the support from Max Planck Institute in Halle and the Martin Luther University are very well appreciated. As well as specific people who always helped in this collaboration, Simone and Antje.

Finally, I want to acknowledge the support from all my friends which have not been mentioned already, Donata, Reinier, April, Beili, Francesco, Maria, Tom, Andrea, Eveline, Mareva and the support from my family.

Curriculum Vitae

First Name:	Panagiotis Charilaos
Family Name:	Filippou
Gender:	Male
Date of Birth:	25th February 1986
Place of Birth:	Amarousio, Greece
Address:	5687 Keymar Dr., San Jose, 95123 CA, USA
Nationality:	Greek

ACADEMIC EDUCATION

10/2014-3/2019	Doctor of Philosophy in Physics Martin-Luther-University Halle-Wittenberg, Halle, Germany
10/2011-09/2013	Master's Degree in Nanotechnology Polytechnic of Turin, Italy Institute National Polytechnic of Grenoble, France Ecole Polytechnique Fédérale de Lausanne, Switzerland
10/2003-10/2010	Bachelor's Degree in Applied Physics National Technical University of Athens, Greece

Panagiotis Charilaos Filippou

San Jose, California, USA

27th April 2019

Eidesstattliche Erklärung

Hiermit erkläre ich, PANAGIOTIS CHARILAOS FILIPPOU, dass ich die vorliegende Arbeit mit dem Titel: **Unit cell thick ferrimagnetic Heusler Domain Wall motion using Chemical Templating Layers** in allen Teilen selbständig verfasst und keine anderen als die angegebenen Quellen und Hilfsmittel benutzt habe. Alle wörtlich oder sinngemäß übernommenen Textstellen habe ich als solche kenntlich gemacht.

Ferner liegen gegen mich weder gerichtliche Vorstrafen vor, noch sind staatsanwaltliche Ermittlungen oder Disziplinarverfahren eingeleitet worden.

Des Weiteren erkläre ich hiermit, dass ich bisher keine andere Arbeit zur Promotion eingereicht noch mit einer anderen Arbeit den Versuch zur Promotion unternommen habe.

San Jose, California, USA

den 11. Oktober 2018

PANAGIOTIS CHARILAOS FILIPPOU